Internal Report
DESY F35D-96-16
November 1996

Inclusive Properties of Diffractive and Non-Diffractive Photoproduction at HERA

by

M. Kasprzak

Inclusive properties of diffractive and non–diffractive photoproduction at HERA

Michał Kasprzak

Institute of Experimental Physics
Department of Physics at the Warsaw University

April 1996

A PhD thesis carried out under the supervision of Prof. Aharon Levy.

Abstract

Inclusive properties of photoproduction at the centre of mass (c.m.) energy of $W \approx 200$ GeV were studied at HERA using the ZEUS detector. The transverse momentum distributions of charged particles produced in the region of the photon fragmentation were measured in non diffractive and diffractive reactions. The non diffractive photoproduction spectrum is very similar to that in hadron hadron collisions at the same c.m. energy in the low p_T region but is significantly harder at higher p_T. The inclusive photoproduction spectrum agrees with the results of a next to leading order QCD calculation. For diffractive reactions, the p_T spectra of the photon dissociation events were measured in two intervals of the dissociated photon mass with mean values $\langle M_X \rangle = 5$ GeV and 10 GeV. In comparison with hadron hadron data the results indicate close similarities between the dissociation of photons and hadrons. For the diffractive reactions the distribution of the dissociated photon mass in the interval $8 < M_X < 21$ GeV was also measured. The shape of the spectrum can be described with the triple pomeron Regge model with the pomeron intercept of $\alpha_{I\!P}(0) = 1.14 \pm 0.01(stat) \pm 0.08(syst)$.

Contents

List of Figures

Chapter 1

Introduction

The nature of light has always troubled philosophers and physicists. In the XIX century the theory developed by Maxwell provided a beautiful explanation of the phenomenon of light in terms of electromagnetic waves. However, very shortly the experiments discovered phenomena like the photoelectric effect and the atomic spectral lines that could not be described by this theory. These effects were finally understood as absorption and emission of photons the light quanta. The initial ideas about interactions of photons with charged matter finally lead to the formulation of the complete theory, the Quantum Electrodynamics (QED). It allowed to calculate with spectacular precision many effects involving photonic reactions, especially in atomic physics. However, once the energy of experimentally available photons reached the GeV range it was observed that in most of the reactions with nucleons the photons manifest hadronic properties. The so called photoproduction interactions showed many features characteristic for hadron hadron reactions in particular large total cross sections, roughly independent of energy [1]. In addition, a copious production of vector mesons in reactions closely resembling elastic scattering of two hadrons was observed. These features found an explanation in the vector meson dominance model (VDM) [2] picturing the photon as a superposition of vector meson states which are responsible for the interaction of the photon with hadrons. This model turned out to be very successful.

A new approach to measuring multiparticle final states produced in high energy collisions was proposed in 1969 by Feynman [3]. He suggested to study the inclusive reactions $AB \to CX$, where only the properties of particle C are measured and those of all other particles, denoted by X, are summed over. The studies of inclusive processes induced by photons and hadrons at the centre of mass (c.m.) energies up to 10 GeV provided further confirmation of the VDM. However, as the beam energies increased the experiments studying the inclusive production of hadrons with high transverse momentum (p_t) showed an excess of those in photoproduction compared to meson induced reactions [4, 5]. The difference was interpreted as a contribution from the process where the photon couples directly to charged constituents of the target hadrons.

Another type of an inclusive process studied extensively in the past was the hadronic reaction $AB \to AX$ where particle A exits intact and retains most of its initial momentum [6, 7]. This reaction is of diffractive nature. It is similar to the elastic scattering, where one of the particles emerges as a dissociated system X. The single dissociation process has been also studied in photon nucleon collisions. The measurements of the reaction $\gamma p \to Xp$ at the c.m. energy $11.8 < W < 16.6$ GeV [8] indicate that the diffractive photon dissociation is very similar to the dissociation of hadrons in terms of the distribution of the square of the

four momentum exchanged by the proton and the mass of the state X. Thus, these results confirm the validity of the VDM also for the single diffractive reactions.

As described in this short historical introduction the experiments at c.m. energies of the order of 1 GeV brought the discovery of the hadronic character of the photoproduction collisions. The increase of the energy by one order of magnitude allowed to observe signs of the direct photon processes. What happens if the c.m. energy is increased by another order of magnitude? Are the photoproduction interactions just like what was observed at lower energies or should some new phenomena become apparent? Is the VDM still adequate for the description of majority of the inclusive photoproduction reactions? Does the contribution from direct photon component becomes stronger? How does the rate of high p_t particle production in photoproduction compare to hadronic reactions? Does the theory account for the observed effects? How do the diffractive photoproduction reactions behave? Are they still very similar to hadronic diffraction as expected from the VDM? These and similar questions are addressed in the following thesis presenting the study of the properties of photon proton reactions at HERA with the ZEUS detector.

This thesis describes the measurement of the inclusive transverse momentum distribution of charged particles produced in the laboratory pseudorapidity range $-1.2 < \eta < 1.1$ [1] in non diffractive photoproduction reactions at an average c.m. energy of $\langle W \rangle = 180$ GeV. In the γp system boosted in the laboratory frame by 2 - 2.2 rapidity units this η interval approximately corresponds to $-3.3 < \eta_{c.m.} < -0.7$, where negative $\eta_{c.m.}$ values indicate the photon fragmentation region. The obtained p_t spectrum is compared to the results from photoproduction experiments at lower c.m. energies and to hadron hadron collisions at similar energy. In the region of high transverse momenta the data is confronted with the prediction of the Quantum Chromodynamics (QCD) - the currently established theory of hadronic interactions. The theoretical calculations have been performed in the next to leading order approximation and they include the contribution from the point like photon processes.

A large part of this thesis is dedicated to the studies of diffractive photoproduction processes. It presents the measurement of the invariant mass distribution of the diffractively dissociated photons in the interval $8 < M_X < 21$ GeV. The analysis was performed for the reaction $\gamma p \to Xp, XN$, were N denotes a nucleonic system with mass $M_N < 2$ GeV, at an average c.m. energy $\langle W \rangle = 200$ GeV. The results are compared to similar measurements in $p\bar{p}$ collisions. The comparison with other photoproduction results is performed in the framework of the Regge model allowing to relate the M_X behaviour to the W dependence of the total and the elastic cross sections.

The last analysis presented in this thesis concerns the subject that has not yet been systematically studied, namely the properties of hadronic final state in diffractive photon dissociation. The inclusive p_t spectra of charged particles emitted in the photon fragmentation region were measured in the diffractive reactions $\gamma p \to Xp, XN$ were N denotes a nucleonic system with $M_N < 1$ GeV. The measurement was performed at $\langle W \rangle = 180$ GeV in two intervals of the dissociated photon mass with mean values $\langle M_X \rangle = 5$ GeV and 10 GeV. The results are used for the comparison of the diffractive dissociation of photons with that of hadrons.

The measurements of the inclusive p_t spectra in diffractive and non diffractive photoproduction reactions were performed with the same experimental setup and very similar analysis techniques using the data collected by ZEUS in 1993. Therefore, these measurements will be presented together in this thesis.

The analysis of M_X distribution in diffractive photoproduction was done using the data collected in 1994 after the commissioning of the ZEUS proton remnant tagger that played a crucial role in the measurement.

The thesis is organized as follows. Chapter 2 contains a short introduction to the physics of photon induced reactions and the models used to describe them. In chapter 3 the basis of the presented measurements are introduced. Chapter 4 describes the experimental apparatus: the HERA collider and the ZEUS detector. The online trigger and the offline filtering used to select the events for the analysis are presented in chapter 5. The next chapter contains a description of the Monte Carlo simulation programs used in this study. Chapter 7 presents the experimental techniques used to identify the diffractive reactions at ZEUS and to determine the mass of the dissociated photon system. Chapters 8 and 9 are dedicated to the measurements of the inclusive p_t spectrum and the M_X distribution respectively. They contain a detailed description of the final data selection, the acceptance correction, systematic uncertainties and the results. In chapter 10 the results are discussed. The final conclusions are given in chapter 11.

[1] Pseudorapidity η is calculated from the relation $\eta = -ln(tan(\theta/2))$, where θ is a polar angle calculated with respect to the proton beam direction.

Chapter 2

Photon–proton interactions

2.1 Vector meson dominance model

The fixed target experiments revealed a number of similarities between photon hadron and hadron hadron interactions [1]. The total cross section for both types of reactions shows resonance structures at beam energies below 3 GeV and is approximately constant above. Although the photoproduction cross sections are lower than hadronic ones by two orders of magnitude, they are much higher than expected for a purely electromagnetic particle. The photon cross sections on neutrons and protons were measured to be almost the same, indicating that the interactions do not depend primarily on the charge of the target. A number of other interesting features were observed including shadowing in photoproduction on nuclei and a copious production of neutral vector mesons in the process similar to elastic hadron hadron scattering.

The observed effects suggested that the physical photon $|\gamma\rangle$ can be considered a superposition of two states: a bare photon $|\gamma_B\rangle$ and a small hadronic component $|h\rangle$ which undergoes conventional hadronic interactions:

$$|\gamma\rangle = \sqrt{Z_3}|\gamma_B\rangle + \sqrt{\alpha}|h\rangle. \tag{2.1}$$

where $\alpha = 1/137$ is the electromagnetic coupling constant and Z_3 is introduced to assure proper normalization. Although the probability of finding the photon in the hadronic state is small, it dominates in the interactions with hadrons due to very large hadron hadron cross sections. The hadronic component $|h\rangle$ should have the same symmetry quantum numbers as the photon and the copious photoproduction of the vector mesons ρ^0,ω and ϕ suggest that they provide very important contribution to $|h\rangle$. The assertion that these three vector mesons are responsible for hadronic interactions of high energy photons is the hypothesis of a vector meson dominance model (VDM) [2]. The inclusion of other hadronic states to $|h\rangle$ is referred to as generalized vector meson dominance (GVDM) [9]. According to the VDM:

$$|h\rangle = \sum_{V=\rho^0,\omega,\phi} \frac{\sqrt{4\pi}}{f_V}|V\rangle. \tag{2.2}$$

The factors f_V indicating the coupling strength of the photon to the vector meson V were measured in a number of photoproduction experiments. However, the most precise values come from e^+e^- annihilation experiments: $f^2_{\rho^0}/4\pi = 2.20 \pm 0.06$, $f^2_\omega/4\pi = 18.1 \pm 1.8$ and $f^2_\phi/4\pi = 13.2 \pm 0.6$ [1].

The VDM may be intuitively understood in the following way. The photon propagating in free space fluctuates into a virtual vector meson state. According to the Heisenberg principle the time allowed for this fluctuation is of the order

$$t_f \approx \frac{1}{\Delta E} \approx \frac{2k}{m_V^2}, \tag{2.3}$$

where k is the photon energy in the target rest frame and m_V is the mass of the vector meson. If the distance that this virtual vector meson state can travel, r_f, is much larger than the nucleon size, $r_{nucl} \approx 1$fm, the resulting interaction may look like a hadronic collision. Already at $k = 10$ GeV the fluctuation time is such that $r_f \approx 7$ fm and at HERA energies it is of the order $r_f \approx 10^4$ fm. Intuitively, the relative probabilities of the photon fluctuation into the different vector mesons should depend on the effective charge of the valence quarks squared. This naive consideration indicates the relative ratios of ω and ϕ to ρ^0 contribution of 1/9 and 2/9 respectively, compared to the mean measured values of 0.12 ± 0.01 and 0.16 ± 0.01 [1].

The VDM approximation allows to connect the cross sections involving high energy photons and nucleons, e.g. protons, $\gamma p \to X$, to analogous reactions of vector mesons, $Vp \to X$:

$$\sigma(\gamma p) = \sum_{V=\rho^0,\omega,\phi} \frac{4\pi\alpha}{f_V^2}\sigma(Vp). \tag{2.4}$$

The vector mesons are short lived particles and the Vp interactions can not be directly studied in the experiments. Fortunately, the additive quark model [10] states, that the properties of interactions between hadrons are determined by their valence quark constituents. Therefore, the behaviour of Vp processes may be determined using the πp and Kp data, e.g.

$$\sigma(\rho^0 p) = \frac{1}{2}(\sigma(\pi^+ p) + \sigma(\pi^- p)), \tag{2.5}$$

$$\sigma(\phi p) = (\sigma(K^+ p) + \sigma(K^- p) \quad \sigma(\pi^+ p)). \tag{2.6}$$

The validity of the VDM for the description of the soft photoproduction has been confirmed in a large number of experiments. Therefore in the following description of soft γp interactions the phenomenological models developed for the hadron hadron interactions will be often used.

2.2 Soft interactions

Once the energy available in hadron hadron and photoproduction experiments was high enough to produce multihadronic final states, it was observed that the momenta of the produced particles were strongly suppressed in the plane transverse to the collision axis [6, 11]. This type of interactions is traditionally referred to as soft processes or limited p_T physics. Although in later experiments [1, 5] the hard processes associated with the production of particles at high transverse momenta were observed, the bulk of hadronic interactions is still attributed to soft type of processes.

The soft hadron hadron interactions may be subdivided into non diffractive and diffractive type of processes.

2.2.1 Non-diffractive processes

Hadronic final states produced in soft non diffractive hadron hadron collisions, $AB \to X$, have the following general properties:

- The average number of charged particles depends approximately logarithmically on the collision energy. The shape of the multiplicity distribution is almost independent of the energy (the KNO [12] scaling) and slightly depends on the type of colliding particles. The models used to describe the shape of multiplicity distributions are usually based only on very general assumptions about the mechanism of particle production, e.g. the lognormal [13] distribution was derived from the statistical analysis of a multi step, scale invariant branching process.

- The transverse momenta of final state hadrons are limited. The p_T distribution has an approximately exponential shape:

$$d\sigma/dp_T^2 \sim exp(-b \cdot \sqrt{p_T^2 + m^2}), \tag{2.7}$$

  where m indicates the particle mass and the slope b depends only weakly on the c.m. energy [11]. The average transverse momenta of particles produced in hadronic interactions at HERA energies are $\langle p_T \rangle \approx 100$ MeV.

- In the longitudinal direction the hadronic final states are distributed approximately uniformly in phase space. This is manifested in the rapidity [1] distribution of final state particles displaying a plateau in the central collision region [6], $y_{c.m.} \approx 0$.

The above properties have not yet found an appropriate explanation in terms of QCD calculations. The following picture may help to understand them intuitively. A hadron may be imagined as a complex cloud of virtual objects, each carrying only a very small fraction of the hadron's momentum. If two hadrons collide, the corresponding clouds meet and some of the constituents interact. The collision energy allows some of the constituents to escape and form the final state hadrons. The number of particles that are created is random, but on average depends on the collision energy. Unless a high momentum transfer occurs between two constituents carrying substantial fractions of the hadrons' momenta no particles with high transverse momentum will be emitted. The p_T of the produced hadrons is to a large extent due to thermal motions within the gas of hadronic constituents. In analogy with the black body radiation one may expect an exponentially falling spectrum of the energy in the transversal plane, $E_T = \sqrt{p_T^2 + m^2}$, with the slope related to the effective temperature of the hadronic gas [14]. In longitudinal direction, randomization leads to equal probabilities of occupying all the available quantum states.

2.2.2 Diffractive processes

Diffraction [7, 6] is the type of periferal scattering of two particles where they exchange only a very small four momentum and no quantum numbers. If the diffractive process is elastic the two colliding particles emerge intact after the reaction. In non elastic diffraction either one

[1] The c.m. rapidity $y_{c.m.} = \frac{1}{2} ln \frac{E+p_Z}{E-p_Z}$, where E and p_Z denote the energy and longitudinal momentum, is defined in the photon proton c.m. system where the positive p_Z correspond to the direction of flight of the protons.

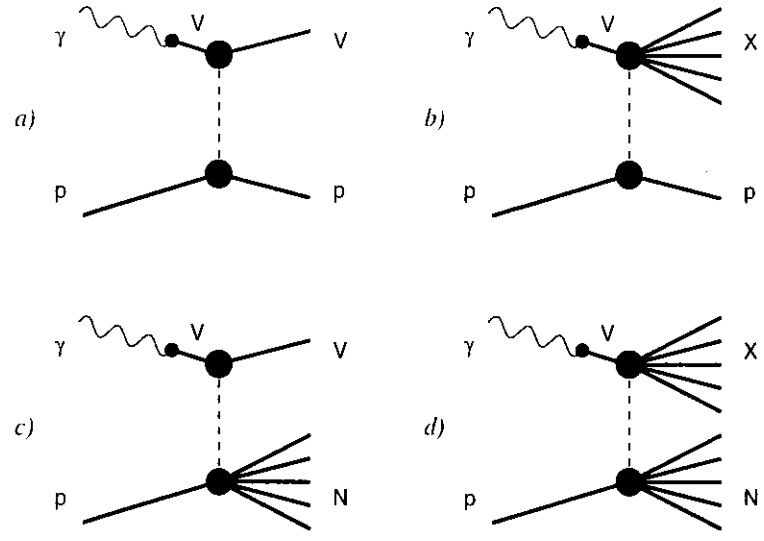

Figure 2.1: *Diffractive photoproduction subprocesses: a) elastic vector meson production, b) photon dissociation, c) proton dissociation and d) double dissociation.*

of the colliding particles or both of them appear as more massive dissociated states. Since only a very small energy and momentum is exchanged, the two particles or the corresponding dissociated states continue to move with the momenta close to those of the initial particles. Therefore in the rapidity distribution the final state particles are grouped in two regions separated by a gap. The presence of a rapidity gap is often used to experimentally identify the diffractive processes.

Elastic scattering

The elastic scattering, $AB \to AB$, is a process where the colliding particles exit intact. The distribution of the squared four momentum exchange, t, has a sharp exponential peak in the forward direction:

$$\left.\frac{d\sigma_{el}}{dt}\right|_{t \approx 0} \sim e^{b_{el}t}, \tag{2.8}$$

where the nuclear slope parameter, b_{el}, depends logarithmically on the collision energy. At HERA energies it has the value $b_{el} \approx 10\,\mathrm{GeV}^{-2}$ [15, 16].

The truly elastic photon proton scattering, the Compton process $\gamma p \to \gamma p$, corresponds to a significant fraction of the total cross section only at energies below the threshold for meson production. Above this, where the properties of the photon are determined by its hadronic component described in the VDM, the quasi elastic vector meson production, $\gamma p \to Vp$, takes over the role of the elastic scattering. It is sketched in Fig. 2.1a with a dashed line denoting the four momentum exchange. To simplify the notation this process will be hereafter called elastic.

Single diffractive dissociation

The single diffractive dissociation, $AB \to AX$, is a process where one of the particles is excited to a more massive state, X, and the other stays intact. It is characterized by an exponential t suppression similar to that in the elastic scattering with a smaller slope, roughly $b_{sd} \approx b_{el}/2$. The spectrum of the dissociated mass, M_X, is dominated by resonant structures at low masses and is smoothly falling at higher values approximately as

$$\frac{d\sigma_{sd}}{dM_X{}^2} \sim \frac{1}{M_X{}^2} \tag{2.9}$$

The M_X is closely related to the fraction of the initial momentum, p_{ini}, that the undissociated particle A retains after the interaction:

$$x = \frac{p}{p_{ini}} \approx 1 - \frac{M_X{}^2 - M_B{}^2}{W^2}. \tag{2.10}$$

where p is the final momentum of particle A and M_B denotes the mass of particle B. The process is clearly identified with diffraction only up to an approximate limit of $M_X{}^2 \approx 0.1\,s$ suggested by the coherence condition [7].

The two types of the single diffractive processes in photoproduction are sketched in Fig. 2.1b and 2.1c. They correspond to the single dissociation of the photon, $\gamma p \to Xp$, and the dissociation of the proton, $\gamma p \to VX$.

The experimental knowledge of the diffractive reactions with the photon dissociation is very poor. Previous measurement of this process was performed in the E612 fixed target experiment at the c.m. energy of $11.8 < W < 16.6$ GeV [8]. The results indicate that the gross features of the diffractive dissociation of the photon resemble diffraction of hadrons in terms of the distributions of t and M_X.

Diffractive double dissociation

In the double dissociation process both colliding particles are converted to more massive states, resembling a combination of two single diffractive excitations, as shown in Fig. 2.1d. The data on this subject is very limited due to experimental difficulties with discriminating between double dissociation process and the non diffractive interactions.

Hadronic final state in diffractive collisions

The studies of particle production properties in diffractive reactions showed that they primarily depend on the mass of the dissociated system, M_X, and not on the overall collision energy [7]. If the diffractive collisions are studied for one value of M_X, the hadronic final states from the decay of the dissociated system X reveal many similarities to the final states in non diffractive collisions. The momenta of produced particles are strongly suppressed in the plane transverse to the collision axis. The rapidity distribution features a central plateau indicating approximately uniform occupation of the longitudinal phase space [17, 18]. The distribution of charged particle multiplicity is similar to that in non diffractive interactions, only at lower energy [18, 19, 7]. This is illustrated with Fig. 2.2 quoted from [18]. The plot shows the mean charged particle multiplicity (n_{ch}) in non diffractive pp and $p\bar{p}$ collisions vs. the c.m. energy $\sqrt{s}$ [20]. This is compared to the average number of charged particles produced in the fragmentation of the system X in the diffractive reaction $pp \to Xp$ at

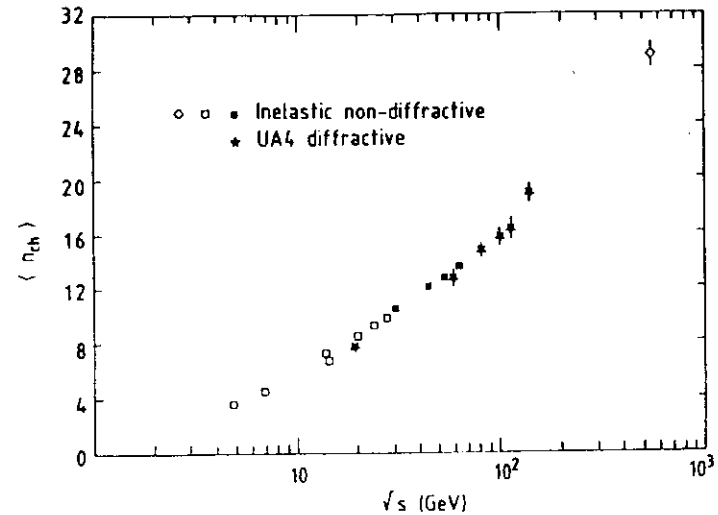

Figure 2.2: *Mean charged particle multiplicity in non diffractive pp and $p\bar{p}$ collisions vs. the c.m. energy [20] compared to the average number of charged particles produced in the fragmentation of the system X in the diffractive reaction $pp \to Xp$ at $\sqrt{s} = 546$ GeV [18].*

$\sqrt{s} = 546$ GeV [18]. The diffractive data points are plotted at $\sqrt{s} = M_X$ and they closely follow the behaviour of the non diffractive data.

All the properties of diffractive final states described above suggest, that it is convenient to think of diffraction as of an exchange of an object that, in collision with dissociating hadron, leads to a similar final state as that in a non diffractive collision of two hadrons.

These properties of the final states in diffractive processes have been observed in hadron hadron experiments. The particle production in diffractive photoproduction has not been systematically studied so far.

2.2.3 Regge phenomenology

The theoretical ideas of Regge [21] lead to the development of a phenomenological model of interactions between hadrons at high energy, also referred to as the Regge theory [11]. This theory explains in relatively simple terms the behaviour of cross sections measured in the experiments. Although very successful in describing the data, it does not provide the explanation of the hadronic processes on such an elementary level as QCD. However, since the QCD calculations can not be performed for the majority of soft processes, one has to rely on the phenomenological models like the Regge theory in the analysis of the data.

The Regge formalism exploits the crossing symmetry between the two reactions sketched in Fig. 2.3. For the two body scattering process, $AB \to CD$, the square of the c.m. energy is $s = (p_A + p_B)^2$, while the square of the four momentum exchange $t = (p_A - p_C)^2$ defines the scattering angle. In the crossed channel, $A\bar{C} \to B\bar{D}$, the roles of the two variables inter-

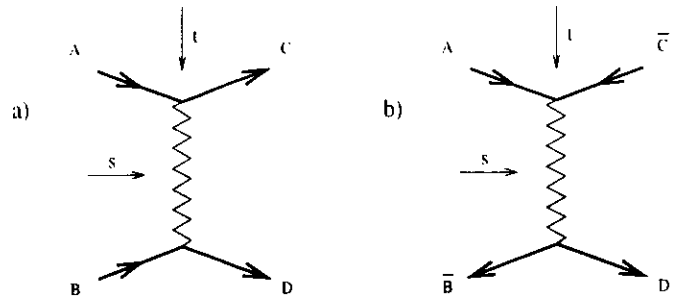

Figure 2.3: *Processes related by crossing symmetry. The s-channel process $AB \to CD$ (a) and t-channel process $A\bar{C} \to \bar{B}D$ (b).*

change, i.e. t is the c.m. energy squared, while s defines the scattering angle. The hypothesis of crossing symmetry states, that since the quantum numbers of the object exchanged in the first process and the intermediate state formed in the second process are the same, the two reactions share a common scattering amplitude.

The hadronic spectroscopy experiments studying the reactions of the type $A\bar{C} \to \bar{B}D$ observed numerous resonances characterized by different values of spin, J, and mass, m, of the intermediate state. Surprisingly, the resonances corresponding to a particular choice of the colliding particles lay on a straight line on the plot of $\alpha = J$ vs. $t = m^2$, the so called Regge trajectory: $\alpha(t) = \alpha(0) + \alpha' \cdot t$. The presence of these resonances is equivalent to the series of poles in the scattering amplitude for the process $A\bar{C} \to \bar{B}D$ at integer values of the spin. This scattering amplitude evaluated for negative values of t and $s \to \infty$ gives the asymptotic behaviour of the crossed channel process $AB \to \bar{C}D$:

$$A(s,t) \overset{s\to\infty}{\sim} \beta(t) \cdot s^{\alpha(t)}, \tag{2.11}$$

and the differential cross section

$$\frac{d\sigma}{dt} \sim \frac{1}{s^2}|A(s,t)|^2 \sim \beta^2(t) \cdot s^{2(\alpha(t)-1)}, \tag{2.12}$$

where $\beta(t)$ depends on the type of the colliding particles. Figure 2.1 presents experimental data confirming this behaviour of the scattering amplitude. The points in the $t < 0$ region correspond to $\alpha(t)$ extracted from the charge exchange reaction $\pi^- p \to \pi^0 n$. They align with the resonances belonging to the ρ trajectory — the intermediate states of the crossed channel process $\pi^-\pi^0 \to \bar{p}n$.

If applied to the case of elastic scattering where $A = C$ and $B = D$ the formalism predicts the following behaviour of the cross section at small $|t|$ [11, 7]:

$$\frac{d\sigma_{el}^{AB}}{dt} \sim s^{2(\alpha(0)-1)} e^{(b_{el}+2\alpha' \ln s)\cdot t} \tag{2.13}$$

The imaginary part of the forward elastic scattering amplitude may be related to the total cross section using the optical theorem [22]:

$$\sigma_{tot}^{AB} \sim s^{\alpha(0)-1} \tag{2.14}$$

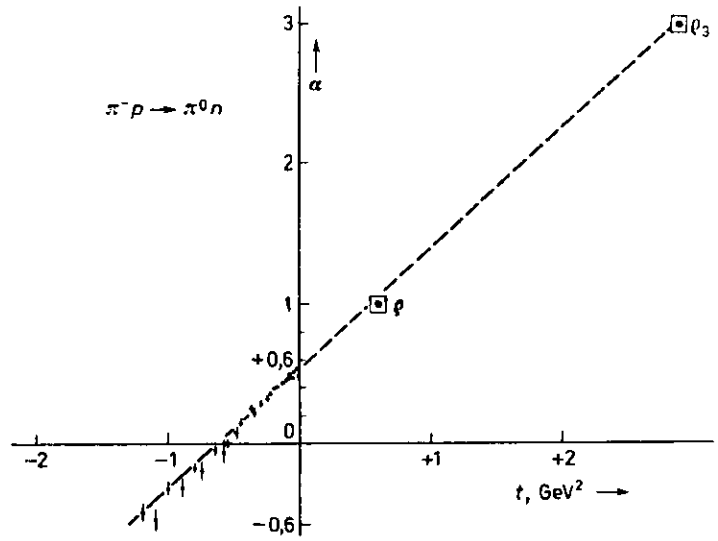

Figure 2.4: *The ρ trajectory [22]. The points in $t < 0$ region come from the analysis of the reaction $\pi^- p \to \pi^0 n$.*

In principle, the full calculation of a cross section should involve summing over all Regge trajectories that can be exchanged in the considered reaction. In practice, two trajectories are sufficient to describe the energy dependence of hadronic and photoproduction cross sections above the resonant region. The reggeon trajectory having the intercept $\alpha_R(0) \approx 0.55$ [23] and the slope $\alpha_R' \approx 1\ \mathrm{GeV}^{-2}$ describes the initial fall of the cross sections as the c.m. energy increases. It corresponds to the exchanges of mesons. The pomeron trajectory was introduced to describe the leveling and slight growth of the cross sections at high energy. It was named after Pomeranchuk who predicted the asymptotic behaviour of the cross sections in 1958 [24]. A fit to the hadronic data indicates a pomeron intercept of $\alpha_P(0) = 1.08$ [23]. A similar value was obtained including the $p\bar{p}$ total cross section at the c.m. energy $\sqrt{s} = 1.8$ TeV measured by E710 [25] experiment. CDF [26] has recently repeated the $p\bar{p}$ cross section measurements at $\sqrt{s} = 1.8$ TeV and found a significantly higher value than E710, which would imply a pomeron intercept of $\alpha_P(0) = 1.11$. The discrepancy between the two measurements has not yet been resolved. The pomeron trajectory corresponds to the exchange of the vacuum quantum numbers and is therefore believed to be responsible for all the diffractive reactions. The pomeron slope is approximately $\alpha_P' \approx 0.25\ \mathrm{GeV}^{-2}$. In the crossed channel the pomeron trajectory should correspond to a series of hadronic resonances called glueballs. A candidate for such a state with spin $J = 2$ has been observed at mass $m \approx 1900$ MeV [27].

The same values of the pomeron and the reggeon intercepts successfully describe also the total cross sections in photoproduction, as illustrated in Fig. 2.5. The plot includes also the results of the measurements at HERA [28, 29]. The ALLM parametrization [31] uses a slightly lower value of $\alpha_P(0) = 1.015$. Figure 2.6 demonstrates that also the cross sections for the elastic ρ^0 photoproduction are consistent with the expectations from the

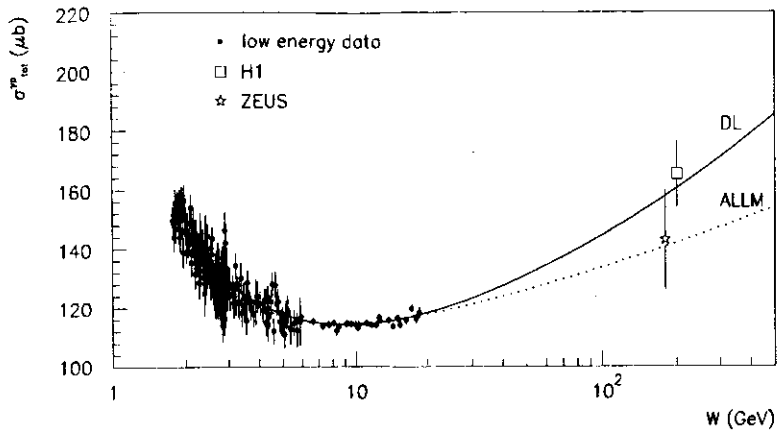

Figure 2.5: *The total photoproduction cross section [28, 29, 30] as a function of the c.m. energy W. The lines are the results of a Regge type of parametrization with $\alpha_P(0) = 1.0808$ (solid) [23] and $\alpha_P(0) = 1.015$ (dotted) [31].*

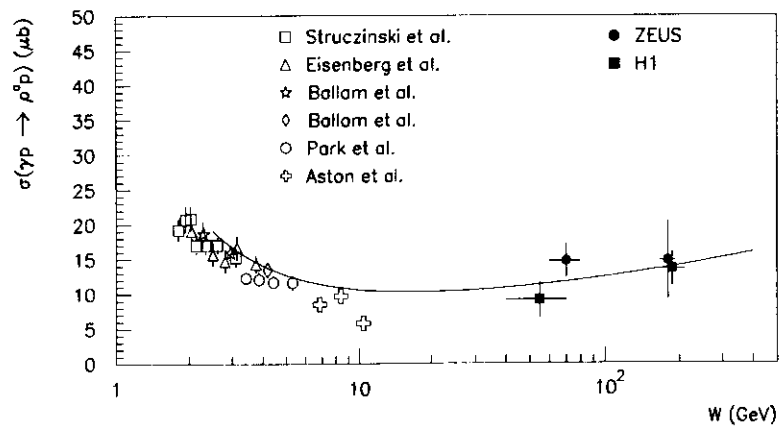

Figure 2.6: *Elastic ρ^0 photoproduction cross section [34, 28, 15, 16] as a function of the c.m. energy W. The prediction of a model [32] based on a Regge type of parametrization is also shown.*

Regge phenomenology. The line shows the parametrization [32] of the form similar to the equation (2.13) using $\alpha_P(0) = 1.08$. The results from HERA [28, 15, 16] are also included.

The Regge theory allows to predict also some features of the inclusive reactions of the type $AB \to CX$. Thanks to Müller's extension of the optical theorem, the high energy asymptotic behaviour of the corresponding cross sections may be derived from the forward amplitude for an elastic three body process $AB\bar{C} \to AB\bar{C}$. The calculations show that if particle C

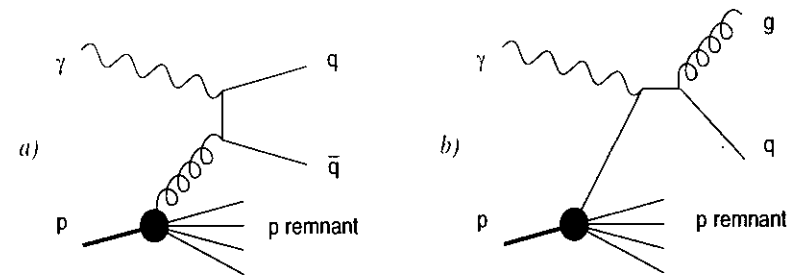

Figure 2.7: *The diagrams of the direct photon interactions: the boson gluon fusion (a) and the QCD Compton process (b).*

is produced in the central region of the collision ($y_{c.m.} \approx 0$), the double Regge limit applies, predicting a plateau in the rapidity distribution observed in non diffractive events. However, if particle C carries the same quantum number and a large fraction of the momentum of A, the reaction describes the diffractive single dissociation process. The behaviour of the inclusive cross section may be then calculated in the triple pomeron asymptotic limit of $M_X^2 \to \infty$ and $s/M_X^2 \to \infty$ [7]:

$$\frac{d^2\sigma}{dtdM_X{}^2} \sim s^{2\alpha_P(0)}(\frac{1}{M_X{}^2})^{\alpha_P(0)} exp(b_\circ + 2\alpha'_P ln\frac{s}{M_X{}^2})t \qquad (2.15)$$

A large number of hadron hadron experiments have confirmed that the above formula correctly describes the diffractively dissociation above the region of low mass resonances. Even at very large c.m. energies of $\sqrt{s} = 1.8$ TeV the value of the pomeron intercept extracted from the M_X spectrum shape [33] is consistent with that obtained from the elastic and the total cross sections.

2.3 Hard processes

Hard processes which occur in high energy photoproduction interactions [35, 36] are characterized by large momentum transfers or by the production of large invariant masses. These processes may be calculated in QCD due to the presence of a hard scale allowing for perturbative expansion. Experimentally, hard interactions can be identified by the emission of high transverse momentum particles, high transverse energy jets [2] or the production of heavy flavour hadrons. The hard photoproduction processes are generally subdivided into direct and resolved photon interactions.

2.3.1 Direct photon interactions

The photon can participate in the hard subprocess by coupling directly to a charged parton inside of the proton. In leading order perturbation theory two channels contribute: the

[2] A jet is a group of collimated particles emitted from a high energy interaction. At HERA the jets are usually defined as groups of particles carrying high total transverse energy within a cone in pseudorapidity and azimuthal angle $\sqrt{\eta^2 + \phi^2} < R$. The total transverse energy is a scalar sum of the transverse component of the particles' energies.

boson gluon fusion (BGF) and the QCD Compton process diagrammed in Fig. 2.7. The quarks and gluons emitted from the hard subprocess shown in Fig. 2.7 convert into final state particles in the process of hadronization described later. The cross section for the direct process depends primarily on the probability for the hard partonic interaction to occur. In the lowest order (LO) of the perturbative series it may be written as the convolution of the probability of finding parton a inside the proton, $f_{a/p}$, and the cross section for the photon parton process, $\sigma_{\gamma a}$:

$$\sigma^{dir}_{\gamma p} = f_{a/p}(x_p) \otimes \sigma_{\gamma a}(x_p), \tag{2.16}$$

where x_p denotes the fraction of the proton momentum carried by the struck parton. For simplicity the dependence on the factorization scale connected with the parton density $f_{a/p}$ and the QCD renormalization scale is not indicated.

2.3.2 Resolved photon interactions

A large fraction of hard photoproduction interactions are due to the resolved processes where the photon does not participate directly in the hard subprocess but through a parton associated with its structure. If hadronization effects are neglected the cross section for the resolved photon interactions may be approximately written as the convolution of the probability of finding parton a inside the photon, $f_{a/\gamma}$, the probability of finding parton b inside the proton, $f_{b/p}$, and the cross section for the parton parton process, σ_{ab}:

$$\sigma^{res}_{\gamma p} = f_{a/\gamma}(x_\gamma) \otimes \sigma_{ab}(x_\gamma, x_p) \otimes f_{b/p}(x_p), \tag{2.17}$$

where x_γ denotes the fraction of the photon momentum carried by the parton a and x_p denotes the fraction of the proton momentum carried by the parton b. The scale dependence is not indicated.

The partonic structure of the photon was studied in the past in interactions of highly virtual and almost real photons in e^+e^- colliders [36], where the virtual photon was acting as a point like probe used to test the structure of the almost real photon.

Recalling the close analogies between photon hadron and hadron hadron interactions described in the soft regime by the VDM one could expect that the structure of the photon seen in hard interactions is also similar to that of the vector meson. However, in addition to the hadronic component, a contribution from an anomalous photon process was observed. The anomalous part is due to the hard, perturbatively calculable splitting of a point like photon into a quark antiquark pair that participates in the interaction with the proton before forming a hadronic state. The anomalous part of the photon structure function is fully calculable, while the hadronic component has to be inferred from the experiment. In the interactions involving partons carrying small fraction of the photon momentum the hadronic component dominates. However at high x_γ values or very hard interaction scales the anomalous photon component is expected to be of primary importance. The two types of resolved photon interactions are schematically shown in Fig. 2.8.

2.3.3 Hadronization

Hard processes are modelled in perturbative QCD in terms of interactions of quarks and gluons carrying colour charge. However, as the result of such interactions colour neutral hadrons are emitted. The transition from partons to hadrons is a very complicated process generally referred to as hadronization. Although the hadronization is not yet understood

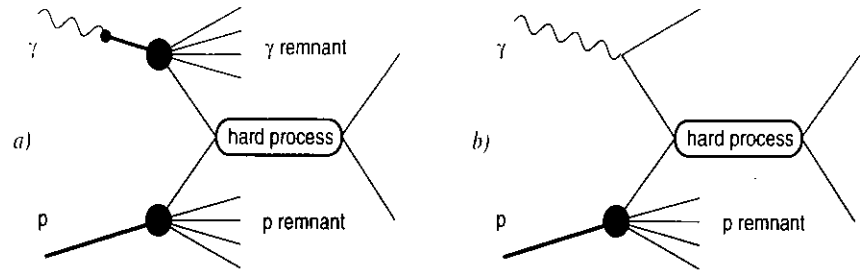

Figure 2.8: *The diagrams of the resolved photon interactions: the hadronic component (a) and the anomalous part (b).*

in terms of elementary QCD calculations, a number of general facts is known [22, 11]. The primary reason for the hadronization is the QCD confinement forbidding coloured objects to be emitted as free particles. The hadronization occurs on a longer time scale than the hard subprocess and therefore does not strongly influence the cross sections calculated on the partonic level. Due to the local parton hadron duality [37] the dynamics of the hadronic final state is closely related to the partonic level. This important property justifies for example the usage of jets to study partonic processes. The properties of the hadronization are believed to be universal regardless of the details of the hard subprocess, the overall energy and the type of colliding particles. This justifies the use of hadronization models developed for e^+e^- physics also in case of hadron hadron and γp interactions.

2.3.4 Experiments on hard photoproduction

The inclusive single particle cross sections in photoproduction were previously measured by NA14 [1] and WA69 [5] fixed target experiments at c.m. energies $9.7 < W < 16.8$ GeV and $11.5 < W < 17.9$ GeV respectively. The photoproduction data were compared to the results obtained in the same experimental setup using pion and kaon beams. Both experiments observed a clear excess of high p_t particles produced in photon induced reactions relative to what was expected for the hadronic component of the photon estimated from the meson data. This difference was attributed to the contribution of the direct photon interactions and could be successfully described by the QCD calculations. Figure 2.9 presents an example of such comparison from [5]. The plot shows the inclusive p_t spectrum of charged particles in photoproduction reactions compared to the shape measured using the hadron beam.

A number of unique measurements of hard photoproduction reactions has been recently performed at HERA. The studies of events with hard jets in photoproduction have clearly demonstrated the presence of the direct photon component in addition to the resolved one [38]. This is illustrated in Fig. 2.10 with early results from ZEUS. The measurement was performed for γp c.m. energies ranging from 130 to 250 GeV. The events with two jets with transverse energies $E_T^{jet} > 5$ GeV were used to study the distribution of the variable

$$x_\gamma = \frac{\sum_{jets} E_T{}^{jet} e^{-\eta^{jet}}}{2yE_e}, \tag{2.18}$$

where η^{jet} denotes the pseudorapidity of the jet, E_e denotes the electron energy and y is the

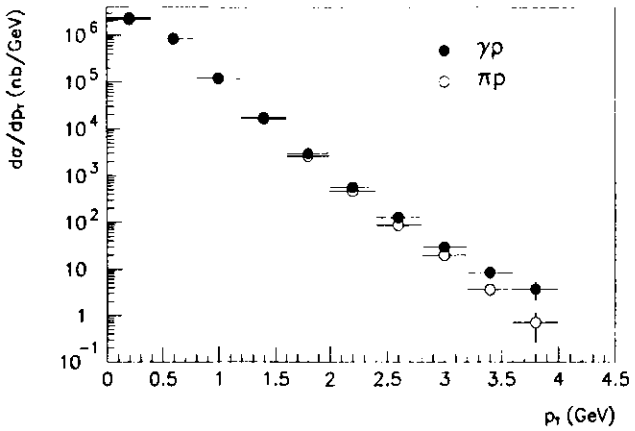

Figure 2.9: *The inclusive p_T spectrum of charged particles measured in photoproduction at c.m. energy of $11.5 < W < 17.9$ GeV from WA69 experiment [5] (full points). It is compared to the shape obtained using the hadron beam (open circles).*

fraction of the electron momentum carried by the interacting photon. The x_γ estimates the fraction of the photon momentum involved in the hard scatter. For the direct photon process it is expected to be close to one, while for the resolved photon interactions it should be much lower. As shown in Fig. 2.10 the observed x_γ distribution has clearly two components. The MC simulation of the resolved photon interactions explains the region of low x_γ but can not account for the peak at high x_γ which is therefore attributed to direct photon collisions. It is confirmed by the MC simulation including the direct photon component.

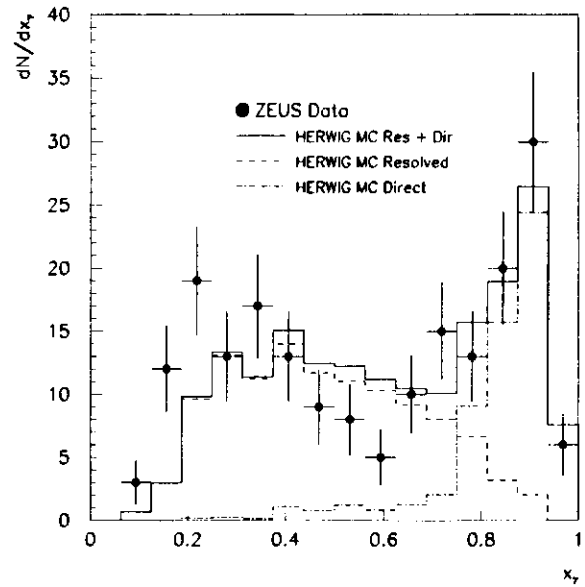

Figure 2.10: *The uncorrected x_γ distribution of dijet photoproduction events from ZEUS [38]. The dashed line indicates the MC simulation of the resolved photon contribution, the dashed dotted line corresponds to the direct photon component and the solid line is the sum of the two.*

Chapter 3

Photoproduction at HERA

In this chapter the variables used at HERA to describe the kinematics of electron proton interactions are introduced and the principles allowing to study photoproduction physics using ep collisions are explained. The last section of this chapter contains the discussion of the basis of the measurements presented in this thesis.

3.1 Kinematics of ep collisions at HERA

The majority of ep collisions at HERA [39] are due to the exchange of the virtual photon, γ^*, a process sketched in Fig. 3.1. The definitions of the variables used to describe the kinematics of such process at HERA are summarized in Table 3.1.

3.2 Relating ep and γp cross sections

The cross section for photon mediated ep scattering is typically written in a double differential form [10]:

$$\frac{d^2\sigma^{ep}}{dydQ^2} = \frac{1}{Q^4}\cdot\left[y\left(1-\frac{2m_e^2}{Q^2}\right)xF_1(y,Q^2)+\frac{(1-y)}{y}\cdot F_2(y,Q^2)\right], \qquad (3.1)$$

where $F_1(y,Q^2)$ and $F_2(y,Q^2)$ are the proton structure functions. The structure functions may be expressed in terms of the cross sections for scattering of transversely and longitudi-

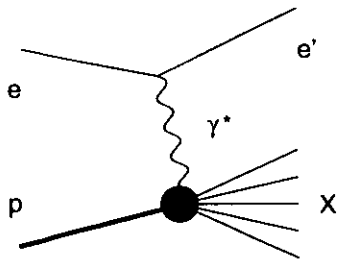

Figure 3.1: *Basic diagram of ep interaction.*

energy, mass and 4-momentum of the incoming proton	E_p 820 GeV, m_p, $p = (E_p, \vec{p})$
energy, mass and 4-momentum of the incoming electron	E_e 26.7 GeV (1993), E_e 27.5 GeV (1994), m_e, $k = (E_e, \vec{k})$
energy, 4-momentum and the polar angle of the scattered electron	$E_{e'}$, $k' = (E_{e'}, \vec{k'})$, θ
squared total center of mass energy	$s = (k+p)^2 \approx 4E_eE_p$, $\sqrt{s} \approx 300$ GeV
4-momentum of the exchanged photon	$q = k - k'$
photon virtuality	$Q^2 \quad -q^2 \approx 4E_eE_e\sin^2\frac{\theta}{2}$
fraction of the electron energy taken by the photon in the proton rest frame	$y = \frac{p\cdot q}{p\cdot k} \approx 1 - \frac{E_{e'}}{E_e}\cos^2\frac{\theta}{2}$
Bjorken x scaling variable	$x = \frac{Q^2}{2p\cdot q}$
squared invariant mass of the hadronic system equivalent to γp c.m. energy	$W^2 = (q+p)^2 = sy - Q^2 + m_p^2$
lower kinematical limit on Q^2	$Q^2_{kin\ min} \approx \frac{m_p^2y^2}{1-y}$

Table 3.1: *Definitions of variables used to describe the kinematics of ep interactions at HERA.*

nally polarized virtual photons on the proton, $\sigma_T^{\gamma^*p}(y,Q^2)$ and $\sigma_L^{\gamma^*p}(y,Q^2)$ respectively:

$$xF_1 = \frac{1}{4\pi^2\alpha}\frac{Q^2}{2}\sigma_T^{\gamma^*p}, \qquad F_2 = 2xF_1 = F_L = \frac{1}{4\pi^2\alpha}\frac{Q^2}{2}\sigma_L^{\gamma^*p}. \qquad (3.2)$$

This allows to express the ep cross section in the form:

$$\frac{d^2\sigma^{ep}}{dydQ^2} = \frac{\alpha}{2\pi}\cdot\frac{1}{Q^2}\cdot\left[\left(\frac{1+(1-y)^2}{y}-\frac{2(1-y)}{y}\cdot\frac{Q^2_{min}}{Q^2}\right)\cdot\sigma_T^{\gamma^*p}(y,Q^2) + \frac{2(1-y)}{y}\cdot\sigma_L^{\gamma^*p}(y,Q^2)\right]. \qquad (3.3)$$

The above equation is often referred to as the equivalent photon expression (EPE) for ep scattering since it reduces the ep collision to the γ^*p interaction. As $Q^2 \to 0$ the cross section for transversely polarized virtual photons approaches that for real photons, $\sigma_T^{\gamma^*p}(y,Q^2) \to \sigma^{\gamma p}(W_{\gamma p} \approx \sqrt{ys})$, while the cross section for longitudinally polarized photons $\sigma_L^{\gamma^*p}(y,Q^2) \sim Q^2 \to 0$. For very low $Q^2 \ll m_\rho^2$ the deviations from real photon cross sections become negligible allowing to express the ep cross section in terms of real photoproduction cross section. After integration between some Q^2_{min} and some Q^2_{max}, it yields

$$\frac{d\sigma^{ep}}{dy} = \frac{\alpha}{2\pi}\cdot\left[\frac{1+(1-y)^2}{y}\ln\frac{Q^2_{max}}{Q^2_{min}}-\frac{2(1-y)}{y}\cdot\left(1-\frac{Q^2_{min}}{Q^2_{max}}\right)\right]\cdot\sigma^{\gamma p}(y). \qquad (3.4)$$

If only the logarithmic term is kept the above relation is equivalent to the Weizsäcker-Williams approximation [11].

Thus, the photoproduction processes may be studied in ep interactions where the electron is scattered under very small angles implicating low Q^2_{max}. It is convenient to select events where y is limited to a narrow interval such that the photoproduction cross section may be approximated with a constant, $\sigma^{\gamma p}(y) \approx \sigma^{\gamma p}$. The ep cross section may be then decomposed into a factor defining the flux of the photons in the electron beam, $f_{\gamma/e}$, and the photoproduction cross section:

$$\sigma^{ep} = f_{\gamma/e} \cdot \sigma^{\gamma p} \tag{3.5}$$

3.3 Inclusive measurements of photoproduction

In the following thesis two measurements of photoproduction reactions at HERA are presented: the inclusive p_t spectrum of charged particles in diffractive and non diffractive interactions and the distribution of diffractively dissociated photon mass. Both measurements were performed using the events where the scattered electron was detected in the electron calorimeter of the ZEUS luminosity monitor (LUMIE). This calorimeter accepts electrons scattered at angles from zero up to about 5 mrad. This limits the virtuality of the exchanged photon to the interval between the kinematical limit $Q^2_{min} = Q^2_{kin\ min} = 4 \cdot 10^{-8}$ GeV^2 and $Q^2_{max} = 0.02$ GeV^2 with a median $\langle Q^2 \rangle = 6 \cdot 10^{-4}$ GeV^2. The events with an electron detected in LUMIE are also referred to as tagged events.

By cutting on the energy of the scattered electron, $E_{e'}$, measured in LUMIE a limited interval of $y \approx E_\gamma/E_e = (E_e - E_{e'})/E_e$ were selected. In the first of the presented analyses the LUMIE energy was required to satisfy $15.2 < E_{e'} < 18.2$ GeV limiting the γp c.m. energy to the interval $167 < W < 191$ GeV with a mean value of $\langle W \rangle = 180$ GeV. In the second study, due to a different beam orbit and LUMIE acceptance in 1994, the interval was changed to $12 < E_{e'} < 18$ GeV, which corresponds to $176 < W < 225$ GeV and a mean value of $\langle W \rangle = 200$ GeV.

The hadronic final state of the γp interactions was studied in the main ZEUS detector. In the first analysis the central tracking chambers were used to measure the transverse momentum distribution of charged particles produced in the laboratory pseudorapidity range $-1.2 < \eta < 1.4$. In the γp system boosted in the laboratory frame by 2 – 2.2 rapidity units this range approximately corresponds to $-3.3 < \eta_{c.m.} < -0.7$, where negative $\eta_{c.m.}$ values define the photon fragmentation region. The p_t distributions of charged particles were studied for non diffractive and diffractive reactions separately. The diffractive interactions $\gamma p \to Xp, XN$ were $M_N < 1$ GeV were identified by a rapidity gap between the dissociated photon state X and the outgoing proton or a nucleonic system N. Experimentally it was required that the central ZEUS calorimeter (CAL) registers no energy deposits exceeding 100 MeV in the pseudorapidity range of $2 < \eta < 1.3$. In the further text the events fulfilling the rapidity gap cut will be also called diffractive like events and the events that fail this cut will be called non diffractive like or non rapidity gap events. The topology of the studied collisions is show in Fig. 3.2a and 3.2b. The rapidity distributions of the final state particles in diffractive and non diffractive photoproduction at $W = 200$ GeV were simulated using the EPSOFT Monte Carlo program (see section 6.4). The distribution of hadrons in non diffractive events is symmetric around the hadronic c.m. at rapidity $y = 2.1$. The diffractive distribution is shown for the process $\gamma p \to XN$, where $M_X = 10$ GeV and $M_N = 3$ GeV. The approximate position of the rapidity gap required in the selection of diffractive like events is also indicated. In this analysis the p_T spectra in diffractive-like

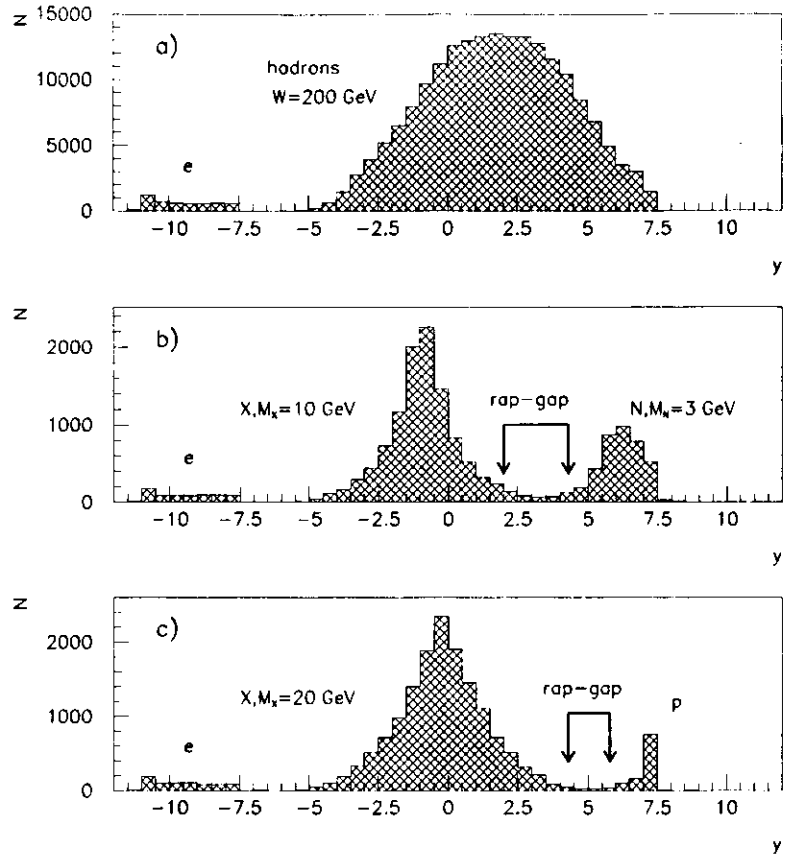

Figure 3.2: *Rapidity distribution of final state particles in non diffractive (a) and diffractive (b and c) photoproduction collisions at $W = 200$ GeV simulated using the EPSOFT MC program. The diffractive distribution is shown (b) for the process $\gamma p \to XN$, where $M_X = 10$ GeV and $M_N = 3$ GeV, and (c) for the process $\gamma p \to Xp$, where $M_X = 20$ GeV. The approximate position of the rapidity gap required in the selection of diffractive like events using CAL (b) and PRT1 (c) is indicated with arrows.*

events were measured in two intervals of the dissociated photon mass with mean values $\langle M_X \rangle = 5$ GeV and 10 GeV. The invariant mass of the dissociated photon system was reconstructed using CAL. The limited acceptance and the resolution of the detector was corrected for by using the MC simulation. It also included the correction for limited efficiency of the rapidity gap cut to distinguish between diffractive and non diffractive processes, i.e. based on the results of the MC simulation the remaining non diffractive contamination in the rapidity gap sample and the diffractive contamination in the non rapidity gap sample

were compensated. The final results will be presented in terms of a double differential rate of charged particle production in an average event of a given type, i.e. in an average non diffractive γp collision at $\langle W \rangle = 180$ GeV, an average diffractive collision with $\langle M_X \rangle = 5$ GeV and a diffractive collision with $\langle M_X \rangle = 10$ GeV:

$$\frac{1}{N_{ev}} \cdot \frac{d^2N}{dp_T^2 d\eta} = \frac{1}{N_{ev}} \cdot \frac{1}{2p_T \Delta\eta} \cdot \frac{\Delta N}{\Delta p_T},$$

where ΔN denotes the number of charged particles produced in N_{ev} events within pseudorapidity and transverse momentum intervals of $\Delta\eta$ and Δp_T. Defining the result in terms of characteristics of an average photoproduction event of a given type has a number of advantages: there is no need to calculate luminosities, cross sections and flux factors to convert the ep cross sections to γp cross sections. Also the electron tagging efficiency does not have to be considered because it is the same for all types of photoproduction processes and therefore does not introduce biases to the data sample. These simplifications significantly reduce the number of sources of potential systematic uncertainties and make the measurement more reliable.

In the second study the distribution of the dissociated photon mass was measured in diffractive reaction $\gamma p \to Xp, XN$, where the mass of the nucleonic system is limited to $M_N < 2$ GeV. The experimental procedure was similar to that applied in the first analysis. In the events with rapidity gap the diffractive mass of the dissociated photon was measured in the calorimeter. The limited acceptance and the resolution of the detector, as well as the limited efficiency of the rapidity gap cut to distinguish between diffractive and non diffractive processes were corrected for with the MC simulation. However, in comparison with the first study this analysis profited from significant improvements of the detector and the data correction method. The events with a rapidity gap were selected using the commissioned in 1991 proton remnant tagger (PRT1) detecting particles emitted in the laboratory pseudorapidity interval of $4.3 < \eta < 5.8$. It allowed to select diffractive reactions with photon dissociated masses as high as 21 GeV and to reduce the contribution of proton dissociation. The topology of the selected rapidity gap events is illustrated in Fig. 3.2c showing the rapidity distribution of the final state particles from the diffractive process $\gamma p \to Xp$, where $M_X = 20$ GeV. In this analysis the data correction factors were derived using the EPSOFT Monte Carlo program to simulate the soft non diffractive photoproduction collisions. This generator was tuned to the preliminary results from ZEUS. In comparison with general purpose MC simulation programs EPSOFT provided a better description of the hadronic final state in soft non diffractive photoproduction collisions at HERA. It therefore allowed for a more precise correction of the rapidity gap data sample for the non diffractive contamination. The final result of this measurement will be presented in terms of single differential cross section for the diffractive reaction $\gamma p \to Xp, XN$, where $M_N < 2$ GeV, relative to the total photoproduction cross section:

$$\frac{1}{\sigma_{tot}^{\gamma p}} \cdot \frac{d\sigma_{diff}^{\gamma p}}{dM_X} = \frac{f_{\gamma/e}}{\sigma_{tot}^{ep}} \cdot \frac{d\sigma_{diff}^{ep}}{f_{\gamma/e} dM_X} = \frac{\mathcal{L} Acc_{tag}}{N_{tot}} \cdot \frac{\Delta N_{diff}}{\mathcal{L} Acc_{tag} \Delta M_X} = \frac{1}{N_{tot}} \cdot \frac{\Delta N_{diff}}{\Delta M_X}$$

The photon flux factor $f_{\gamma/e}$, the integrated luminosity $\mathcal{L}$ and the electron tagger acceptance Acc_{tag} cancel. Therefore the measurement may be performed by directly comparing the numbers of tagged diffractive ep events ΔN_{diff} falling into the ΔM_X bin with the total number of tagged ep events N_{tot}. Like in the case of the first study this significantly simplifies the analysis and reduces the systematic uncertainty of the result.

In the measurements presented in this thesis no correction for the electroweak radiation is performed. In the considered W range, the QED radiation effects may lead up to 2% change in the number of tagged photoproduction events and do not depend on the type of the γp process [12, 28]. Since all the measurement results are quoted relative to the number of observed events and not in terms of absolute cross sections, they are practically insensitive to the electroweak radiation effects.

Chapter 4

The experimental apparatus

4.1 The HERA collider

The Hadron Electron Ring Accelerator HERA is the world's first electron proton collider installed in the DESY laboratory in Hamburg, Germany. It consists of two storage rings placed in a 6.3 km long tunnel 10–25 m underground. The energy of the proton beam may be as high as 820 GeV. This is achieved due to the application of superconducting dipole magnets providing the field of 4.6 T to keep the protons in the circular orbit. The electrons may be accelerated at HERA up to an energy of 30 GeV. This is mainly determined by the power of the radio frequency (RF) acceleration system which compensates the energy lost by the beam through synchrotron radiation. HERA has been instrumented with superconducting RF cavities supplied by a microwave klystron system of a total power of 13.2 MW. The electrons and the protons circulate at HERA in opposite directions. The beams meet at two points in the experimental halls where the ZEUS and the H1 detectors are installed. The HERA beams are bunched. Each of the rings is capable of storing 220 bunches of particles. The collisions of electron and proton bunches, the so called beam crossings, occur every 96 ns. At nominal proton and electron beam currents of $I_p = 160$ mA and $I_e = 60$ mA HERA will provide a luminosity of $L = 1.5 \cdot 10^{31}$ cm^{-2}s^{-1}. A more detailed description of the design and the performance of HERA may be found in [39, 13].

In 1993 the HERA electron beam was operated at an energy of $E_e = 26.7$ GeV. The rings were filled with 84 colliding electron and proton bunches. In addition there were 10 unpaired electron bunches and 6 unpaired proton bunches. These, the so called pilot bunches, served for the estimation of the background from the interactions of the beam particles with the residual gas in the beam pipe. The total average electron current was 7.4 mA and the total average proton current was 10.9 mA. The maximal instantaneous luminosity reached in 1993 was $1.5 \cdot 10^{30}$ cm^{-2}s^{-1} [14].

In 1994 the electron ring was filled with positrons and the beam energy was increased to $E_e = 27.5$ GeV. The HERA rings were filled with 153 colliding bunches, 15 positron and 17 proton pilot bunches. Due to higher beam currents reaching 30 mA in case of positrons and 50 mA for the protons, the highest observed luminosity was $5 \cdot 10^{30}$ cm^{-2}s^{-1} [15]. To simplify the notation the term electron will be further used as a generic name for both electrons and positrons.

The coordinate system used throughout this thesis is the so called ZEUS coordinate system defined such that its origin is at the nominal electron–proton interaction point (IP) inside the ZEUS detector. The Z-axis points in the proton beam direction, called also the

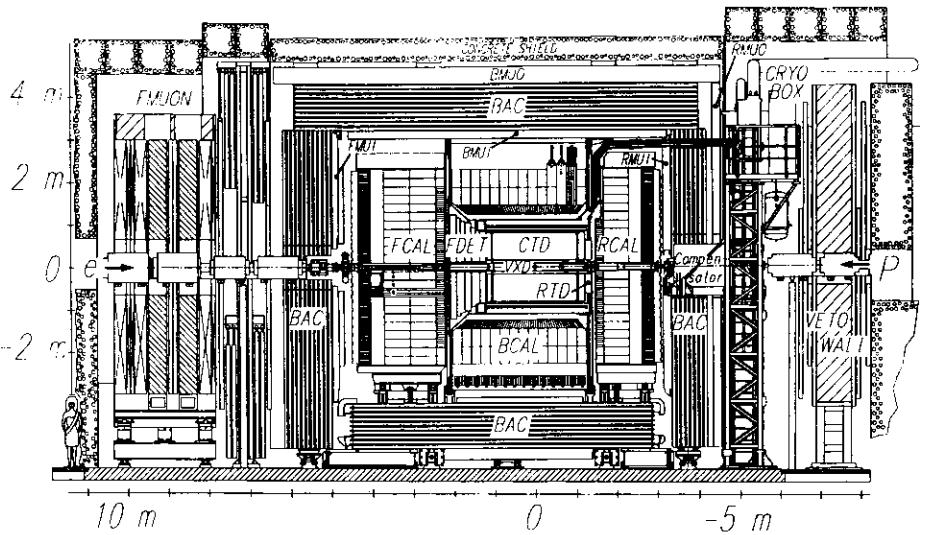

Figure 4.1: *The YZ cut of the ZEUS detector.*

forward direction. The X-axis points towards the center of the HERA ring and the Y-axis points upwards. The angular coordinates are defined accordingly: $\theta \in [0, \pi]$ denotes the polar angle with respect to the positive Z direction and $\phi \in [0, 2\pi]$ is the azimuth angle around the Z axis relative to the positive X direction.

The actual position of electron–proton interactions is randomly distributed in space, so that one talks about an extended interaction point. In the transverse direction the size of the IP is $\sigma_X \approx 1$ mm and $\sigma_Y \approx 0.1$ mm as is determined by the width of the colliding beams. In the longitudinal direction the ep vertices are distributed with $\sigma_Z \approx 12$ cm reflecting the relatively large length of the proton bunches of about 25 cm.

4.2 The ZEUS detector

The ZEUS detector is installed in the south experimental hall of the HERA ring. It is a hybrid of a number of specialized subdetectors, as shown in the cut through picture in Fig. 4.1. The ZEUS detector was designed in a way that allows for the most complete measurement of particles produced in an ep interaction. The path of charged particles emitted from the IP is measured in the inner tracking chambers comprising a vertex detector (VXD) [18], a central tracking detector (CTD) [19], and planar drift chambers in the forward (FTD) and rear (RTD) directions. The momentum is determined from the track curvature as the inner tracking detectors operate in a 1.43 T magnetic field produced by a superconducting solenoid.

Surrounding the central tracking detectors are the main uranium calorimeter (CAL) and the backing calorimeter (BAC). They capture and measure the energy carried by the particles coming from the ep interaction.

The tracks of the muons that penetrate through CAL are measured by the inner and the outer muon chambers. The path curvature of the muons passing the magnetized iron YOKE allows the determination of the momentum. In the forward direction the muons are measured in the forward muon spectrometer (FMUO).

The protons and neutrons emitted under very small angles in the forward direction are measured in the leading proton spectrometer (LPS) and forward neutron calorimeter (FNC) installed in the HERA tunnel at Z between 21 and 101 m. The region of slightly larger scattering angles is covered by the proton remnant tagger (PRT1) installed behind the forward part of CAL at $Z = 5$ m.

The electrons and photons emitted backwards under very small angles are detected in two calorimeters of the luminosity monitor (LUMI) installed in the beampipe tunnel on the rear side of the ZEUS at $Z = -35$ and -107 m.

In order to reduce the contamination of the data from interactions of the beam protons with the rest gas in the beam pipe, the so called p-gas background, the ZEUS is equiped with dedicated background detectors, in particular the C5 and the vetowall (VETO) installed behind the rear part of CAL at $Z = -3.1$ m and at $Z = -7.3$ m respectively.

In the following section a more detailed description of the detector components used in the presented analyses is given. A complete presentation of the ZEUS detector may be found in [16, 17].

4.2.1 Inner tracking devices

The ZEUS vertex detector [18] is a cylindrical drift chamber surrounding the beam pipe in the region of the nominal IP. It extends up to a radius of $r = 15.9$ cm and has a length of 159 cm. Each of its 120 radial cells consists of 12 sense wires running parallel to the beam axis. The VXD allows for a position measurement in the XY plane with a resolution of 50 μm in the central region of the cell and 150 μm near the edges.

The central tracking detector [19] surrounds immediately the VXD. It extends from an inner radius of 16.2 cm to an outer radius of 82.1 cm and has a length of 210 cm. The inner structure of the CTD consists of 72 cylindrical drift chamber layers organized in 9 superlayers. The superlayers alternate between those with wires parallel to the beam axis, the so called axial layers, and those with wires inclined at 5° angle to provide a stereo view. The stereo layers as well as the measurement of the time of the pulse arrival to both ends of the sense wire (ZbyTiming readout) allow for the Z position measurement. A spatial resolution of 260 μm in the XY plane and 2 mm along the Z direction has been achieved so far. The understanding of this detector is not easy due to the very complicated electron drift in the regions of the inhomogeneous magnetic field at the ends of the chamber. The efficiency of the chamber for detecting single hits is greater than 95%.

4.2.2 Central calorimeter

The ZEUS detector is equipped with a sampling calorimeter built as a sandwich structure of depleted uranium absorber plates and scintillator tiles [16, 50]. The light from the scintillator tiles is collected by wave length shifters and read out by photomultiplier (PM) tubes.

Mechanically, the ZEUS calorimeter is divided into three parts: forward (FCAL) covering the pseudorapidity region $1.3 > \eta > 1.1$, barrel (BCAL) covering the central region $1.1 > \eta > -0.75$ and rear (RCAL) covering the backward region $-0.75 > \eta > -3.8$ [50].

Holes of 20×20 cm^2 in the centre of FCAL and RCAL are required to accommodate the HERA beam pipe. Each of the calorimeter parts is subdivided into towers of typically 20×20 cm^2 transverse dimensions, which in turn are segmented longitudinally into electromagnetic (EMC) and hadronic (HAC) sections. To improve the spatial resolution, the electromagnetic sections are subdivided transversely into cells of typically 5×20cm^2 (10×20cm^2 for the RCAL). Each cell is read out by two photomultiplier tubes, providing redundancy and a position measurement within the cell.

Under test beam conditions, an energy resolution of $\sigma_E/E = 0.18/\sqrt{E(\text{GeV})}$ for electrons and $\sigma_E/E = 0.35/\sqrt{E(\text{GeV})}$ for hadrons was measured. The very good resolution for hadronic showers is due to the compensation property of the ZEUS calorimeter meaning equal response of the detector to electromagnetic and hadronic cascades. The compensation was achieved by carefully selecting the thickness of the scintillator and the uranium layers in the sandwich structure.

In addition to the energy measurement, the cells of the ZEUS calorimeter allow for the time measurement with a resolution below 1 ns for energy deposits greater than 1.5 GeV, a property used in background rejection. The calorimeter noise, dominated by uranium radioactivity, is in the range $15 - 19$ MeV for EMC cells and $21 - 30$ MeV for HAC cells.

4.2.3 Luminosity monitor

The ZEUS luminosity monitor (LUMI) [51, 52] detects photons and electrons from the Bethe Heitler reaction $ep \to ep\gamma$ used to measure the luminosity. It consists of a photon calorimeter (LUMIG) and an electron calorimeter (LUMIE). Both are sampling calorimeters with transverse dimensions 25×25 cm^2 made as a sandwich of lead absorber and scintillator tiles. The scintillating light is collected by wave length shifter plates and read out by photomultipliers. The energy resolution of both calorimeters is $\sigma_E/E = 0.18/\sqrt{E(\text{GeV})}$ [52].

The photon calorimeter is positioned at $Z = -107$ m and measures the photons produced at the nominal IP with angles below 0.5 mrad with respect to the electron beam direction.

The electron calorimeter is positioned at $Z = -35$ m and accepts electrons produced in the nominal IP with the energy between 7 and 20 GeV at angles up to about 5 mrad with respect to the electron beam direction.

4.2.4 Proton remnant tagger

The proton remnant tagger (PRT1) [53] is a set of scintillator counters immediately surrounding the beam pipe in the forward part of the ZEUS detector at $Z = 5.1$ m. The tagger consists of two layers of scintillating material separated by a 2 mm thick lead and wrapped in lead and iron shielding foil. Each of the scintillator layers is split in two halves independently read out by two photomultiplier tubes. The geometrical layout of the PRT1 scintillator counters and the readout channel assignment is shown in Fig. 4.2. The geometrical acceptance of the PRT1 extends over the laboratory pseudorapidity range of $1.3 < \eta < 5.8$.

4.2.5 Background detectors

The vetowall (VETO) [16, 54] located at the exit of the beam pipe tunnel at $Z = -7.3$ m protects the detector from the products of the interactions of beam protons with rest gas in the vacuum pipe occurring in the HERA tunnel. It consists of an 87 cm thick iron wall

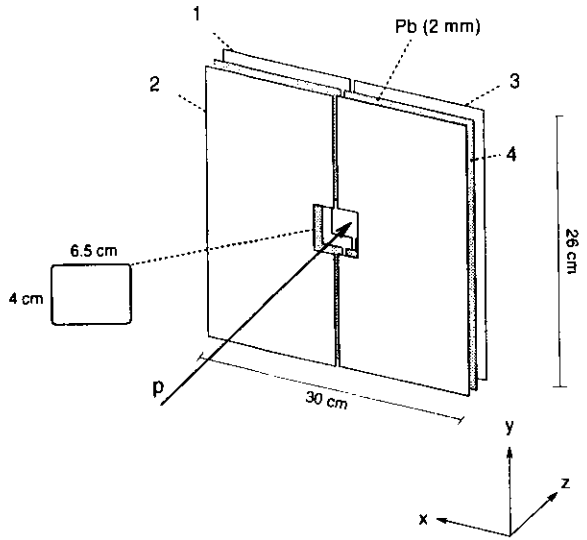

Figure 4.2: *Layout of the PRT1 scintillator counters and the readout channel assignment.*

with overall dimensions of $5 \times 6\,m^2$ acting as an absorber. The background that escaped the absorption is detected by two layers of scintillator counters installed on both sides of the iron wall and the VETO tag is issued to the trigger.

The p-gas interactions occurring closer to the IP are detected by the C5 detector [16]. It consists of two pairs of small scintillator counters (roughly $10 \times 5 cm^2$ of active area) installed above and below the beam pipe behind the RCAL at $Z = -3.1$ m.

The VETO and C5 detectors discriminate between the particles coming from a genuine ep collision at nominal IP and the upstream p-gas background by precise evaluation of the time of the hit relative to the bunch crossing time. The early timing is a clear indication of the p-gas background.

4.2.6 Trigger and data acquisition system

In order to cope with a very high rate of ep bunch crossings at HERA (10 MHz) the ZEUS detector is equipped with a very sophisticated data acquisition (DAQ) system with three levels of triggering. The principles of the operation have been described in [55] and are presented here verbally, for completeness: "The ZEUS detector comprises several independently operating detector components, each of which is equipped with their own so-called component subsystem. Component subsystems contain the front-end electronics required for the component control and readout. They interface to two levels of global trigger processors and the Eventbuilder. The layout of the ZEUS trigger and data acquisition system and the data throughput at its components are shown in Fig. 4.3.

Once a detector component has been read out, the data are stored in a 5 μs first level trigger pipeline and analyzed by a local first level trigger processor. The results of the differ-

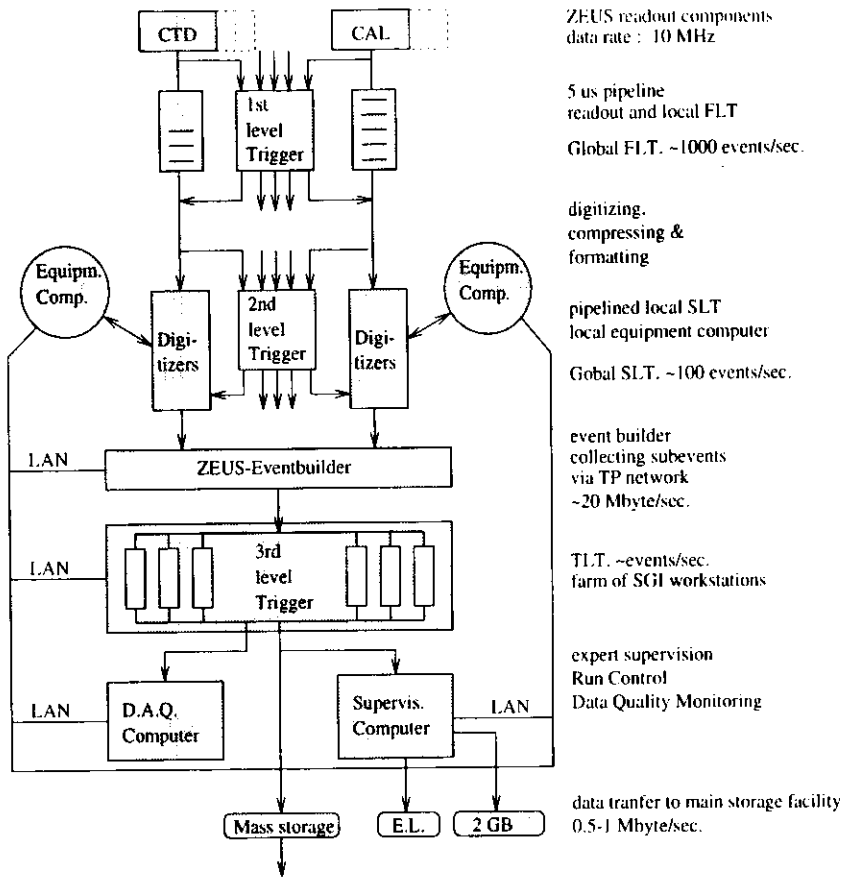

Figure 4.3: Diagram of the ZEUS data acquisition system.

ent component subsystems referring to the same beam crossing are input to the global first level trigger (GFLT), which computes an overall first level trigger decision. The maximum rate of GFLT accept decisions is designed to be 1 kHz. Up to the GFLT both the trigger and readout are deadtime free.

On GFLT accept, data accepted for further analysis are copied to a second level trigger pipeline. A GFLT accept rate of 1 kHz and a copy time of 30 μs result in 3% deadtime. This is the only source of deadtime provided no buffer full states occur.

A second level trigger processor local to the component subsystem computes a trigger subdecision, which is forwarded to the global second level trigger (GSLT) and used to compute an overall second level trigger decision. The GSLT is designed to accept approximately 10% of all GFLT accepted triggers.

In case a component subsystem receives a positive GSLT decision, the corresponding data

are assigned a GSLT decision number and transferred to the Eventbuilder. The Eventbuilder combines and formats all the component data carrying the same GSLT decision number into one data set. This data set is called an event, and its GSLT decision number is also referred to as the event number.

Once an event is complete, it is input to the third level trigger (TLT). The TLT is a processor farm consisting of six branches of a total of 36 processor nodes. It performs the global event reconstruction and a final filtering and is designed to accept up to 5 events/s.

4.2.7 Offline processing and analysis facilities

The ZEUS experiment is producing up to 1 MB of physics data during each second of its operation. This data is stored on cassettes operated by an AMPEX tape robot with a total storage capacity of 6 TB. The events are then processed offline using the ZEUS reconstruction program ZEPHYR executed on a SGI Challenge XL multiprocessor machine. The reconstruction program analyses the signals registered by the data acquisition systems of different detector components and converts them into quantities useful for the physics analysis. The amount of data necessary to describe each event in terms of physics quantities is on average 26 kB. The data in this form is stored on a farm of 600 GB of fast hard disks connected to a SGI Challenge DM machine acting as an I/O server. Therefore the data is easily accessible from the analysis programs running on two SGI Challenge XL multiprocessor machines (31 processors total). All these computers are connected by very fast HIPPI links. This system is a central computing facility of the ZEUS experiment, the so called ZARAH [56]. In the physics analysis it acts as a batch facility executing jobs submitted from the workstations used by the physicists for the interactive work.

4.2.8 Monte Carlo simulation of the detector

In this analysis the resolution and the acceptance of the detector to the studied physics processes was determined by the means of a Monte Carlo simulation. The response of the ZEUS detector was simulated using the MOZART program based on the GEANT 3.13 MC package [57]. It tracks all the particles emitted from the ep vertex through the detector apparatus simulating the processes associated with the passage of particles through matter. The detector response is expressed in the form very similar to that of the data coming from the actual detector. The data is then subject to the ZGANA program simulating the answer of the ZEUS triggering system. The MC events are then reconstructed using the ZEPHYR program just like the data from the actual experiment. The detector simulation in MOZART is very CPU consuming (simulation of one event may take up to 5 minutes on a DEC 5000/200 workstation). To produce enough MC events for the numerous analyses of the ZEUS data MOZART is executed in background on a large number of workstations in the physics institutes participating in the experiment. The distributed processing of MC events is controlled by the FUNNEL [56] system centrally managed from DESY. The MC events after the detector and trigger simulation are reconstructed and stored on the tapes in the STK silos directly accessible from the analysis programs running on ZARAH.

Chapter 5

Event selection and background elimination

During normal operation the ZEUS detector collects events corresponding to a wide spectrum of ep physics. The tagged photoproduction events are only a small fraction of the total data sample. These events are selected by a set of dedicated cuts implemented in the three levels of the ZEUS trigger system. These online selection cuts are described in the first of the following sections. The second section describes the offline processing, the method of calorimeter noise suppression, the trigger inefficiency correction and the statistical background subtraction procedure.

5.1 Photoproduction trigger

The data used in this analysis was collected using the tagged photoproduction trigger requiring the coincidence of signals in the main calorimeter and the LUMI electron tagger. The trigger configuration in 1993 and 1994 was very similar, except that in 1994 a prescaling was introduced to the photoproduction trigger and some of the selection cuts applied in 1993 in the offline were moved to the online. The online prescaling of the photoproduction events turned out to be necessary since at large instantaneous luminosities in 1994 the rate of photoproduction events was too high. In the following, the more complicated 1994 setup of the trigger is presented. The description of the 1993 configuration may be found in [58]. A schematic diagram of the trigger logic implemented in 1994 is presented in Fig. 5.1.

5.1.1 First level trigger

All the tagged photoproduction data come from one FLT slot (slot nr 36) requiring the coincidence of the LUMIE subtrigger with the REMC or REMC'th subtriggers. The LUMIE subtrigger was activated if the energy deposited in the LUMI electron calorimeter exceeded 5 GeV. The REMC subtrigger required that the energy deposited in any of the towers of the RCAL EMC section, excluding the towers immediately adjacent to the beam pipe, to be more than 161 MeV. In the REMC'th subtrigger the energy from all the RCAL EMC towers (including the beam pipe region) of at least 161 MeV was summed and compared to the threshold of 1250 MeV. Additionally, to reduce the contamination from p gas background already at the first triggering level, the events with a background hit in the C5 counter were

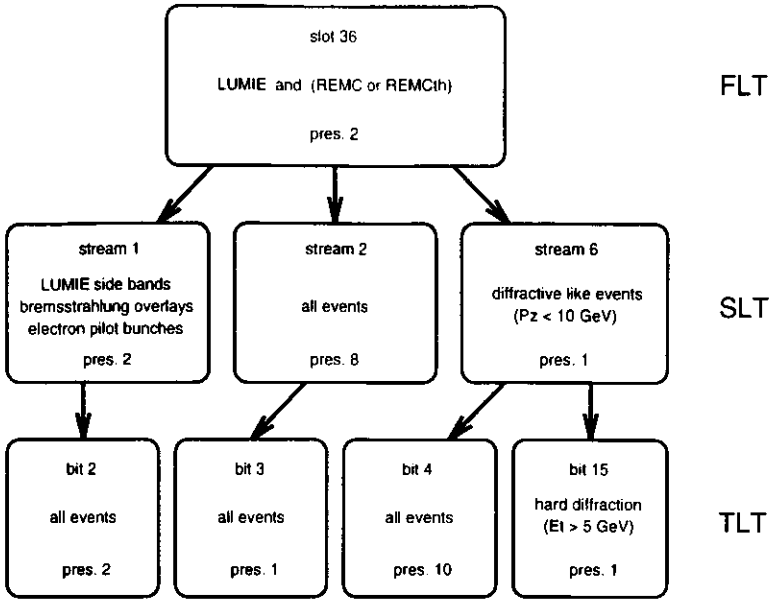

Figure 5.1: *Schematic diagram of the tagged photoproduction trigger implemented in 1994.*

rejected. To decrease the rate of tagged photoproduction subtrigger, only every second event was accepted by the FLT (prescale 2).

In the analysis of the 1993 data the events accepted by the BEMC subtrigger in coincidence with LUMIE were also included. The BEMC subtrigger required that the energy sum in the EMC section of BCAL exceeded 3100 MeV. The sum was calculated using towers with more than 164 MeV deposited energy.

5.1.2 Second level trigger

At the SLT the tagged photoproduction event stream was further cleaned from background and some parts of the event sample were additionally prescaled. The following cleaning filters were applied:

- **RCAL timing** the substantial part of the p gas background is identified by too early timing of the energy deposition in the RCAL, t_{RCAL}. It was removed by rejecting events with $|t_{RCAL}| > 8$ns, where the timing calibration is such that particles from ep collision at nominal IP result in average $\langle t_{RCAL} \rangle = 0$. If the energy allowed, also the FCAL timing was examined and compared to t_{RCAL};

- **up–down timing** the events where the difference in the timing of the hits in the upper and the lower half of the BCAL exceeds 10 ns were rejected. Such events are mostly due to cosmic muons;

- **spark** the events triggered by one cell in the calorimeter were removed if only one of the photomultipliers corresponding to that cell was activated. Such events are typically due to a spark in the PM tube.

- **$E - P_Z$** the events where the difference between the total energy, E, and the longitudinal momentum calculated from the calorimeter cells, $P_Z = \sum E \cos\theta_i$, was greater than 75 GeV. This usually indicates the contamination from p gas background.

The events coming from the tagged photoproduction FLT slot were further processed by physics filters and assigned to one of the streams shown in Fig. 5.1. The stream 2 accepted all the tagged photoproduction but was prescaled by factor 8. Particularly interesting events (LUMI electron energy outside the highly populated central band of $10 < E_{e'} < 19$ GeV, overlays with bremsstrahlung and electron pilot events) were assigned to stream 1 and saved with smaller prescale of 2. The diffractive candidates characterized by a small energy deposit in the forward part of CAL were passed with no prescale in stream 6.

5.1.3 Third level trigger

In the ZEUS third level trigger a simplified version of the ZEPHYR reconstruction program was executed. Therefore it allowed to further suppress the background contamination using more refined cuts (like muon finder algorithms to reject events due to cosmic or beam gas muons) and to apply more complicated filtering to select only the desired type of events. The filters applied on the tagged photoproduction events assigned them to the four trigger bits shown on the diagram in Fig. 5.1. The different prescale factors assigned to those bits were adjusted to optimize the usage of the tape storage the events were sent to.

5.2 Offline processing

All of the tagged photoproduction events accepted by the TLT were recorded on tapes. Later, they were reconstructed and stored on the disks in the miniDST format. These events will be also referred to as the offline sample. In the offline analysis the effects of prescaling on the three triggering levels were corrected for by assigning appropriate weights to the events.

The 1993 offline data sample corresponded to a luminosity of 0.1 pb^{-1} and consisted of 231k events. After compensating the prescaling effects it represented 385k events that fulfilled the LUMIE and CAL coincidence condition before the FLT. For the second analysis only part of the data collected by ZEUS in 1994 was used, namely after the commissioning of the PRT1. The data sample consisted of 103k events corresponding to the luminosity of 0.7 pb^{-1}. They are equivalent to 691k events after the prescaling correction. In the further text the size of the event samples will always be expressed in number of events the sample corresponds to after the prescaling correction.

In the first step of the offline analysis all the tagged photoproduction events were subject to a trigger correction and statistical subtraction of remaining background.

5.2.1 Calorimeter noise suppression and offline trigger correction

The offline data sample contained a small fraction of tagged photoproduction events that did not actually fulfill the CAL trigger condition. They were accidentally accepted by the online trigger because a PM spark or some calorimeter noise contributed to the energy sum

sufficiently to exceed the trigger threshold. This changes the efficiency of the trigger for events with energy close to the threshold in a way that is only partially described by the MC simulation. The detector MC reproduces the effects of uranium activity noise in CAL, but the PM sparks and the run to run dependent noisy readout channels are not simulated. Thus, in the offline analysis each of the events was subject to a two step trigger correction procedure.

In the first step a special noise suppression algorithm was applied on the CAL data. All the EMC(HAC) cells with energy below 60 MeV(110 MeV) were removed. For isolated cells the thresholds were increased to 80 MeV(110 MeV). Isolated cells were also removed if they corresponded to one of the noisy readout channels or if the imbalance between the two corresponding PM tubes was too large, indicating a spark. This noise suppression algorithm was verified using empty events collected with a random trigger. The remaining calorimeter activity was fully consistent with the uranium noise simulated in the detector MC.

In the second step the corrected CAL energies were used to reevaluate the trigger decision. This was done with the help of the ZGANA program used also for the trigger simulation in the MC events. The photoproduction events that failed the offline reconstructed trigger were not used in the analysis. For consistency an identical procedure was also applied on all the MC events.

Another potential source of the systematic error associated with the trigger is an inaccurate calibration of CAL FLT, which may lead to a reduced efficiency for triggering events with energy close to the threshold. This was verified by increasing the trigger thresholds applied in the offline on the data and the MC events from 161 MeV(1250 MeV) for the REMC(REMCth) subtrigger to 660 MeV(1875 MeV). The whole analysis was repeated for the increased trigger thresholds and the results were compared to those obtained using the nominal thresholds. The difference in the result was used as an estimate of the systematic uncertainty due to trigger inefficiency.

5.2.2 Statistical background subtraction

The tagged photoproduction data coming from the experiment was relatively clean from background. It was due to the trigger requirement of the coincidence of the signals in CAL and LUMIE which was difficult to fulfill by background interactions due to the large distance separating the two detectors. The remaining contamination of the offline sample was of two types: the e gas and the coincidence background. Each of them is described below together with the method used to subtract it statistically [28, 10, 58].

e–gas background

The e gas background is created when a beam electron undergoes a photoproduction reaction on a rest gas atom in the vacuum pipe. Such events satisfy the tagged photoproduction trigger if the scattered electron hits the LUMI electron calorimeter and the products of the photoproduction interaction deposit enough energy in the CAL. The e gas contamination is in total below 0.5%. However, such background events usually do not deposit any energy in the FCAL due to a large backward boost of the e gas c.m. system. Therefore these event often imitate a rapidity gap signature making the e gas background particularly dangerous in the studies of diffractive photoproduction. In some regions of the reconstructed invariant mass of a diffractively dissociated photon the concentration of the background may even reach 10% of the events.

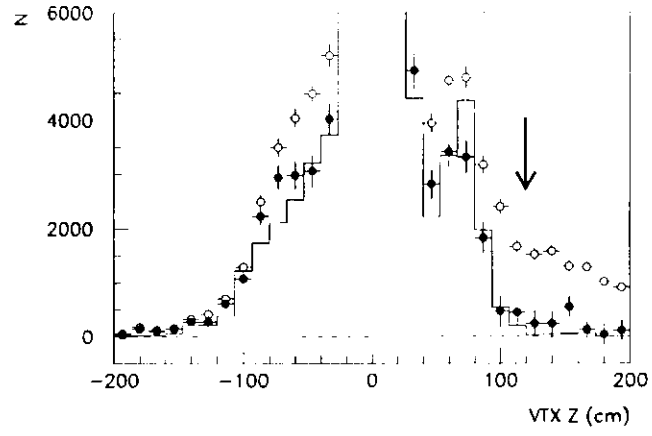

Figure 5.2: *The Z position of vertex in the events with no energy in the FCAL before (circles) and after statistical e gas background subtraction (points). The solid line is the expected vertex distribution from MC simulation of genuine ep collisions.*

Fortunately, all the remaining e gas background can be statistically subtracted using events corresponding to beam crossings where the proton bunch was empty. To compensate for the effect of the e gas collisions in other crossings the electron pilot bunch events are counted with negative weights:

$$w_{epil} = -\frac{I_{col}}{I_{pil}}, \tag{5.1}$$

where I_{col} and I_{pil} denote the total electron current in colliding and pilot bunches respectively. Figure 5.2 demonstrates the effect of statistical subtraction of the e gas background on the distribution of the Z position of the event vertex (vertex reconstruction is described in section 8.1). Majority of the ep collisions occur around $Z = 0$. The peak at $Z = -70$ cm is due to interactions with protons ariving one oscillation of the HERA RF system earlier than the actual proton buches. The beam gas background is produced uniformly in Z and has a particularly high trigger acceptance for forward shifted vertices, $Z > 100$ cm, where the genuine ep collisions almost never occur. The figure shows the vertex distribution in a particularly contaminated subsample of events with no energy in the FCAL before and after statistical e gas background subtraction. The excess of data events with vertices $Z > 100$cm vanishes after the background subtraction and the resulting vertex distribution is consistent with the one expected from the MC simulation.

Coincidence background

Many types of background processes, including p gas, cosmic muons and untagged ep collisions can satisfy the CAL subtrigger but do not produce any activity in LUMI electron calorimeter. These events can only be accepted by the tagged photoproduction trigger if they coincide with a process producing activity in LUMIE. The most common of such processes is the electron bremsstrahlung on a beam proton or an atom of a rest gas, $eN \to e\gamma N$.

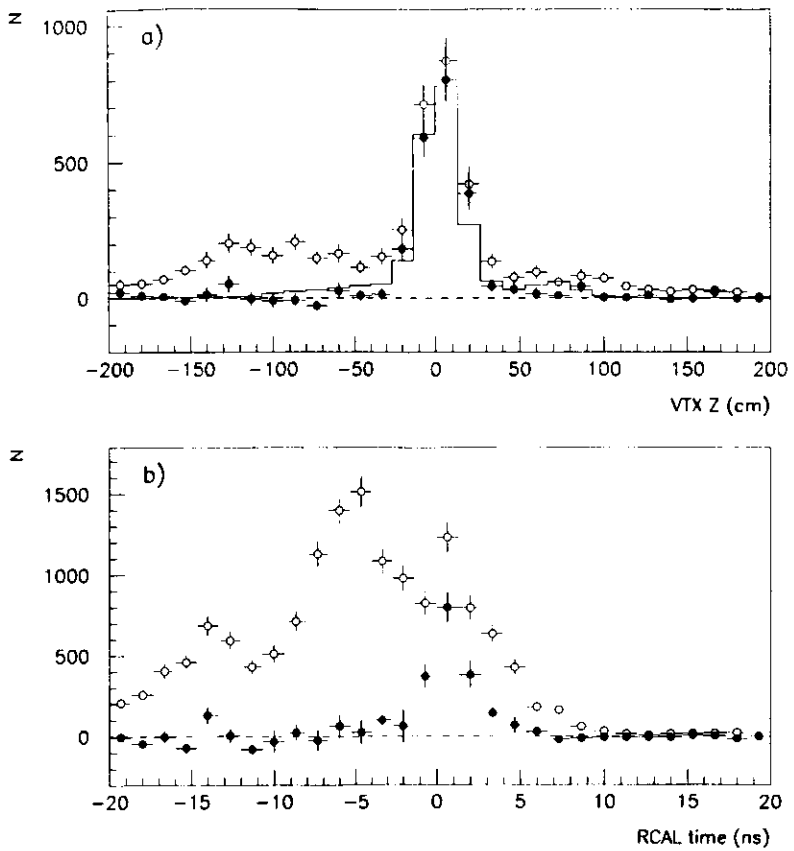

Figure 5.3: *The distributions of the vertex Z position (a) and the RCAL timing (b) for the events with VETO tag before statistical background subtraction (circles) and after background subtraction (solid points). The vertex position distribution is also compared to the shape expected for the genuine ep events from the MC (solid histogram).*

A large fraction of coincidence background events due to p gas and cosmic muons are rejected already at the FLT due to the C5 veto or at the SLT due to incorrect CAL timing. The rare coincidence events due to untagged ep interaction are not removed by any of those cuts because they have all the features of genuine tagged photoproduction collisions. Therefore, a small fraction of the coincidence background survives all the selection cuts and appears in the final data sample. The overall contamination is on the level of $1-2\%$.

In about a half of the coincidence background events the photon from the bremsstrahlung process reaches the LUMI photon calorimeter. Such events are easy to identify since the energies measured in the LUMI electron and the photon calorimeters approximately add

up to the electron beam energy, $E_{e'} + E_{\gamma} \approx E_e$. In the statistical background subtraction procedure such events are used to correct for the coincidence background events that could not be identified since the bremsstrahlung photon missed the LUMI photon calorimeter. This is usually the case for bremsstrahlung interactions occurring far from the nominal IP. The identified background events are therefore counted with negative weights

$$w_{ev} = -\frac{P_{unident}}{P_{ident}}, \tag{5.2}$$

where P_{ident} denotes the probability that the bremsstrahlung photon is detected in LUMIG and $P_{unident} = 1 - P_{ident}$. These probabilities are calculated on run to run basis from the bremsstrahlung spectra collected by the LUMI data acquisition system independent of the ZEUS triggers.

The quality of the coincidence background subtraction procedure was verified using the events tagged by the vetowall detector which indicates the presence of the p gas interaction in an event. From 3248 VETO tagged events in the 1994 offline photoproduction sample only 639 survived the background subtraction procedure. However, as shown in Fig. 5.3 the remaining events have vertex and the RCAL timing distributions characteristic for genuine ep collisions. These events should not be subtracted because they actually are genuine photoproduction interactions that happened to coincide with a random activity of the vetowall, e.g. due to remains of a beam gas collision in the HERA tunnel that were detected by the VETO but never reached the main ZEUS detector. All the VETO tagged events with the timing and the Z vertex position indicative of a p gas background are subtracted out.

Chapter 6

Simulation of photoproduction processes

In this analysis the resolution and the acceptance of the experimental apparatus were derived by means of the Monte Carlo (MC) simulation. The response of the ZEUS detector to high energy particles emitted from the ep collisions was simulated using the MOZART program described in section 4.2.8. The trigger simulation was performed with the ZGANA program. However, the response of the apparatus strongly depends on the number, the type and the momenta of the particles produced in the primary ep interaction. Therefore, the detector simulation program was supplied with a series of primary ep interactions resembling the actual collisions as closely as possible. These primary vertices were calculated using various MC generator programs. Each of the photoproduction subprocesses was simulated separately and the obtained event sample was compared to the data. Only the MC event samples providing a good description of the data were used in the final analysis. The simulation programs used to produce those final MC samples are listed in tables 6.1 and 6.2. The details of the MC generation are described below.

6.1 Diffractive processes

The diffractive photon dissociation process ($\gamma p \to Xp$) was simulated with the NZ MC program based on the Nikolaev Zakharov QCD model [59]. Within the implemented algorithm the photon dissociated system is constructed from a quark antiquark pair approximately aligned with the collision axis. The subsequent QCD radiation and the hadronization processes are simulated according to the Lund scheme [60] using the JETSET [61] package.

subprocess	primary MC	alternative MC
$\gamma p \to Xp$	NZ, PYTHIA (low M_X)	PYTHIA, POMPYT (high E_T)
$\gamma p \to Vp$	PYTHIA	
$\gamma p \to VX$	PYTHIA	
$\gamma p \to XX$	PYTHIA	
soft, non diffractive	HERWIG (min. bias)	PYTHIA (soft)
hard, non diffractive	HERWIG ($p_{T\,min} = 2.5$ GeV)	PYTHIA ($p_{T\,min} = 5$ GeV)

Table 6.1: *The MC simulation programs used in the analysis of the inclusive p_T spectrum.*

subprocess	primary MC	alternative MC
$\gamma p \to Xp$	NZ, EPSOFT (low M_X)	EPSOFT
$\gamma p \to Vp$	EPSOFT	
$\gamma p \to VX$	EPSOFT	
$\gamma p \to XX$	EPSOFT	
soft, non diffractive	EPSOFT	PYTHIA (mult. int.)
hard, non diffractive	HERWIG ($p_{T\,min} = 3.5$ GeV)	PYTHIA (mult. int.)

Table 6.2: *The MC simulation programs used in the analysis of the diffractive M_X spectrum.*

For the simulation of the region $M_X < 1.7$ GeV the PYTHIA [61] and the EPSOFT (see section 6.4) programs were used in case of the p_T analysis and in case of the M_X study respectively. To cross check the sensitivity of the measurement results to the model used for the simulation of the photon dissociation process, the analysis was repeated using an alternative MC model. In the inclusive p_T study this alternative simulation was performed using the soft diffractive option in PYTHIA. To correctly reproduce the tail of the transverse energy distribution in the data, the sample of events from PYTHIA was enriched with the harder component simulated using the POMPYT [62] program. POMPYT is a program developed within the framework of PYTHIA modeling the diffractive dissociation as partonic collisions of a direct photon with a hard, gluonic pomeron emitted from the proton. In case of the M_X analysis the alternative simulation of the diffractive photon dissociation was performed using EPSOFT. In all the MC samples used for the final analyses the distribution of the mass of the dissociation photon, M_X, followed the triple pomeron relation expressed in Eq. 2.15 with $\alpha_P \approx 1.08$. The effective exponential slope of the t spectrum was between 5 and 6 GeV^{-2}.

The other diffractive subprocesses, $\gamma p \to Vp, VX, XX$ were simulated using either PYTHIA (p_T analysis) or EPSOFT (M_X analysis). Both programs rely on parametrizations of the experimental data. The vector mesons, $V = \rho^0, \omega, \phi$, were produced with ratios similar to what was measured in low energy photoproduction experiments. The elastic slope of the t spectrum was between 10 and 12.5 GeV^{-2}. In case of the diffractive proton dissociation no precise simulation of the low mass resonances was performed and only the average M_X behaviour was reproduced.

6.2 Soft non–diffractive process

In the inclusive p_T analysis the soft, non-diffractive γp collisions were simulated with the HERWIG [63] program using the hadron hadron minimum bias option. This generation mode was developed for pp and $p\bar{p}$ physics and relies on the parametrizations of hadronic data. The hadronization in HERWIG is simulated according to the cluster model. As a result of the γp collision a number of clusters are created with momenta distributed approximately uniformly in the longitudinal phase space. The clusters are intermediate hadronization objects that undergo fragmentation until their mass is reduced to the level where the clusters can be converted into hadrons. The parameters of this generation mode in HERWIG were retuned to improve the agreement of the model with preliminary photoproduction data from ZEUS, e.g. the multiplicity of charged particles in the simulated events was reduced by about 15%.

In the M_X analysis the EPSOFT program was used to simulate the soft, non-diffractive γp collisions (see section 6.4). The hadronic final state is simulated in EPSOFT according to a similar algorithm to that in HERWIG, but the step involving the creation of intermediate hadronization clusters was eliminated. The program was also tuned to the ZEUS data and provides a slightly better description of the observed distributions than HERWIG.

For the evaluation of the model dependence the alternative MC simulation of the non diffractive photoproduction collisions was performed using the PYTHIA program. In the p_T analysis the soft, hadronic option of the generator was used which simulates low p_T hadron hadron scattering similar to that described above. In the M_X study the simulation was performed using the multiple interaction option [61, 61]. It involves an approximate QCD calculation of a process where many independent parton parton scatterings may occur in one photon hadron collision. If none of the partonic interactions involves a high momentum transfer no hard jets are produced and the resulting collisions have properties characteristic for soft interactions. However, if a large transverse momentum is exchanged, the resulting events display pronounced jet structures as expected for hard scattering. The advantage of this approach is that it naturally combines the soft and the hard regimes. The hadronization in PYTHIA is simulated according to the Lund scheme implemented in JETSET [61].

6.3 Hard processes

In the analysis of the inclusive p_T spectrum the resolved and the direct photoproduction subprocesses were simulated using the HERWIG program with the lower cut-off on the transverse momentum of the final state partons, $p_{T\,min}$, chosen to be 2.5 GeV. For the parton densities of the colliding particles, the GRV LO [65] (for the photon) and MRSD'_ [66] (for the proton) parametrizations were used. As a cross check the hard γp scattering events were also generated using PYTHIA with $p_{T\,min} = 5$ GeV.

In the M_X analysis the primary simulation was performed using HERWIG with $p_{T\,min} = 3.5$ GeV and the same parton distribution functions as above. No alternative simulation of hard photoproduction was needed since the multiple interaction mode of PYTHIA used to generate the soft non diffractive events describes also the hard regime.

6.4 EPSOFT

The EPSOFT program performs a Monte Carlo simulation of ep scattering via photon exchange. The program was primarily written to model the photoproduction processes and relies on the phenomenological models used to describe the interactions of real photons. EPSOFT can simulate the soft diffractive and non diffractive collisions of the exchanged photon with the proton. The photon is assumed to interact via its hadronic structure described by the VDM. The cross sections are calculated form the parametrizations of the hadronic and the photoproduction data and the hadronic final states are generated uniformly in the limited p_T phase space. The EPSOFT program may be also used to simulate the Deep Inelastic Scattering characterized by high virtuality of the exchanged photon, $Q^2 >> 1$ GeV^2. The dynamics of the simulated photon proton scattering is assumed not to depend on the photon virtuality in any way.

The EPSOFT program was developed within the framework of HERWIG and was tuned to reproduce the properties of the photoproduction collisions observed with the ZEUS detector. The program was used extensively in the analysis of the diffractive M_X spectrum described in this thesis. From the point of view of this study EPSOFT has two major advantages over the general purpose MC programs like HERWIG or PYTHIA. It provides a better description of the HERA data and the user has a full control over all the steps of the event generation.

The next sections describe in detail the algorithm of generating an event in the EPSOFT program.

6.4.1 Electron vertex

The event generation starts from choosing the y and Q^2 variables determining the kinematics of the electron vertex in the ep collision. The following slightly simplified version of the cross section formula from Eq. 3.3 is used:

$$\frac{d^2\sigma^{ep}}{dydQ^2} \quad \frac{\alpha}{2\pi}\frac{1}{Q^2}\left\{\frac{(1+(1 \quad y)^2)}{y}\sigma_{T\,ALLM}^{\gamma p} + \frac{2(1-y)}{y}\sigma_{L\,ALLM}^{\gamma p}\right\} \tag{6.1}$$

The cross sections for scattering of transverse and longitudinal photons on protons, $\sigma_{T\,ALLM}^{\gamma p}$ and $\sigma_{L\,ALLM}^{\gamma p}$, are calculated from the ALLM parametrization [31]. It relies on a Regge type of relation similar to Eq. 2.11 with pomeron and reggeon intercepts that may depend on Q^2. It was fitted to a large number of photoproduction and DIS data points and provides a smooth transition between the two kinematical regions.

The actual weights assigned to the generated events correspond to the total cross section (Eq. 6.1) scaled down by the factor depending on the type of the subprocess. The soft non diffractive process is assumed to correspond to 50% of the total cross section. In the photoproduction regime all the diffractive processes simulated by EPSOFT add up to about 10% of the total cross section. This leaves some space also for the hard type of interactions that have to be simulated with other MC programs.

Once the cross section is evaluated and the electron vertex is generated, the collision of the emitted photon with the proton is simulated following one of the algorithms described below.

6.4.2 Soft non diffractive collisions

The soft non diffractive collisions of hadronic photons with the proton are generated in EPSOFT according to the following algorithm:

1. The number of charged particles in the final state is chosen. Due to charge conservation, it is generated in terms of a number of pairs of charged particles, n. The negative binomial distribution (NBD) is used:

$$P_n = \left(\begin{array}{c} n+k-1 \\ n \end{array}\right)\frac{(\langle n\rangle/k)^n}{(1+\langle n\rangle/k)^{n+k}}, \tag{6.2}$$

where the width parameter, $1/k = 0.021$, was adjusted so as to obtain the best description of the track multiplicity shapes observed in the photoproduction collisions at ZEUS. The mean multiplicity of charged particle pairs is calculated from the relation

$$\langle n\rangle = 0.23 \cdot (ln\, M)^2 + 0.13 \cdot ln\, M + 0.86, \tag{6.3}$$

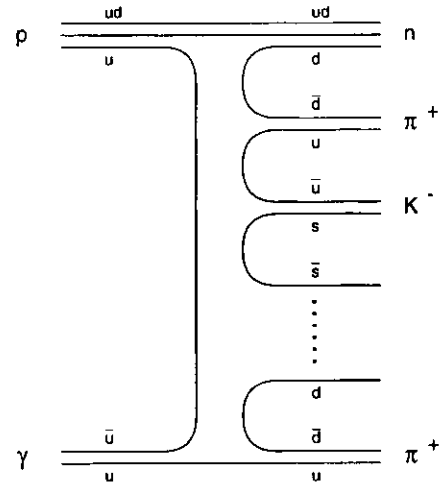

Figure 6.1: *Valence quark flavour connections between the colliding particles and the hadrons produced in a γp scattering, as implemented in the EPSOFT MC program.*

where $M = W - m_1 - m_2$ is the c.m. energy reduced by the rest mass of the two colliding particles. This relation was obtained from a fit to the pp and $p\bar{p}$ data and was later scaled by a constant factor to describe the multiplicities observed at ZEUS.

2. The particle contents of the hadronic final state is chosen. In order to automatically conserve charge, isospin and strangeness the flavors of the valence quarks of final state hadrons are generated according to the scheme depicted in Fig. 6.1. In this algorithm, adding a new hadron involves extending the quark flavour chain by one element. The new element may be either one of light quarks or a diquark line. This is selected randomly with probabilities adjusted such as to produce hadrons in ratios similar to what was measured in hadron hadron interactions [67]. When the valence quark flavors do not uniquely define the hadron, the one with the smallest mass is chosen. The procedure is repeated till the charged multiplicity $2 \cdot n$ is reached.

3. The transverse momenta of the particles chosen in the previous step are generated from the probability distribution

$$\frac{dP}{dp_T^2} \sim exp(-a \cdot \sqrt{p_T^2 + m^2}), \tag{6.1}$$

where m denotes the mass of the hadron. For strange hadrons the slope of $a = 3$ is used, and for all others it is $a = 5.1$, as indicated by fits to hadronic data [68, 75]. The transverse momenta are defined with respect to the photon proton collision axis.

4. The longitudinal momenta are generated from the flat rapidity distribution using a technique similar to that of Jadach [70]. Care is taken to assign the highest and the lowest rapidity to the hadrons that inherit the valence quark flavour of the incident particles. This operation enforces a leading particle effect. The other particles are not ordered in rapidity.

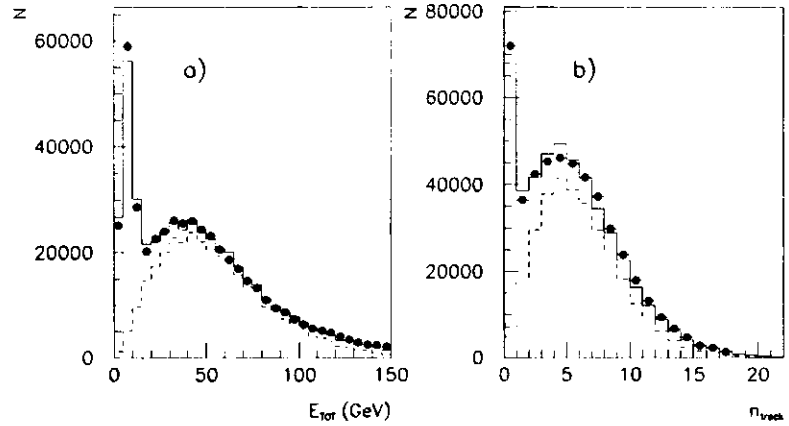

Figure 6.2: *The distribution of the total energy in the calorimeter (a) and the multiplicity of tracks detected in the region of $-1.5 < \eta < 1.5$ (b) in the tagged photoproduction events. The behaviour of the ZEUS data (points) is reproduced by the MC simulation (solid line) where the dominant soft non diffractive component was simulated using EPSOFT (dashed line).*

	$\langle n \rangle$	$\langle p_T \rangle$ (MeV)
all charged	19.0	410
$\pi^\pm$	15.5	410
γ	19.3	220
$K^\pm$	2.0	520
p	0.85	610
n	0.77	620
Λ^0	0.08	660

Table 6.3: *The average multiplicities and the mean transverse momenta of different particles in soft non diffractive photoproduction events simulated with the EPSOFT program. The collision corresponds to c.m. energy of* $W = 180$ GeV.

In steps 3 and 4 special care is taken to ensure energy and momentum conservation in the produced events. The hadronic final states of the events generated with this algorithm have all the properties characteristic for soft non diffractive hadron hadron interactions described in section 2.2.1. They also account for all the general features of the photoproduction events observed with the ZEUS detector, as illustrated with two examples in Fig.6.2. The plots show the distribution of the total energy in the calorimeter and the multiplicity of tracks detected in the region of $-1.5 < \eta < 1.5$ in the tagged photoproduction events at $\langle W \rangle = 200$ GeV. The behaviour of the data (points) is reproduced by the MC simulation (solid line) where

the dominant soft non diffractive component was simulated using EPSOFT (dashed line). Table 6.3 lists the average multiplicities and transverse momenta of different particles in non diffractive photoproduction collisions at the c.m. energy of $W = 180\,\mathrm{GeV}$ simulated with the EPSOFT program.

6.4.3 Elastic vector meson production

When the EPSOFT program is used to simulate the elastic vector meson production, $\gamma p \rightarrow Vp$, the ρ^0, ω and ϕ mesons are randomly chosen with the probabilities of 80%, 10% and 10% respectively. The mass of the ρ^0 vector meson is generated from a relativistic Breit-Wigner shape, while the ω and ϕ masses are approximated by constants. The kinematics of the γp interaction is then uniquely defined by only one variable, namely the square of the four momentum transferred by the proton, t. It is generated according to the following cross section formula:

$$\frac{d\sigma(\gamma p \rightarrow Vp)}{dt} = A \cdot \sigma^{\gamma p}_{ALLM} \cdot exp(b_{el} \cdot t), \tag{6.5}$$

where the default value of the effective slope is $b_{el} = 10\,\mathrm{GeV}^{-2}$ and may be easily redefined by the user of the EPSOFT program. The factor A, defining the weights assigned to the generated MC events, is either set to the value specified by the user or is calculated from the cross section formula in Eq. 6.6 as described in section 6.1.1. The decays of the elastically produced vector mesons:

- $\rho^0 \rightarrow \pi^+\pi^-$,
- $\omega \rightarrow \pi^+\pi^-\pi^0, \gamma\pi^0, \pi^+\pi^-$
- $\phi \rightarrow K^+K^-, K^0_L K^0_S, \rho^0\pi^0, \pi^+\pi^-\pi^0$

are simulated assuming s-channel helicity conservation [1]. By default a dominantly transversal polarization of the exchanged photons is assumed which is a good approximation only for $Q^2 \approx 0$. If EPSOFT is used in the DIS regime the relative contributions of the the transverse and longitudinal polarization states has to be specified by the user. The part of the EPSOFT program responsible for simulating the decays of vector mesons relies on the code developed by G.Levman [71].

6.4.4 Diffractive photon dissociation

At the beginning of the simulation of the diffractive interaction $\gamma p \rightarrow Xp$ in the EPSOFT program the t and the M_X variables are chosen. They are generated from the following cross section formula:

$$\frac{d^2\sigma(\gamma p \rightarrow Xp)}{dt dM^2_X} = C \cdot \sigma^{\gamma p}_{ALLM} \cdot \frac{exp(b_{sd} \cdot t)}{(M^2_X + Q^2 - m^2_1)^{\alpha_P(0)}}, \tag{6.6}$$

where the constant term $C = 0.11$ defining the ratio between the single diffractive cross section and total one was taken from a fit to the hadronic and the photoproduction data [7, 8]. The soft pomeron intercept has a default value of $\alpha_P(0) = 1.1$ and may be easily modified by the user of the EPSOFT program. The effective exponential slope is set by default to $b_{sd} = 6\,\mathrm{GeV}^{-2}$ in accord with the results of the measurements [7, 8] but may also be redefined by the user. The dissociated photon mass is generated in the range

$(m_X + 2 \cdot m_{\pi^0})^2 < M^2_X < 0.1 \cdot W^2$, where m_{π^0} is a pion mass and W denotes the c.m. energy of the γp system. The vector meson mass m_X is chosen with the same algorithm as that used for the simulation of the elastic process. This ensures the correct transition between the resonant and the non resonant region of the M_X spectrum, avoiding gaps and double-counting. In addition, EPSOFT may be used in a mode where the cross section of the elastic process defined by the factor A in Eq. 6.5 is chosen such that the finite mass sum rule [7, 8] is fulfilled. This rule states that the extrapolation of the high M_X behaviour of the single diffractive process (Eq. 6.6) into the low mass region defines the average behaviour of the resonances including the elastic scattering. This ensures a correct transition from the elastic to the non elastic M_X region also in terms of the cross sections assigned to the EPSOFT events.

Once the t and M_X variables are chosen, the proton vertex in the reaction $\gamma p \rightarrow Xp$ is calculated. In the last step the hadronic final state X is simulated using the method inspired by the experimental observations described in section 2.2.2. The data suggests that diffraction may be modelled as an exchange of an object that, in collision with the dissociating particle, leads to a final state similar to that in non diffractive hadron hadron scattering. This object will be later called a pomeron, although the relation with the pomeron trajectory introduced to explain the growth of the total cross sections is not direct (see section 2.2.3). Following this observation the hadronization of the photon dissociated system is simulated in EPSOFT using the algorithm described in section 6.1.2 and already implemented in the program for the non diffractive channel. The only difference is that instead of generating the γp collision at a c.m. energy W, a collision of the photon with the pomeron at a c.m. energy M_X is simulated.

6.4.5 Diffractive proton dissociation

The EPSOFT program can also simulate processes involving the dissociation of the proton $\gamma p \rightarrow VN, XN$. The corresponding cross section is calculated in relation to the reactions $\gamma p \rightarrow Vp, Xp$, where the proton emerges intact:

$$\frac{d^3\sigma(\gamma p \rightarrow XN)}{dt dM^2_X dM^2_N} = \frac{d^2\sigma(\gamma p \rightarrow Xp)}{dt dM^2_X} \cdot 0.5 \cdot \frac{d^2\sigma(pp \rightarrow pN)/dt\, dM^2_N}{d\sigma(pp \rightarrow pp)/dt}. \tag{6.7}$$

The first term in this formula describes the cross section for the process with the proton in the final state. The second term defines the ratio of probabilities that the proton dissociates into the nucleonic system N to that in which it emerges intact. It is derived from a parameterization of the $pp \rightarrow pp$ and $pp \rightarrow pN$ cross sections developed by G.Wolf [72] and based on the data from [7]. The hadronic cross sections $\sigma(pp \rightarrow pN, pp)$ were evaluated at the c.m. energy W. The factor 0.5 accounts for the fact that in $pp \rightarrow pN$ scattering there are two protons which can dissociate. The mass of the nucleonic system is generated in the range $(1.25\,\mathrm{GeV})^2 < M^2_N < 0.1 \cdot W^2$.

The hadronization of the nucleonic system N is simulated with the same method as that used in case of the photon dissociation (see section 6.1.1). The algorithm implemented in EPSOFT for the non diffractive channel is used to calculate the collision of the pomeron with the proton at the c.m. energy M_N. In case of the double diffractive process the hadronization of the dissociated photon and the dissociated proton are simulated independently.

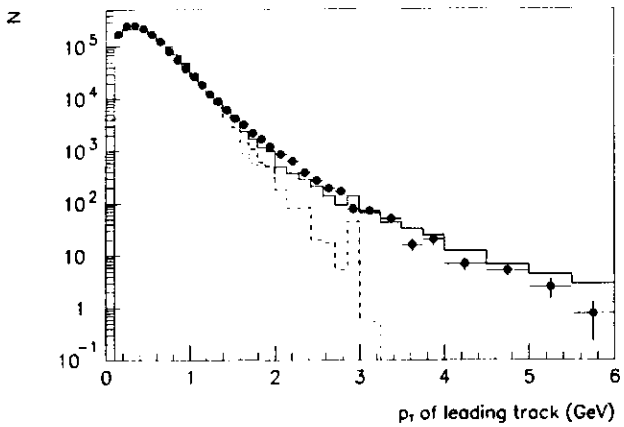

Figure 6.3: *The transverse momentum distribution of the track with the largest p_T in each event observed in the data (points) compared to the result of the MC simulation (solid histogram). The soft and the hard MC components are shown as dashed and dotted histograms respectively.*

6.5 Combining different MC subprocesses

In order to correctly describe the shapes of the photoproduction events observed at ZEUS the MC samples corresponding to the different subprocesses had to be combined in the ratios similar to that between the corresponding photoproduction cross sections. Since the models used to simulate the subprocesses give only a rough cross section estimate the relative normalization of the MC samples was inferred from the data.

In the first step the MC samples corresponding to soft and hard non diffractive components were combined in a ratio that gave the best description of the transverse momentum distribution of the track with the largest p_T in each event observed in the data. In Fig. 6.3 the leading track p_T spectrum is compared to such a combination of the MC samples. The dashed and the dotted histograms show the contribution of the soft and the hard MC components respectively. The obtained ratio between the hard and the soft MC components depends on the way the hard processes were simulated. For the case of a hard MC component generated with $p_{T\,min} = 2.5$ GeV, it corresponded to 11% of the non-diffractive sample, while for $p_{T\,min} = 5$ GeV it was only about 3%.

In the next step the non diffractive MC sample was combined with all the diffractive subprocesses. The relative contributions of the subprocesses were adjusted according to the ratios of the corresponding photoproduction cross sections measured at HERA [28, 15]. The non diffractive cross section $\sigma_{nd} = 91 \pm 11$ μb [28] combined with the total one $\sigma_{tot} = 143 \pm 17$ μb [28] measured at $\langle W \rangle = 180$ GeV were used to fix the contribution of non diffractive processes in the MC simulation at $64 \pm 8\%$. The photoproduction cross section of the elastic ρ^0 production of $\sigma(\gamma p \to \rho^0 p) = 11.7 \pm 0.4$ [15] corrected for other light vector mesons [1] and non elastic production mechanism was used to determine the contribution of the processes $\gamma p \to Vp, VN$ to be $15 \pm 3\%$. The remaining $21 \pm 8\%$ of the

photoproduction interactions were assigned to the diffractive photon dissociation processes $\gamma p \to Xp, XN$. The ratio between the number of diffractive interactions where the proton emerges intact to the interactions where the proton is dissociation to higher mass nucleonic state was inferred from the weights assigned to the simulated events by the MC generator programs.

Chapter 7

Measuring diffraction at ZEUS

The following chapter presents the experimental techniques used in this study to identify the photoproduction events corresponding to diffractive processes and to reconstruct the mass of the photon dissociated system.

7.1 Selection of diffractive events using CAL

The events corresponding to diffractive processes were selected by requiring a gap in the rapidity distribution of the final state particles. In the first of the presented analysis, the p_T spectrum measurement, the forward part of the central calorimeter was used for that purpose. All the events where the pseudorapidity of the most forward energy deposit with energy above 400 MeV, η_{max}, was below 2 were classified as diffractive like. The rapidity gap in those events extended at least to the edge of the FCAL at a pseudorapidity of 1.3. Thus, in the γp c.m. system the gap spans approximately over the pseudorapidity interval

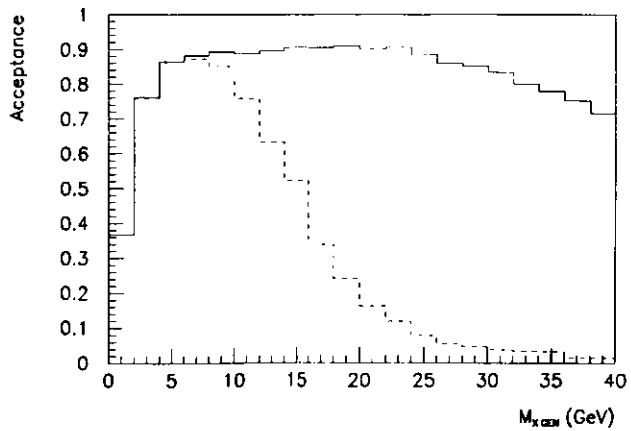

Figure 7.1: *The acceptance of the trigger and the $\eta_{max} < 2$ cut (dashed line) or the PRT1 cut (solid line) for the diffractive process $\gamma p \to Xp$ simulated with the NZ MC program vs. the mass of the dissociated state X.*

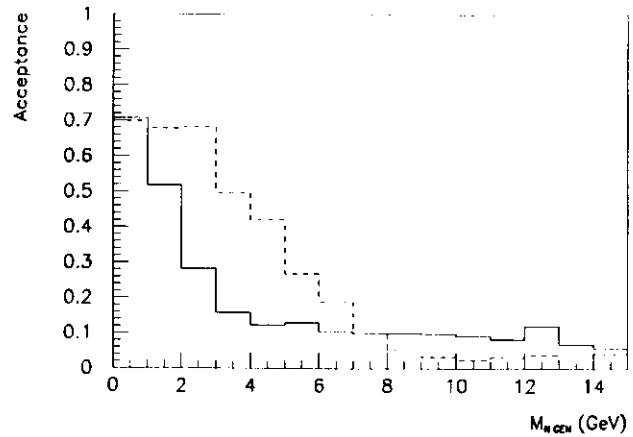

Figure 7.2: *The acceptance of the trigger and the $\eta_{max} < 2$ cut (dashed line) or the PRT1 cut (solid line) for the process process $\gamma p \to XN$ simulated with the EPSOFT MC program vs. the mass of the nucleonic system N.*

of $-0.1 < \eta_{c.m.} < 2.2$. The combined acceptance of the trigger and the $\eta_{max} < 2$ cut for the diffractive process $\gamma p \to Xp$ simulated with the NZ MC program is presented in Fig. 7.1 as a function of the mass of the dissociated photon state. In the region of $M_X < 3$ GeV, where a significant fraction of the produced particles escape through the beam pipe hole in RCAL, the acceptance is reduced due to the calorimeter trigger inefficiency. As M_X grows the acceptance reaches $80 - 90\%$. At $M_X \approx 15$ GeV the acceptance falls again since the particles from the decay of the dissociated system start reaching the rapidity gap region. In Fig. 7.2 the acceptance of the trigger and the $\eta_{max} < 2$ cut for the $\gamma p \to XN$ process simulated with the EPSOFT MC program is shown as a function of the nucleonic system mass. The acceptance is highest for very low masses. At $M_N > 1$ GeV it drastically falls since the decay products of the N system start reaching the FCAL and the events fail the rapidity gap cut.

7.2 Selection of diffractive events using PRT1

In the second study, the M_X analysis, the diffractive events were selected by requiring no charged particle hits in the proton remnant tagger. The PRT1 covers the laboratory pseudorapidity interval of $1.3 < \eta < 5.8$, which in the γp c.m. system approximately corresponds to $2.2 < \eta_{c.m.} < 3.7$. Therefore, the diffractive like events selected with the PRT1 have a rapidity gap shifted by over two pseudorapidity units into the proton fragmentation region, compared to the events selected with the $\eta_{max} < 2$ cut. This allows to study diffractive interactions with much higher values of M_X and to reduce the contribution of the proton dissociation process.

The PRT1 was operational for the first time in 1991. Therefore, a number of tests were performed to ensure that the quality of the data provided by the detector was satisfactory for this analysis. These tests are summarized below.

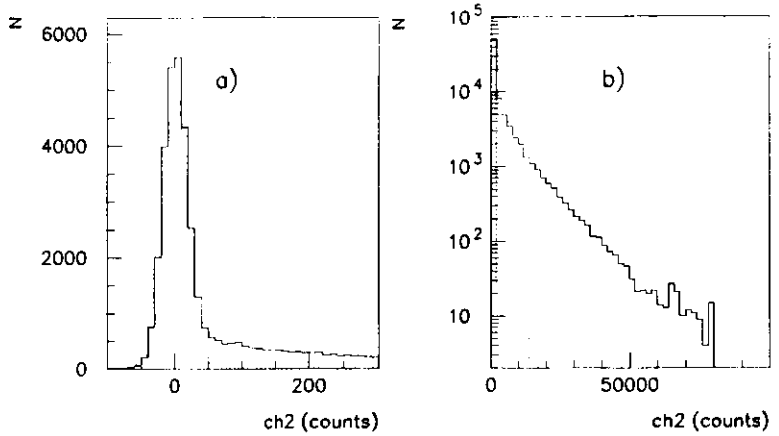

Figure 7.3: *The spectrum of the signal from channel 2 of the PRT1 in tagged photoproduction events (solid histogram) and the shape of the spectrum in empty events (dotted histogram). The distributions are shown in linear (a) and in logarithmic scales (b).*

7.2.1 PRT1 performance

As discussed in section 4.2.1 the PRT1 consists of two pairs of scintillator counters read out by PMs, installed in the front part of the ZEUS detector. The spectrum of the signal from one of the PRT1 channels (e.g. *ch*2) in tagged photoproduction events is shown in Fig. 7.3. The distribution has a peak at $ch2 \approx 0$ and a tail extending towards very high amplitudes of the PM signal expressed in counts of the readout analog to digital converter. A very similar behaviour of the spectrum at $ch2 \approx 0$ was observed for empty events collected with a random trigger indicating that the peak is due to pedestal fluctuations in events with no hits in the PRT1 counters. The corresponding spectrum is shown as a dashed histogram in Fig. 7.3. In order to better visualize the PRT1 response to charged particle hits the data sample was limited to photoproduction events with the total energy in CAL $E_{tot} > 50$ GeV. These events are dominantly due to non diffractive processes with low probability of a rapidity gap in the PRT1 region. The resulting distribution is shown in Fig. 7.4. The remaining contribution from events with no PRT1 hits was statistically subtracted using empty events collected with random trigger to parametrize the shape of the pedestal peak. The resulting spectrum, shown as a dashed histogram in Fig. 7.4, corresponds to the photoproduction events with at least one charged particle hit in this PRT1 counter. The spectrum has a maximum at $ch2 \approx 70$ counts corresponding to the deposit of one minimum ionizing particle (MIP) smeared by the large detector noise. Due to this noise there are no additional maxima from two and more MIP hits. A similar analysis showed that the MIP peak in channels 3 and 4 is located approximately at $ch3 \approx 90$ and $ch4 \approx 80$ counts. The first maximum in the signal spectrum of channel 4 was at $ch4 \approx 30$ counts. This is consistent with the known fact that the high voltage (HV) supplying the corresponding PM was accidentally set at a too low value resulting in the gain reduction. Figure 7.5 presents the correlation between the signals from *ch*3 and *ch*4 in photoproduction events with $E_{tot} > 50$ GeV. These readout channels correspond to two scintillator counters covering the same area. Apart from the

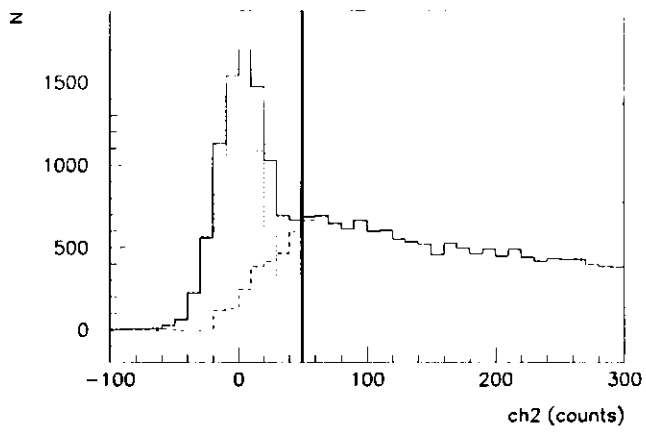

Figure 7.4: *The spectrum of the signal from channel 2 of the PRT1 in tagged photoproduction events with the total energy in CAL $E_{tot} > 50$ GeV (solid histogram) and the shape of the spectrum in empty events (dotted histogram). The difference between the two spectra corresponds to the photoproduction events with at least one charged particle hit in this part of the PRT1 (dashed histogram).*

large peak from events with no hits in this part of the PRT1 a second maximum at $ch3 \approx 90$ and $ch4 \approx 80$ counts due to a single charged particle crossing both layers is observed.

In this analysis the threshold of 50 counts is used to discriminate between the signal and the pedestal fluctuations in each of the PRT1 counters. This threshold is marked as a solid line in Fig. 7.4 and 7.5. The poor separation between the pedestal peak and the signal introduces effectively some accidental tags – the noise, and the tagging inefficiency. The noise was estimated using empty events collected with random trigger and corresponding to the beam crossings where the electron and proton bunches were empty. There, the fraction of events with the PRT1 signal exceeding the 50 counts threshold was measured to be $0.6 \pm 0.2\%$. This number is similar for all four channels. The same fraction calculated using events collected with random trigger but corresponding to crossings where both electron and proton bunches were filled is $1.4 \pm 0.3\%$. This number accounts for the detector noise as well as the beam related background.

The efficiency of each of the PRT1 counters was calculated as a fraction of the events with charged particle hits where the signal from the counter exceeds the threshold of 50 counts. The PRT1 spectrum for events with charged particle hits was obtained by statistically subtracting the pedestal peak due to events with no hits from the measured distribution, a procedure analogous to that illustrated in Fig. 7.4. However, the calculation was performed for exactly the type of events that are responsible for the non diffractive contamination in the M_X spectrum measurement, namely those with invariant mass reconstructed from the CAL $M_{X\,rec} < 32$ GeV (see section 7.3). The tagging efficiency obtained for the channels 2, 3 and 4 is $97.8 \pm 0.5\%$. The efficiency of channel 4 suffering from too low setting of the HV was $90.5 \pm 0.5\%$, which is also satisfactory for this analysis.

The above estimations of the PRT1 efficiency were verified using an alternative method

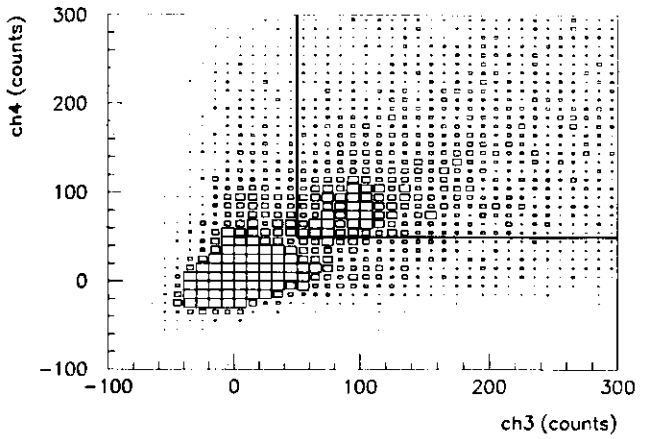

Figure 7.5: *Distribution of the signals from two PRT1 counters covering the same area in tagged photoproduction events with $E_{tot} > 50$ GeV.*

that involved studying the response of the counters from one layer in sample of events with charged particle hits in PRT1 selected using the counters from the other layer. The results were consistent with those of the method presented above.

In this analysis the events were classified as non rapidity gap if at least one counter from each of the two PRT1 layers produced a signal of more than 50 counts. This tagging method will be hereafter called the coincidence method since it requires the detection of the charged particle in both PRT1 layers. The overall tagging efficiency derived from the single counter efficiencies is $92 \pm 0.7\%$. The rate of accidental tags due to the detector noise and the beam background was estimated using random trigger events to be $1.1 \pm 0.2\%$.

To cross check the sensitivity of the final results to the PRT1 noise and inefficiency, the entire analysis was repeated using an alternative tagging method where no coincidence between the two PRT1 layers was required. All events where the signal from any of the four counters exceeded 50 counts were classified as non rapidity gap. This selection method is characterized by an overall tagging efficiency of $96 \pm 0.5\%$. The noise and the background result in the PRT1 tag in $2.3 \pm 0.2\%$ of events.

The difference in the final result obtained using the two tagging methods was used as an estimate of the systematic error due to the inefficiency and the noise of the PRT1.

7.2.2 Simulation of PRT1 acceptance

PRT1 is covering the region of very small polar angles in the forward direction. In the non diffractive events this region is populated with particles having relatively large energy due to the forward boost of the hadronic c.m. system. A full MC simulation of the hadronic and the electromagnetic cascades in this region requires a lot of computing. To simplify these calculations a special technique of shower termination is used in the ZEUS detector simulation program, namely only more energetic particles in the cascade are traced and the energy deposited in the detector material by low energy particles is calculated from

the parametrization of the test beam data [73]. This significantly speeds up the computing but may introduce some inaccuracies into the simulation of the detectors sensitive to low energy particles like PRT1. The shower termination may result in an underestimation of the probability that PRT1 tags an event because of the low energy particles from a cascade developing in the neighbourhood of the detector. This effect was studied using a set of MC events simulated once with and once without the shower termination. The comparison showed that for events with $M_{X,e} < 32$ GeV the shower termination reduces the number of events with hits in PRT1 by about 9%. This artificial inefficiency in the MC simulation with the shower termination is of a similar size as the overall inefficiency of the detector measured in the data. For this reason no additional apparatus related inefficiencies were introduced into the MC simulation if the shower termination technique was used. To account for the background and the detector noise 1% of randomly chosen MC events with no charged particle hits in PRT1 were treated as if there was a hit. To verify the precision of the detector simulation the simulated fraction of the events tagged by PRT1 was compared to the data. To eliminate the sensitivity to the model assumptions about the diffractive processes the comparison was performed for the events with $E_{tot} > 50$ GeV dominated by non diffractive collisions. The following fractions were obtained:

- $95.6 \pm 0.1\%$ MC simulation with non diffractive γp interactions generated using EPSOFT (soft) and HERWIG (hard).
- $94.8 \pm 0.1\%$ MC simulation with non diffractive γp interactions generated using PYTHIA.
- $91.9 \pm 0.1\%$ data.
- $97.0 \pm 0.1\%$ data, if the alternative tagging method requiring no coincidence between the two PRT1 layers is used.

The discrepancy between the data and the two MC simulations is much smaller than the difference between the two methods of tagging the data used for the estimation of the systematic uncertainty of the final result. This comparison demonstrates that although only a very simplified MC simulation of the PRT1 was performed the achieved precision is sufficient for this analysis.

7.2.3 PRT1 acceptance for diffractive events

The acceptance of the rapidity gap cut based on the PRT1 for the diffractive process $\gamma p \to Xp$ simulated with the NZ MC is presented in Fig. 7.1 as a function of the mass of the dissociated state X. Above the region of low M_X affected by the trigger inefficiencies the acceptance is close to 90% and it is approximately flat in M_X. At $M_X \approx 30$ GeV the acceptance starts to fall due to particles from the decay of the dissociated system X that reach the PRT1. The acceptance of the PRT1 cut for the $\gamma p \to XN$ process simulated with the EPSOFT MC program is shown in Fig. 7.2. The cut removes most of the events with $M_X > 2$ GeV.

7.3 Diffractive mass reconstruction

In tagged photoproduction at HERA the diffractively dissociated photon state is usually produced with only a small laboratory momentum, due to the large Lorenz boost of the γp

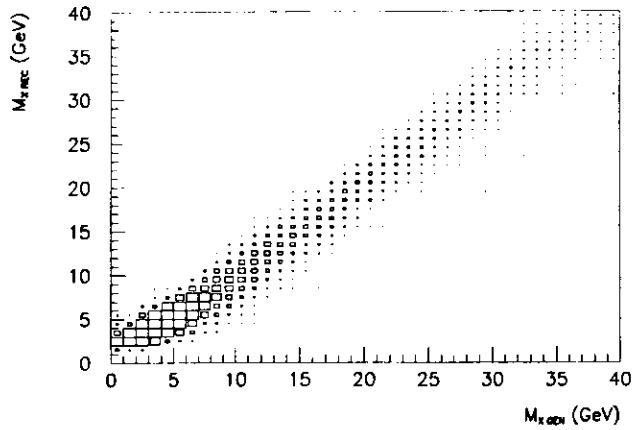

Figure 7.6: *The relation between the generated and the reconstructed mass of the dissociated photon state in events simulated with the NZ MC program.*

c.m. system in the proton direction. At $W \approx 200$ GeV the system X is produced at rest if $M_X \approx 20$ GeV. Therefore, the mass of the diffractively dissociated system may be estimated from the invariant mass of the hadronic system observed in the central ZEUS calorimeter without large loses due to beam pipe holes. The following relation was used to estimate the M_X:

$$M_X = \sqrt{E^2 - P^2} \approx \sqrt{(E - P_Z)\cdot(E + P_Z)} = \sqrt{2E_e\cdot(E + P_Z)} \qquad (7.1)$$

The total momentum of the dissociated photon system, P, is approximated with the longitudinal one, P_Z, since in tagged photoproduction the transverse momentum of the system X is usually very small (roughly $\langle P_t \rangle \approx 200$ MeV). The mass of the dissociated photon was reconstructed from the following expression:

$$M_{X\,rec} = A\cdot\sqrt{2(E_e - E_{e'})\cdot(\sum_{cond} E_i + \sum_{cond} E_i cos\theta_i)} + B. \qquad (7.2)$$

The energy of the scattered electron, $E_{e'}$, was measured in the LUMI electron calorimeter. The E_i and θ_i denote the energy and the polar angle of CAL condensates defined as groups of adjacent cells with the total energy of at least 100 MeV, if all the cells belong to the EMC, or 200 MeV otherwise. The condensate finding algorithm was run after the noise suppression procedure described in section 5.2.1. In the p_T spectrum analysis the $M_{X\,rec}$ was calculated by summing over all the condensates of at least 160 MeV. In the M_X study the threshold was increased to 200 MeV to reduce the sensitivity to low energy particles which suffer from large energy losses in the inactive material before entering the CAL. Both analyses were repeated without these additional energy thresholds and the difference in the obtained results was used for the estimation of the systematic accuracy.

The correction factors A and B compensate the effects of energy loss in the inactive material, beam pipe holes, and calorimeter cells that failed the energy threshold cuts. Their values were selected such as to give the best estimation of the true invariant mass in diffractive photon dissociation events obtained from the MC simulation. If M_X was reconstructed using

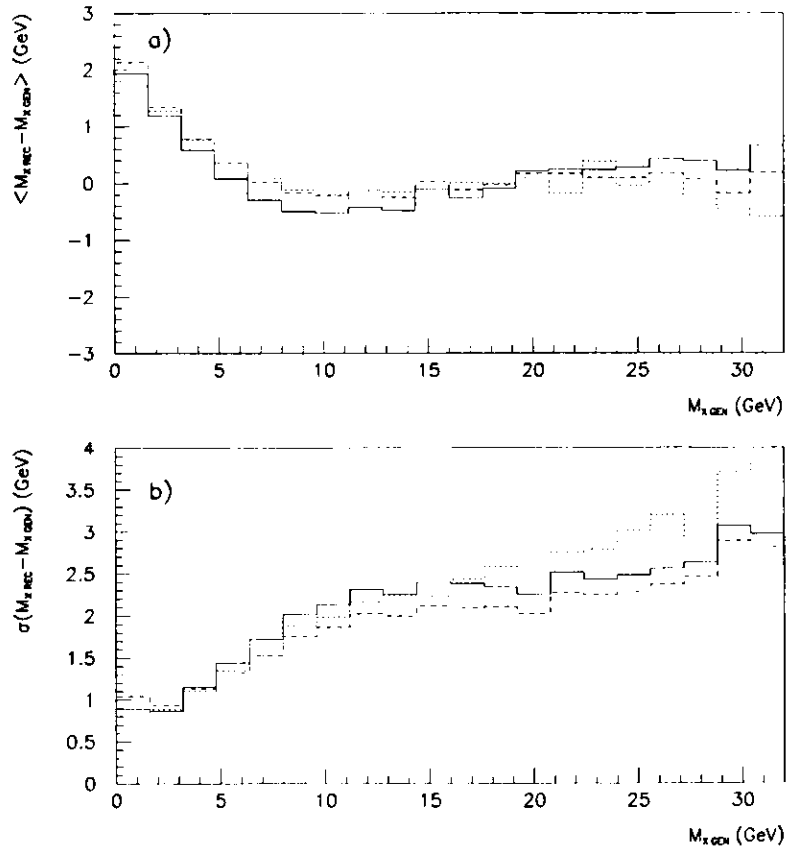

Figure 7.7: *(a) The mean difference between the reconstructed and the generated mass of the dissociated photon in the events simulated with the NZ MC program. The $M_{X\,rec}$ calculated from condensates with energy above 200 MeV (solid line) is compared to that obtained with all the condensates (dashed line). The dotted line corresponds to the events simulated with the EPSOFT MC program. (b) The resolution of the mass reconstruction. The lines have the same meaning as in (a).*

the condensates above the energy of 160 MeV the correction factors had the values of $A = 1.20$ and $B = 1.0$ GeV. For the method with the additional threshold of 200 MeV the factors were $A = 1.17$ and $B = 1.1$ GeV. If no additional energy threshold was applied the factors were $A = 1.13$ and $B = 1.3$ GeV.

Figures 7.6 and 7.7 show the quality of the diffractive mass reconstruction. In the events corresponding to the process $\gamma p \to Xp$ simulated using the NZ and the EPSOFT MC programs the reconstructed $M_{X\,rec}$ is compared to the generated value of the dissociated photon

mass, $M_{X\ p\pi}$. In the region of $M_{X\ p\pi} < 1$ GeV the diffractive mass is reconstructed with the resolution close to 1 GeV. Unfortunately, due to a large fraction of particles escaping the detection through the beam pipe hole in RCAL, the reconstruction of low diffractive masses suffers from migrations towards higher $M_{X\ p\pi}$ values. In the range $1 < M_{X\ p\pi} < 28$ GeV the resolution of the mass reconstruction is close to 2 GeV and the linearity is better than 0.5 GeV. All of the measurements presented in this thesis are limited to this region of M_X.

Chapter 8

Transverse momentum spectrum of charged particles

In this chapter the details of the measurement of the inclusive p_T spectrum of charged particles in diffractive and non diffractive photoproduction are described. The trigger used to collect the events and the general offline selection criteria have already been discussed in chapter 5. The further analysis relies on the information about charged particle tracks reconstructed from the tracking chamber data using the algorithm described in the following section. The actual measurement was performed with the data passing the final selection cuts described in sections 8.2 and 8.3. The acceptance correction procedure and the possible systematic effects are discussed in sections 8.4 and 8.5. The results are presented in section 8.6.

8.1 Track reconstruction

At the beginning of the track reconstruction algorithm the pulses measured in the sense wires of the CTD and VXD are analyzed and the precise position of all the hits is calculated from the drift time information. The hits are combined into full tracks in the pattern recognition algorithm starting with the hits in the outermost axial superlayers of the CTD. As the trajectory is followed inwards towards the beam axis, more hits from the axial wires of the CTD and the VXD are incorporated. The resulting path in the XY projection is used for the pattern recognition in the ZbyTiming and the stereo superlayers. The track candidates are then fitted to a 5 parameter helix model. To account for the possible multiple Coulomb scattering in the inactive material between the VXD and the CTD the tracks are allowed to have a kink in this region. In the calculation of the covariance matrix the possibility of multiple scattering in the beam pipe walls and any dead material traversed by the track is taken into account. For the full length tracks with $p_T > 1$ GeV the resolution in transverse momentum is $\sigma_{p_T}/p_T \approx 0.005 \cdot p_T \oplus 0.016$ (p_T in GeV).

The reconstructed tracks are used to determine the primary event vertex by means of the perigee fitting technique [71]. The trajectories of the tracks assigned to the primary vertex are then reevaluated with an additional constraint from the vertex position. In events with charged particle tracks, the position resolution of the reconstructed primary vertex is 0.6 cm in the Z direction and 0.1 cm in the XY plane.

In 1993 the ZEUS CTD and VXD were fully operational for the first time and not all of the detector effects were fully understood. Also the MC simulation of the tracking detectors

was not yet final and some of the subtle effect were not reproduced, e.g. complicated electron drift in the regions of inhomogeneous magnetic field at the ends of the chambers. The MC simulation is used in this study to correct the data for the limited detector acceptance and if not all of the effects are appropriately simulated the accuracy of the correction might be reduced. To verify the size of this potential inaccuracy, the analysis was repeated with an alternative sample of MC events where the performance of the tracking system was artificially degraded. This sample was obtained using a tracking reconstruction code where two modifications were introduced. Since in the data only about 38% of the tracks were reconstructed including the information from the VXD compared to over 90% in the MC simulation, in the alternative reconstruction code the VXD was not used at all. In addition 10% of the hits in the CTD were randomly removed to reduce the average number of hits used to reconstruct a charged track in the MC simulation to the level observed in the data. The superlayer closest to the beam pipe was excluded from this procedure.

8.2 Offline event selection

This analysis is based on the offline data sample described in chapter 5. The offline trigger correction and the statistical background subtraction were performed as discussed in sections 5.2.1 and 5.2.2. Only the events with an electron energy measured in the LUMI calorimeter in the range $15.2 < E_{e'} < 18.2$ GeV were used, limiting the γp c.m. energy to the interval of $167 < W < 191$ GeV. The longitudinal vertex position determined from tracks was required to be in the range $-35\,\mathrm{cm} < Z_{vertex} < 25\,\mathrm{cm}$. The vertex cut limited the data sample to the region of uniform detector acceptance. The cosmic ray background was suppressed by requiring the transverse momentum imbalance of the deposits in the main calorimeter, $P_{missing}$, relative to the square root of the total transverse energy, $\sqrt{E_T}$, to be small: $P_{missing}/\sqrt{E_T} < 2\sqrt{\mathrm{GeV}}$.

The data sample was divided into a diffractive and a non diffractive subsamples using the rapidity gap cut of $\eta_{max} < 2$ described in section 7.1. The final non rapidity gap data sample consisted of 119k events.

The diffractive like data sample was analyzed as a function of the dissociated photon mass reconstructed in the main calorimeter using the method described in section 7.3. The diffractive data were selected in two intervals of the reconstructed mass, namely $1 < M_{X\,rec} < 7$ GeV and $8 < M_{X\,rec} < 13$ GeV. As already mentioned in section 7.3, the reconstruction of low diffractive masses suffered from large migrations towards higher $M_{X\,rec}$. To reduce the migrations from the region corresponding to vector meson production, both of the diffractive data samples were subject to an additional cut $\eta_{max} > -2$. According to the MC simulation the events passing all the diffractive cuts and falling into the lower interval of $M_{X\,rec}$ are dominantly due to the photon dissociation process with a mean value of the diffractive mass and a spread of $\langle M_X \rangle = 5$ GeV and r.m.s. = 1.8 GeV. The diffractive events falling into the higher $M_{X\,rec}$ interval correspond to $\langle M_X \rangle = 10$ GeV with r.m.s. = 2.3 GeV. The contamination from the non diffractive processes was approximately 12% in the lower M_X interval and 25% in the higher one. The final diffractive data sample consisted of 5k and 3k events in the two M_X intervals respectively.

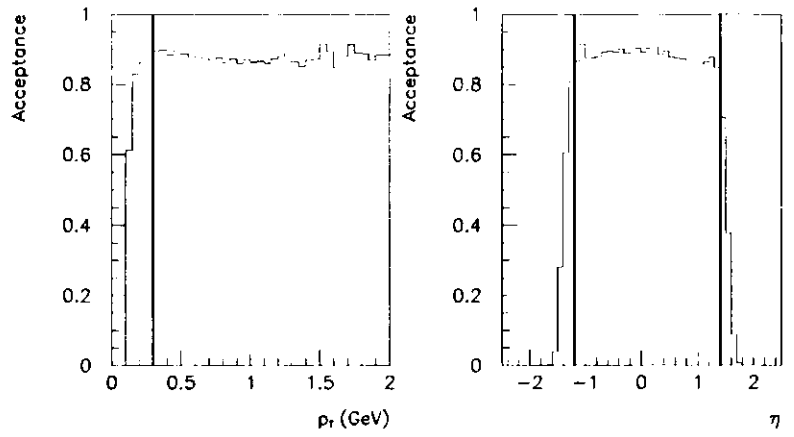

Figure 8.1: *The efficiency of the charged track reconstruction convoluted with the acceptance of the selection cuts listed in section 8.3. The acceptance as the function of p_t is shown only for particles with $-1.2 < \eta < 1.1$ and the acceptance vs. η is limited to particles of $p_t > 0.3$ GeV. The acceptance was calculated by means of the MC simulation.*

8.3 Track selection

The charged tracks used for this analysis were selected with the following criteria:

- only tracks accepted by an event vertex fit were considered. This eliminated most of the tracks that came from secondary interactions and decays of short lived particles;
- tracks must have hits in each of the first 5 superlayers of the CTD. This requirement ensures that only long, well reconstructed tracks are used for the analysis;
- $-1.2 < \eta < 1.1$ and $p_t > 0.3$ GeV.

These selection cuts were tested on events from the MC simulation. The efficiency of the charged track reconstruction convoluted with the acceptance of the selection cut is plotted as a function of p_t and η in Fig. 8.1. The last of the cuts listed above selects the region where the effective acceptance for charged particles is close to 90% and is uniform in p_t and in η. The contamination of the final sample from secondary interaction tracks, products of decays of short lived particles, and from spurious tracks (artifacts of the reconstruction algorithm) ranges from 5% at $p_t = 0.3$ GeV to 3% for $p_t > 1$ GeV. The inefficiency and remaining contamination of the final track sample is accounted for by the acceptance correction described in the following section.

The pseudorapidity distributions of tracks with $p_t > 0.3$ GeV passing the quality cuts in the non diffractive like events and the two diffractive like data samples are presented in Fig. 8.2. The distribution of tracks in non diffractive like events is compared to result of the MC simulation of the η spectrum of charged particles with $p_t > 0.3$ GeV in the non diffractive processes shown as dashed histogram in Fig. 8.2. Similarly, the two distributions of tracks in the diffractive like events are compared to the simulated η spectrum of charged

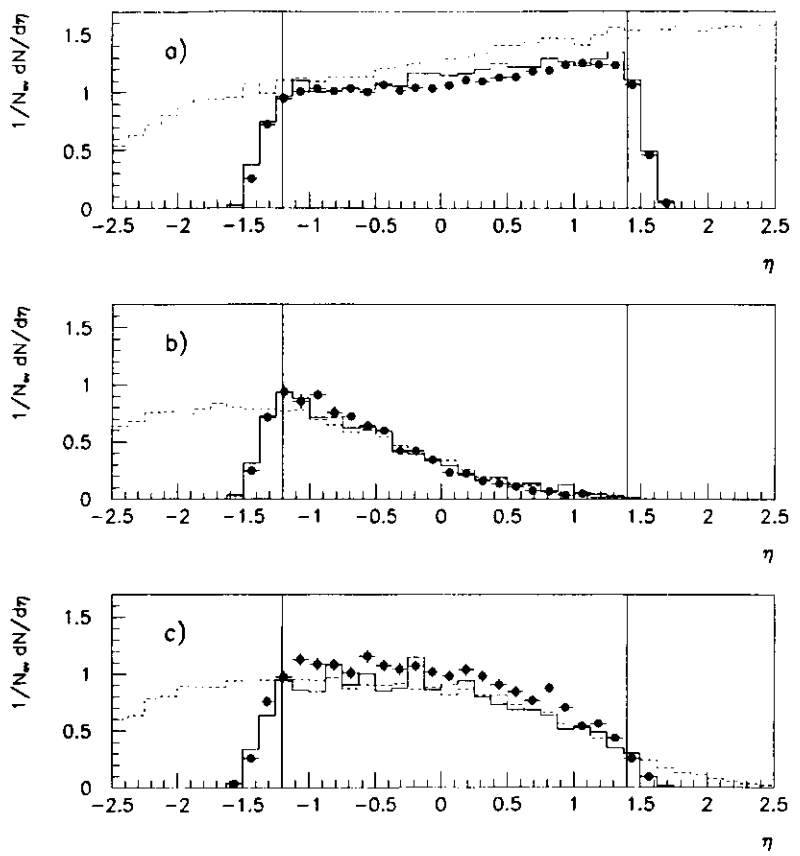

Figure 8.2: *The pseudorapidity distribution of tracks with $p_T > 0.3$ GeV passing the quality cuts in the non diffractive like events (a), diffractive like events with $4 < M_{X\,rec} < 7$ GeV (b) and $8 < M_{X\,rec} < 13$ GeV (c). The data (points) is compared to the results of the MC simulation of η spectrum of charged particles (dashed histogram) in the non diffractive processes (a) and the diffractive photon dissociation with mass $4 < M_{X\,gen} < 7$ GeV (b), and $8 < M_{X\,gen} < 13$ GeV (c). The solid histograms show the results of the MC simulation including the contribution from other photoproduction processes, the detector effects and the quality cuts applied on the reconstructed tracks. The vertical lines mark the region of $-1.2 < \eta < 1.1$ used for the measurement.*

particles in the diffractive photon dissociation with generated mass $4 < M_{X\,gen} < 7$ GeV and $8 < M_{X\,gen} < 13$ GeV, respectively. In the region of good detector acceptance the distributions of tracks and charged particles are very similar. The solid histograms in Fig. 8.2 show the results of the MC simulation including the contribution from other photoproduction processes, the detector effects and the quality cuts applied on the reconstructed tracks. The

simulated distributions closely follow those in the data. Only the region of $-1.2 < \eta < 1.1$ is used for the measurement.

The transverse momenta of the tracks measured in the data and simulated in the MC displayed no correlation with η over the considered interval and were symmetric with respect to the charge assigned to the track.

8.4 Acceptance correction

The acceptance corrected transverse momentum spectrum was derived from the reconstructed spectrum of charged tracks, by means of a multiplicative correction factor, calculated using Monte Carlo techniques:

$$C(p_T) = \left(\frac{1}{N_{gen\,ev}} \cdot \frac{dN_{gen}}{dp_{T\,gen}}\right) \Big/ \left(\frac{1}{N_{rec\,ev}} \cdot \frac{dN_{rec}}{dp_{T\,rec}}\right).$$

N_{gen} denotes the number of primary charged particles generated with a transverse momentum $p_{T\,gen}$ in the considered pseudorapidity interval and $N_{gen\,ev}$ is the number of generated events. Only the events corresponding to the appropriate type of process were included, e.g. for the lower invariant mass interval of the diffractive sample only the Monte Carlo events corresponding to diffractive photon dissociation with the generated invariant mass $4 < M_{X\,gen} < 7$ GeV were used. N_{rec} is the number of reconstructed tracks passing the experimental cuts with a reconstructed transverse momentum of $p_{T\,rec}$, while $N_{rec\,ev}$ denotes the number of events used. Only the events passing the trigger simulation and the experimental event selection criteria were included in the calculation. To account for the contribution of all the subprocesses, the combination of the MC samples described in section 6.5 was used. This method corrects for the following effects in the data:

- the limited trigger acceptance;
- the inefficiencies of the event selection cuts, in particular the contamination of the diffractive like spectra from non diffractive processes and the events with a dissociated mass that was incorrectly reconstructed. Also the non-diffractive like sample is corrected for the contamination from diffractive events with high dissociated mass;
- limited track finding efficiency and acceptance of the track selection cuts, as well as the limited resolution in momentum and angle;
- loss of tracks due to secondary interactions and contamination from secondary tracks;
- decays of charged pions and kaons, photon conversions and decays of lambdas and neutral kaons. Thus, in the final spectra the charged kaons appear, while the decay products of neutral kaons and lambdas do not. For all the other strange and charmed states, the decay products were included.

The p_T dependence of the factors used to correct the non diffractive and the two diffractive spectra is shown in Fig. 8.3. The validity of the acceptance correction method relies on the correct simulation of the described effects in the Monte Carlo program. The possible discrepancies between reality and Monte Carlo simulation were analyzed and the estimation of the effect on the final distributions was included in the systematic uncertainty, as described in the following section.

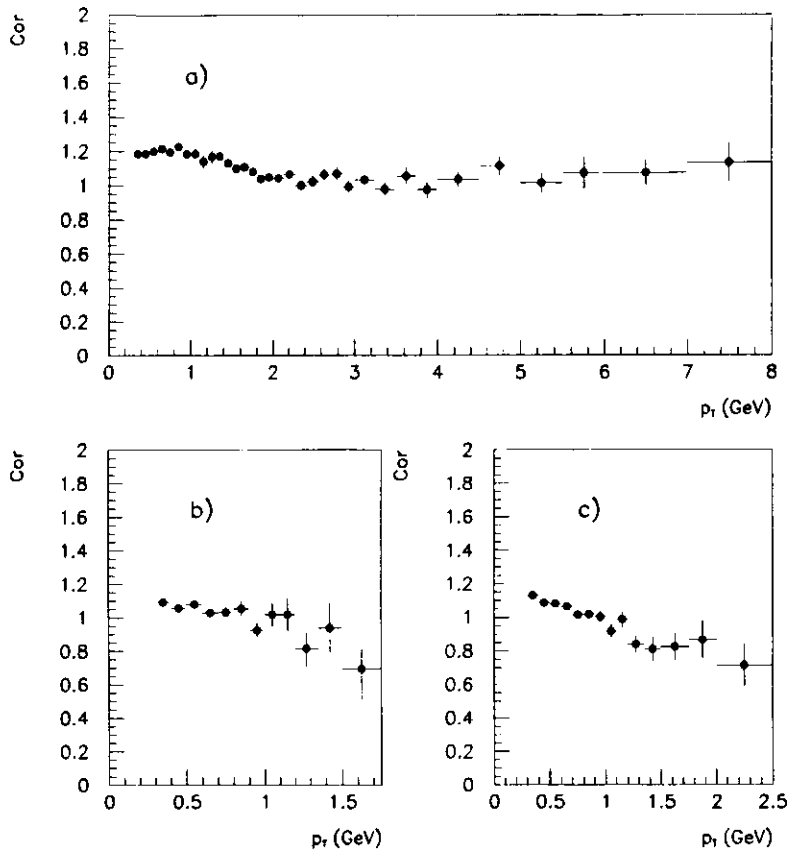

Figure 8.3: *The factors $C(p_T)$ used for the correction of the non diffractive spectrum (a), the diffractive spectrum corresponding to $\langle M_X \rangle = 5$ GeV (b), and $\langle M_X \rangle = 10$ GeV (c). The error bars indicate the statistical precision of the correction factors.*

8.5 Systematic effects

One of the potential sources of the systematic inaccuracy is the tracking system and its Monte Carlo simulation used for the acceptance correction. This inaccuracy was estimated by recalculating all the correction factors using the alternative MC simulation code with artificially degraded tracking performance. The difference in the obtained $C(p_T)$ factors with respect to the original values is plotted in Fig. 8.1 as a function of p_T. In case of the non diffractive spectrum the difference in $C(p_T)$ is estimated to be less than 10%. In case of the low M_X interval of the diffractive spectrum the corresponding estimate is 13%. The discrepancy is larger since most of the particles in those events are emitted backward at pseudorapidities close to the tracking acceptance limit. The systematic error due to track

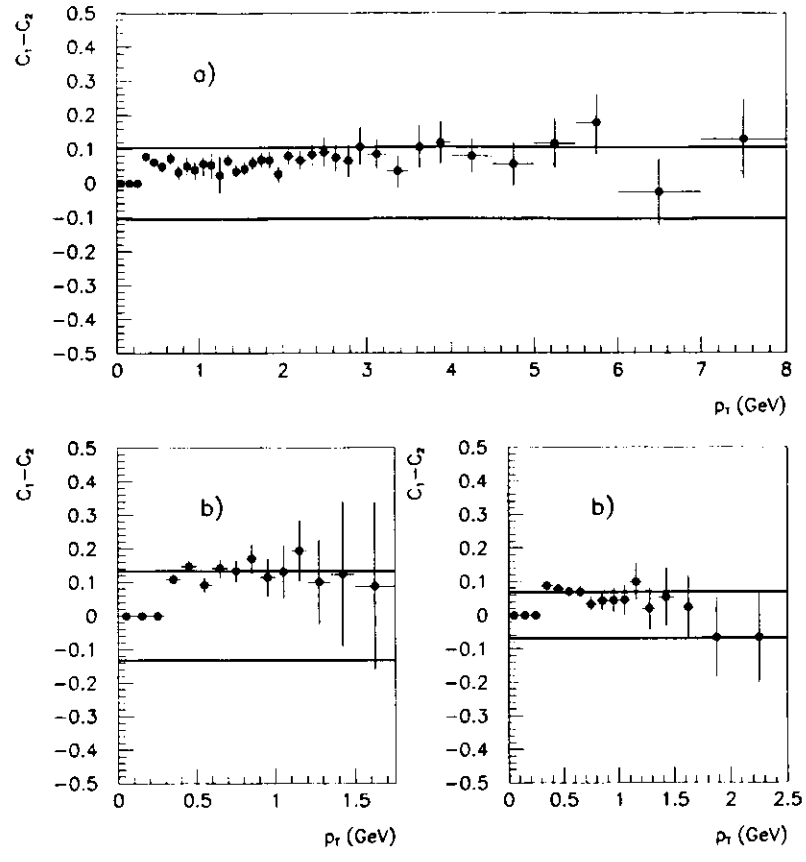

Figure 8.4: *The difference between the correction factors calculated assuming artificially degraded tracking performance and those calculated from the standard MC simulation in case of the non diffractive spectrum (a), the diffractive spectrum with $\langle M_X \rangle = 5$ GeV (b) and $\langle M_X \rangle = 10$ GeV (c). The horizontal lines indicate the corresponding error limits.*

finding efficiency in the diffractive spectrum at $\langle M_X \rangle = 10$ GeV was estimated to be 7%. An incorrect description of the momentum resolution in the MC simulation at high p_t could also introduce a systematic error in the results. To verify this, the calculation of the correction factors was repeated assuming much worse tracking resolution. The effect was negligible compared to the statistical precision of the data. It was also checked that the final spectra would not change significantly if the tracking resolution at high p_t had non gaussian tails at the level of 10% or if the measured momentum was systematically shifted from the true value by the size of the momentum resolution.

Another source of systematic uncertainty is the Monte Carlo simulation of the trigger

response. It was verified that even a very large (20%) inaccuracy of the BCAL energy threshold would not produce a statistically significant effect. By varying the trigger thresholds it was verified that the inefficiency of the RCAL trigger would change the number of events observed, but would not affect the final p_t spectrum since it is normalized to the number of events. The correlation between the RCAL energy and the p_t of tracks is very small.

To evaluate the model dependence, the calculation of the correction factors was repeated using an alternative set of MC programs (see chapter 6) and compared to the original values. The differences between the obtained factors varied between 5% for the high mass diffractive sample and 11% for the non diffractive one. The sensitivity of the result to the assumed relative cross sections of the physics processes was checked by varying the subprocess ratios within the error limits given in [28]. The effect was at most 3%.

All the above effects were combined in quadrature, resulting in an overall systematic uncertainty of the charged particle rates as follows: 15% in the non-diffractive sample, 15% in the $\langle M_X \rangle = 5$ GeV diffractive sample and 9% in the $\langle M_X \rangle = 10$ GeV diffractive sample. All these systematic errors are independent of p_t.

8.6 Results

The double differential rate of charged particle production in an event of a given type is calculated as the number of charged particles ΔN produced within $\Delta\eta$ and Δp_t in N_{ev} events as a function of p_t:

$$\frac{1}{N_{ev}} \cdot \frac{d^2N}{dp_t^2\, d\eta} = \frac{1}{N_{ev}} \cdot \frac{1}{2p_t \Delta\eta} \cdot \frac{\Delta N}{\Delta p_t}. \tag{8.1}$$

The charged particle transverse momentum spectrum was derived from the transverse momentum distribution of observed tracks normalized to the number of data events by means of the correction factor described in section 8.1. The resulting charged particle production rates in diffractive and non-diffractive events are presented in Fig. 8.5 and listed in Tables 8.1, 8.2 and 8.3. In the figure the inner error bars indicate the statistical error. Quadratically combined statistical and systematic uncertainties are shown as the outer error bars. The non diffractive spectrum extends to $p_t = 8$ GeV, while the diffractive spectra reach $p_t = 4.75$ GeV and 2.5 GeV in case of $\langle M_X \rangle = 5$ and 10 GeV respectively.

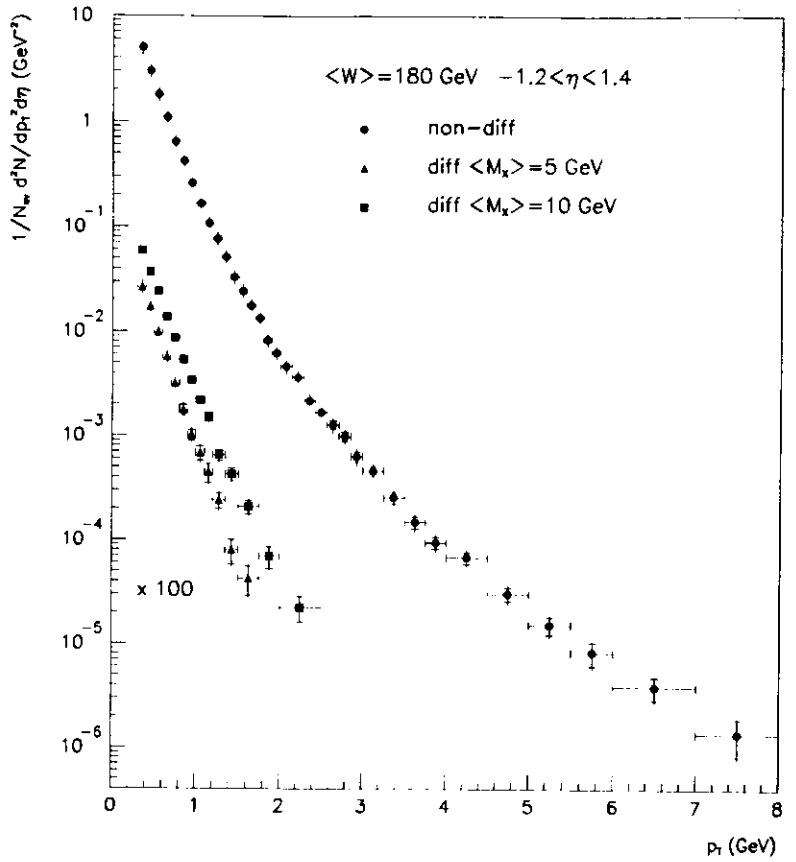

Figure 8.5: *Inclusive transverse momentum distributions of charged particles in photoproduction events at* $\langle W \rangle = 180$ GeV *averaged over the pseudorapidity interval of* $-1.2 < \eta < 1.1$. *The inner error bars indicate the statistical errors and the outer ones represent the quadratic sum of the statistical and systematic errors. For the sake of clarity the diffractive points are shifted down by two orders of magnitude.*

p_T [GeV]	$\frac{1}{N_{ev}} \cdot \frac{d^2N}{dp_T^2 d\eta}$ [GeV^{-2}]	σ_{stat} [GeV^{-2}]	σ_{syst} [GeV^{-2}]
0.30 0.40	1.98	0.05	0.71
0.40 0.50	2.99	0.03	0.44
0.50 0.60	1.78	0.02	0.26
0.60 0.70	1.09	0.01	0.16
0.70 0.80	0.611	0.012	0.096
0.80 0.90	0.420	0.010	0.063
0.90 1.00	0.259	0.007	0.038
1.00 1.10	0.161	0.005	0.021
1.10 1.20	0.107	0.001	0.016
1.20 1.30	0.0761	0.0031	0.0111
1.30 1.40	0.0513	0.0017	0.0077
1.40 1.50	0.0329	0.0012	0.0049
1.50 1.60	0.0212	0.0010	0.0036
1.60 1.70	0.0175	0.0008	0.0026
1.70 1.80	0.0133	0.0006	0.0020
1.80 1.90	0.0082	0.0005	0.0012
1.90 2.00	0.00615	0.00038	0.00092
2.00 2.11	0.00451	0.00028	0.00068
2.11 2.29	0.00360	0.00021	0.00054
2.29 2.43	0.00215	0.00017	0.00032
2.43 2.57	0.00166	0.00013	0.00025
2.57 2.71	0.00126	0.00012	0.00018
2.71 2.86	0.00098	0.00010	0.00015
2.86 3.00	0.000625	0.000071	0.000093
3.00 3.25	0.000456	0.000048	0.000068
3.25 3.50	0.000252	0.000031	0.000037
3.50 3.75	0.000147	0.000020	0.000022
3.75 4.00	0.000091	0.000012	0.000014
4.00 4.50	0.000067	0.000008	0.000010
4.50 5.00	0.0000301	0.0000015	0.0000015
5.00 5.50	0.0000151	0.0000029	0.0000023
5.50 6.00	0.0000082	0.0000021	0.0000012
6.00 7.00	0.0000038	0.0000009	0.0000006
7.00 8.00	0.0000014	0.0000005	0.0000002

Table 8.1: *The rate of charged particle production in an average non diffractive event. The data correspond to $-1.2 < \eta < 1.4$. The σ_{stat} and σ_{syst} denote the statistical and systematic errors.*

p_T [GeV]	$\frac{1}{N_{ev}} \cdot \frac{d^2N}{dp_T^2 d\eta}$ [GeV^{-2}]	σ_{stat} [GeV^{-2}]	σ_{syst} [GeV^{-2}]
0.30 0.40	1.63	0.06	0.24
0.40 0.50	1.02	0.04	0.15
0.50 0.60	0.559	0.028	0.083
0.60 0.70	0.308	0.019	0.046
0.70 0.80	0.165	0.013	0.021
0.80 0.90	0.088	0.011	0.013
0.90 1.00	0.0479	0.0059	0.0071
1.00 1.10	0.0312	0.0052	0.0046
1.10 1.20	0.0196	0.0042	0.0029
1.20 1.35	0.0100	0.0018	0.0015
1.35 1.50	0.00301	0.00087	0.00045
1.50 1.75	0.00153	0.00052	0.00023

Table 8.2: *The rate of charged particle production in an average event with a diffractively dissociated photon state of a mass $\langle M_X \rangle = 5$ GeV. The data correspond to $-1.2 < \eta < 1.4$. The σ_{stat} and σ_{syst} denote the statistical and systematic errors.*

p_T [GeV]	$\frac{1}{N_{ev}} \cdot \frac{d^2N}{dp_T^2 d\eta}$ [GeV^{-2}]	σ_{stat} [GeV^{-2}]	σ_{syst} [GeV^{-2}]
0.30 0.40	3.87	0.10	0.31
0.40 0.50	2.32	0.06	0.20
0.50 0.60	1.16	0.01	0.13
0.60 0.70	0.803	0.033	0.072
0.70 0.80	0.485	0.023	0.043
0.80 0.90	0.288	0.017	0.025
0.90 1.00	0.176	0.012	0.015
1.00 1.10	0.109	0.009	0.009
1.10 1.20	0.0732	0.0075	0.0065
1.20 1.35	0.0291	0.0035	0.0026
1.35 1.50	0.0186	0.0028	0.0016
1.50 1.75	0.0086	0.0011	0.0008
1.75 2.00	0.00260	0.00066	0.00023
2.00 2.50	0.00076	0.00023	0.00007

Table 8.3: *The rate of charged particle production in an average event with a diffractively dissociated photon state of a mass $\langle M_X \rangle = 10$ GeV. The data correspond to $-1.2 < \eta < 1.4$. The σ_{stat} and σ_{syst} denote the statistical and systematic errors.*

Chapter 9

Diffractive mass spectrum

In this chapter the details of the measurement of the dissociated photon mass spectrum in diffractive photoproduction are described. The extraction of the uncorrected M_X distribution from the data is discussed in the following section. The acceptance correction method and the procedure of reweighting the MC event samples used to correct the data are described in sections 9.2 and 9.3. In the last two sections the results are presented and the systematic uncertainties are analyzed.

9.1 Uncorrected M_X spectrum

This measurement is based on the offline data sample described in chapter 5. The offline trigger correction and the statistical background subtraction were performed as discussed in sections 5.2.1 and 5.2.2. Only the events with the electron energy measured in the LUMI calorimeter in the range $12 < E_{e'} < 18\,\mathrm{GeV}$ were used, limiting the γp c.m. energy to the interval of $176 < W < 225\,\mathrm{GeV}$. This cut reduced the data sample to 180k events. The diffractive like events were selected using the rapidity gap cut based on PRT1 and described in section 7.2. The data sample after the PRT1 cut corresponded to 131k events. In these events the invariant mass of the hadronic system measured in the central calorimeter was reconstructed with the method described in section 7.3. The obtained distribution of $M_{X\,rec}$ is presented in Fig. 9.1 in the form:

$$\frac{1}{N_{ei}}\frac{dN}{dM_{X\,rec}} = \frac{1}{N_{ei}}\frac{\Delta N(M_{X\,rec})}{\Delta M_{X\,rec}}. \qquad (9.1)$$

where $\Delta N(M_{X\,rec})$ denotes the number of rapidity gap events in the given $M_{X\,rec}$ bin and N_{ei} is the number of the photoproduction events before requiring the rapidity gap, but after the $E_{e'}$ cut. The bin width $\Delta M_{X\,rec} = 1\,\mathrm{GeV}$ is almost twice as large as the $M_{X\,rec}$ resolution for masses in the range $1 < M_X < 21\,\mathrm{GeV}$, so the bin-to-bin migrations remained on the level of about 20%.

9.2 Acceptance correction

The $M_{X\,rec}$ spectrum obtained from the data was corrected for the non diffractive contamination, the detector smearing and the acceptance effects by means of the multiplicative correction factors derived from the MC simulation. The result is expressed in terms of

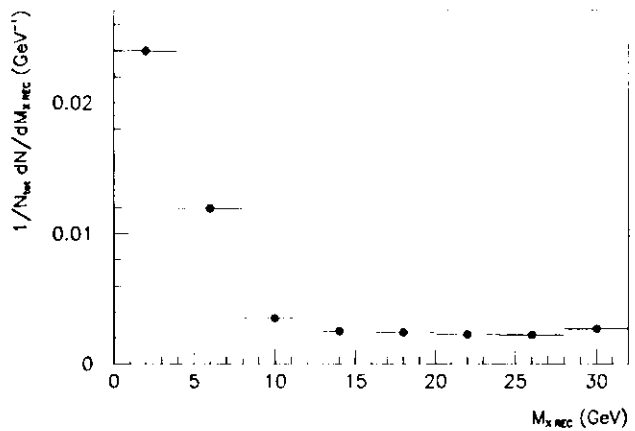

Figure 9.1: *Uncorrected distribution of the invariant mass reconstructed from the calorimeter in diffractive like events selected with the PRT1.*

the diffractive photon dissociation cross section relative to the total photoproduction cross section:

$$\frac{1}{\sigma_{tot}}\frac{d\sigma}{dM_X} = \frac{1}{N_{ei}}\frac{dN}{dM_{X\,rec}} \cdot (1 - Cont(M_X)) \cdot \frac{1}{Mig(M_X)} \cdot \frac{1}{Acc(M_X)} \cdot Acc_{tot} \qquad (9.2)$$

The contamination factor, $Cont(M_X)$, is defined as the ratio of the number of events due to non-diffractive reactions and the process $\gamma p \to XN$ with $M_X > 2\,\mathrm{GeV}$ to the total number of events passing the rapidity gap cut and observed in a bin of $M_{X\,rec}$. The bin to bin migration factor, $Mig(M_X)$, defines a ratio between the number of diffractive events that are reconstructed and the events that are generated in a given bin of the invariant mass, where only the events passing the selection cuts are taken into account. The $Acc(M_X)$ denotes the acceptance of the selection cuts for the process $\gamma p \to Xp, XN$, where $M_X < 2\,\mathrm{GeV}$, as a function of the generated mass. The Acc_{tot} is the global trigger acceptance. Figure 9.2 shows the behaviour of the contamination, migration and acceptance correction factors as a function of M_X. For $M_X > 8\,\mathrm{GeV}$ the correction for the acceptance and migration effects is almost negligible, as the corresponding factors are constant and close to unity. However, the very small non-diffractive contamination at low masses increases with growing invariant mass reaching 10% at $M_{X} \approx 21\,\mathrm{GeV}$. Therefore, the shape of the diffractive M_X spectrum after the acceptance correction will depend on the level of the non diffractive contamination estimated from the MC simulation. This level is directly related to the ratio of the contributions from diffractive and non diffractive processes in the MC simulation. This ratio was originally determined from the partial photoproduction cross sections measured at HERA (see section 6.5). However, due to a limited precision, such a method could not be used in this analysis. Instead, the relative contribution of the diffractive and non diffractive channels in the MC simulation was adjusted so as to reproduce the ratio of the number of the rapidity gap events with $8 < M_{X\,rec} < 20\,\mathrm{GeV}$ and the non rapidity gap events with CAL energy $E_{tot} > 60\,\mathrm{GeV}$ in the data. The former data sample is dominated by diffractive processes with the dissociated photon mass far from the region

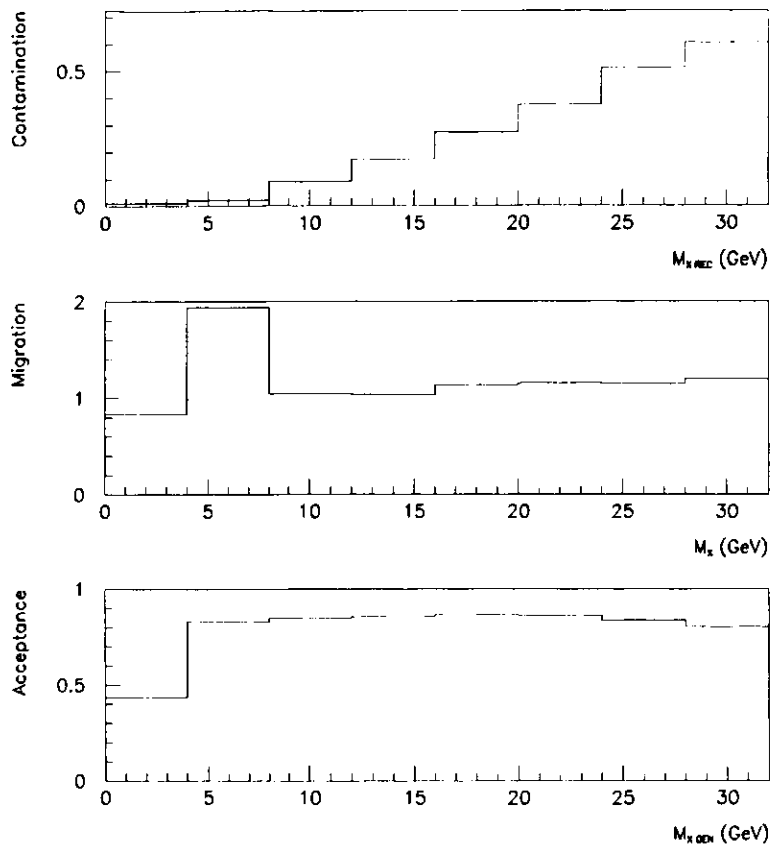

Figure 9.2: *The contamination correction factor, migration factor and acceptance for the photon dissociation process determined from the MC simulation.*

of low M_X resonances, while the latter sample is due to non diffractive interactions. The ratio of the two channels in the MC simulation derived in this way may slightly depend on the characteristics of the simulated events. Therefore, this normalization procedure was performed independently for all the combinations of the used MC models. In all cases the results were consistent with the corresponding ratio between the photoproduction cross sections measured in [28].

The M_X spectrum after all the corrections is presented in Fig. 9.3. The statistical error of the corrected data combines the statistical error of the data and that of the correction factor. For comparison, the shape of the uncorrected distribution is also shown.

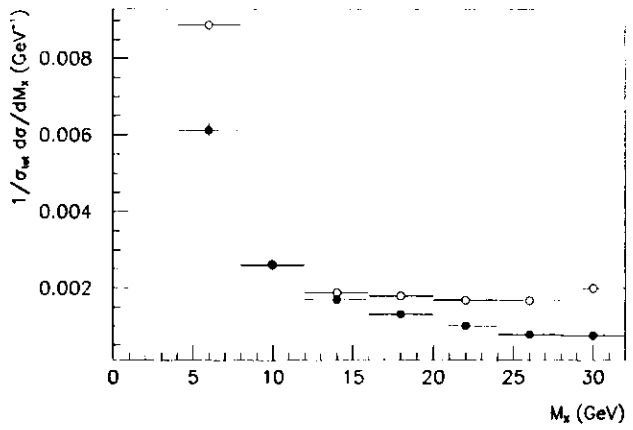

Figure 9.3: *The corrected spectrum of diffractively dissociated photon mass (solid points). For comparison, the uncorrected spectrum scaled by the overall trigger acceptance, $\frac{1}{N_{ev}}\frac{dN}{dM_{X\,rec}} \cdot Acc_{tot}$ is also included (open points).*

9.3 MC reweighting

The acceptance corrected diffractive mass spectrum was fitted in the interval $8 < M_X < 21$ GeV with the triple Regge formula from Eq. 2.15 integrated over t:

$$\frac{d\sigma}{dM_X} = \int_{-\infty}^{t_{max}} 2M_X \cdot \frac{d^2\sigma}{dtdM_X^2} dt \sim \frac{1}{b_0 + 2\alpha'_P ln\frac{W^2}{M_X^2}} \cdot \frac{1}{M_X^{2\alpha_P(0)-1}} \tag{9.3}$$

The higher integration limit $t_{max} = -m_p^2(M_X^2/s)^2$ at HERA energies is consistent with 0. The dependence of the effective t slope on M_X may significantly distort the power like behaviour of the diffractive mass spectrum at low M_X and was therefore incorporated into the fitted function. The parameter values of $\alpha'_P = 0.25\,\mathrm{GeV}^{-2}$ [7] and $b_0 = 5\,\mathrm{GeV}^{-2}$ [8] were assumed in accord with the results of the experiments at lower energy.

The fit to the corrected M_X spectrum resulted in the value of $\alpha_P(0) = 1.15 \pm 0.01$. As a consistency check, the diffractive MC event sample used for the acceptance correction was reweighted according to Eq. 9.3 with the measured value of $\alpha_P(0)$. The diffractive MC event sample was combined with other subprocesses following the procedure described in section 9.2 and was used to repeat the correction of the $M_{X\,rec}$ spectrum. The fit of Eq. 9.3 to the obtained distribution gave the same value of $\alpha_P(0)$. To verify the sensitivity of the result to the $\alpha_P(0)$ assumed in the diffractive MC sample used for the acceptance correction, the diffractive MC events were reweight assuming $\alpha_P(0) = 1.0$ and the measurement was repeated. The obtained value was consistent with the first result. Figure 9.4 shows the comparison of the $M_{X\,rec}$ spectrum in the data and in the MC simulation assuming either $\alpha_P(0) = 1.0$ or the measured value of $\alpha_P(0) = 1.15$. In the second case the MC description of the region $M_{X\,rec} > 8$ GeV is satisfactory, but below that value a significant discrepancy between the data and the MC simulation is observed. Although this region is not directly used for the measurement, the observed discrepancy may affect the result due to tails of the

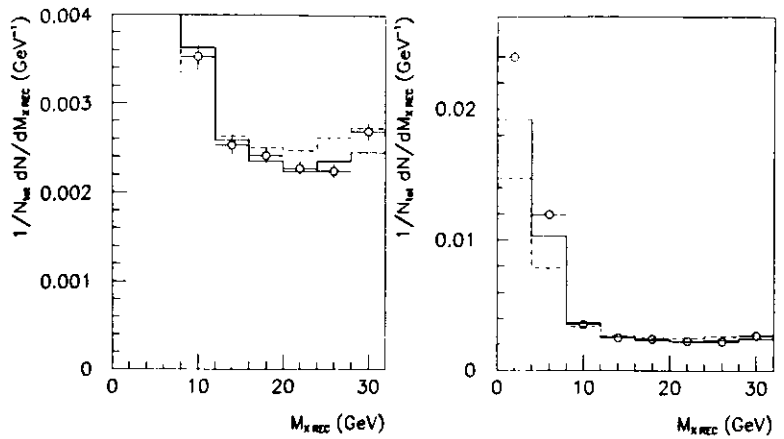

Figure 9.4: *The reconstructed mass spectrum of diffractive like events in the data (points), the MC simulation with $\alpha_P(0) = 1.0$ (dashed line) and $\alpha_P(0) = 1.11$ (solid line). The left plot is zoomed on the tail of the $M_{X\,rec}$ distribution while the right one shows the whole spectrum.*

$M_{X\,rec}$ resolution function leading to some migration between distant mass bins. The effect can be verified only with the MC model where the low M_X region of the diffractive spectrum is correctly described. Unfortunately, there exists neither a reliable theoretical prediction nor a precise experimental measurement of the low M_X region of the dissociated photon mass spectrum. Therefore, the necessary adjustment of the low M_X shape in the diffractive MC simulation was performed by means of iterative fitting to the data. Three factors, f_1, f_2, f_3, scaling the simulated mass spectrum in the intervals of $1.1 < M_X < 2$ GeV, $2 < M_X < 4$ GeV and $4 < M_X < 6$ GeV respectively were defines as parameters of the fit. The scaling was done relative to the triple pomeron shape of Eq. 9.3. The goal of the fitting procedure was the minimization of the χ^2 defined as:

$$\chi^2 = \sum_j \frac{(n_{data}(j) - n_{MC}(j))^2}{\sigma^2_{data}(j) + \sigma^2_{MC}(j)}, \tag{9.4}$$

where $n_{data}(j)$ and $n_{MC}(j)$ indicate the number of events in bin j of the $M_{X\,rec}$ distribution in the data and the MC respectively, while $\sigma_{data}(j)$ and $\sigma_{MC}(j)$ are the corresponding statistical errors. To compare only the shapes of the $M_{X\,rec}$ spectra the MC distribution was normalized to the data before the χ^2 calculation. To increase the sensitivity of the result to the fine structure in the low mass region the width of the bins was reduced to $\Delta M_{X\,rec} = 1$ GeV. The fitting procedure resulted in the following values of the scaling factors: $f_1 = 1.6 \pm 0.7$, $f_2 = 1.7 \pm 0.4$, $f_3 = 1.0 \pm 0.2$. The errors reflect the spread of the results obtained with different combinations of MC models and when the contribution from the vector meson production process is varied within the limits described in section 6.5. These results were obtained assuming the values of the $\alpha_P(0)$ derived separately for each combination of the MC models from the $M_{X\,rec} > 8$ GeV region of the spectrum in the data. Figure 9.5 compares the fine binned $M_{X\,rec}$ distribution in the data and MC simulation after reweighting the low

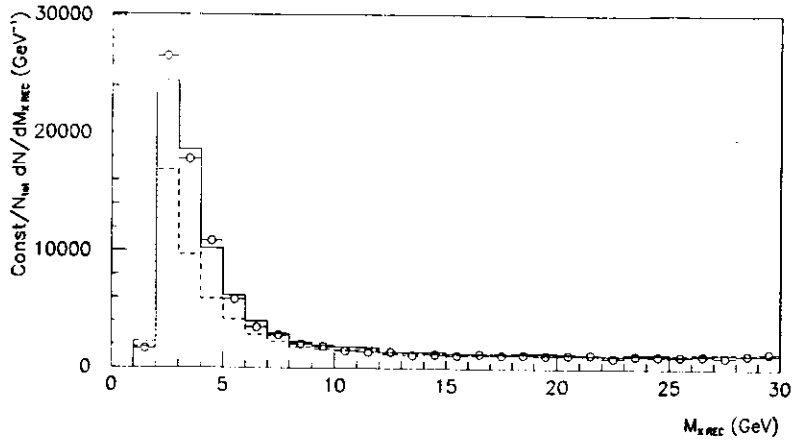

Figure 9.5: *The reconstructed mass spectrum of diffractive like events in the data (points) compared to the result of the MC simulation with $\alpha_P(0) = 1.0$ (dashed line), $\alpha_P(0) = 1.15$ (dotted line) and after additional reweighting of the low diffractive mass region (solid line).*

diffractive mass region. For comparison the spectrum from the MC simulation before the reweighting is also shown.

9.4 Results

The diffractive MC event samples reweighted according to the results of the fits discussed in the previous section were combined with other subprocesses and were finally used to correct the invariant mass distribution measured in the data. The corrected mass spectrum was fitted in the interval $8 < M_X < 21$ GeV with Eq. 9.3 converted to the form where the $\alpha_P(0)$ parameter defining the shape and the overall normalization factor A are practically uncorrelated:

$$\frac{1}{\sigma_{tot}}\frac{d\sigma}{dM_X} = A \cdot \frac{d\sigma(M_X, \alpha_P(0))}{dM_X} \Big/ \frac{\sigma(M_X = 11\,\text{GeV}, \alpha_P(0))}{dM_X} \tag{9.5}$$

The following values were obtained: $\alpha_P(0) = 1.11 \pm 0.01$ and $A = (11.5 \pm 0.3) \cdot 10^{-4}$ GeV^{-1}. The result of the fit is shown in Fig. 9.6.

9.5 Systematic uncertainties

The analysis was repeated using various acceptance correction and fitting methods and the difference between the obtained results was used to estimate the systematic uncertainty. Table 9.1 summarizes the outcome of these checks. The largest uncertainty is related to the poor understanding of the noise and the efficiency of the PRT1 used to select the rapidity gap events. It was evaluated by repeating the measurement without requiring the coincidence between the two counters layers, as discussed in section 7.2. The result also depends on

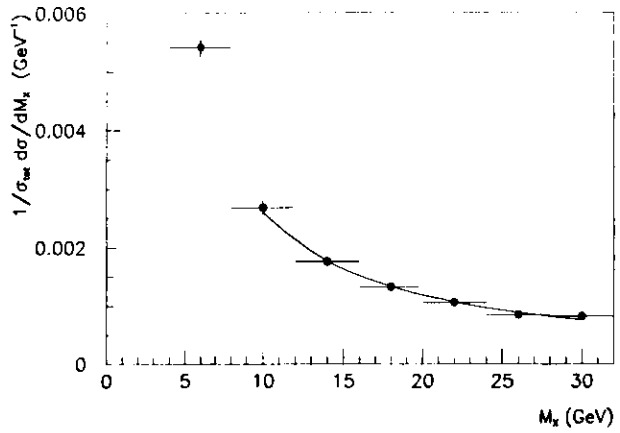

Figure 9.6: *The corrected distribution of the dissociated photon mass in photoproduction at* $\langle W \rangle = 200\,\mathrm{GeV}$. *The line is the result of the fit of the formula 9.3 derived from the triple pomeron relation 2.15.*

source of the uncertainty	$\sigma_{syst}(\alpha_P(0))$	$\sigma_{syst}(A)(10^{-1}\,\mathrm{GeV}^{-1})$
PRT1 noise and efficiency	0.06	1.1
non diffractive contamination	0.05	3.1
M_X reconstruction	0.01	0.2
increased CAL FLT thresholds	0.01	0.2
diffractive MC	0.03	1.5
fitting interval	0.01	0.1
dependence on b_0	0.01	0.1
dependence on α'_P	0.01	0.0

Table 9.1: *Individual contributions to the systematic error on* $\alpha_P(0)$ *and* A.

the way the non diffractive background is modelled in the acceptance correction procedure. This effect was estimated by using the PYTHIA to simulate the non diffractive interactions instead of the EPSOFT program (see chapter 6). In addition to these two dominant sources of systematic error a number of other effects was studied. The sensitivity to the precision of the diffractive mass reconstruction was verified by using an alternative method of M_X determination (see section 7.3). The influence of possible trigger inefficiencies was checked by repeating the whole analysis with higher trigger thresholds (see section 5.2.1). To verify the dependence on the MC simulation of the diffractive process used for the acceptance correction, the EPSOFT program was used instead of the NZ (chapter 6). To check the stability of the fitting procedure the fit was repeated using an extended interval of $8 < M_{X\,rec} < 32\,\mathrm{GeV}$. To examine the dependence of the result on the assumed parameter values the t slope parameter was changed from $b_0 = 1\,\mathrm{GeV}^{-2}$ to $5\,\mathrm{GeV}^{-2}$ and $\alpha'_P = 0.20\,\mathrm{GeV}^{-2}$ was used instead of the original value of $0.25\,\mathrm{GeV}^{-2}$. To estimate the overall systematic uncertainty all the error contributions were added in quadratures.

The final result is $\alpha_P(0) \quad 1.11 \pm 0.01(stat) \pm 0.08(syst)$ and $A \quad [14.5 \pm 0.03(stat) \pm 3.7(syst)] \cdot 10^{-1}\,\mathrm{GeV}^{-1}$.

Chapter 10

Discussion

The following chapter contains a discussion of the results obtained in this analysis. The next two sections are dedicated to the soft and hard non diffractive photoproduction reactions. The results on the diffractive processes are examined in section 10.3. Section 10.4 contains a discussion of the possible applications and more general implications of the EPSOFT MC program developed for the presented analysis.

10.1 Soft non–diffractive photoproduction

In chapter 8 a measurement of the p_T spectrum of charged particles produced in non diffractive photoproduction reactions at an average c.m. energy of $\langle W \rangle = 180$ GeV was presented. The considered laboratory pseudorapidity range $-1.2 < \eta < 1.4$, equivalent to $-3.3 < \eta_{c.m.} < -0.7$ in the γp c.m. system, corresponds mainly to the region of photon fragmentation. The low p_T part of the spectrum, attributed to soft hadronic interactions, may be described with thermodynamical models. They predict a steep fall of the transverse momentum spectrum that can be approximated with the exponential form [14]:

$$\frac{1}{N_{ev}} \cdot \frac{d^2N}{dp_T^2 d\eta} = exp(a - b \cdot \sqrt{p_T^2 + m_\pi^2}), \qquad (10.1)$$

where m_π is the pion mass. This relation provides a good description of the ZEUS data from the lowest measured value of 0.3 GeV up to approximately 1.2 GeV as shown in Fig. 10.1. The fit in this interval gives the value of the exponential slope $b = 1.91 \pm 0.09(stat) \pm 0.19(syst)$ GeV^{-1}. The systematic error was estimated by varying the relative inclusive cross sections within the systematic error limits (see section 8.5) and by varying the upper boundary of the fitted interval from 1.0 GeV to 1.1 GeV. A similar fit to the inclusive p_T spectrum of charged particles produced in $p\bar{p}$ collisions at a c.m. energy of $\sqrt{s} = 200$ GeV [75] gives an exponential slope $b = 1.87 \pm 0.13$ GeV^{-1} [75]. Interpreted in the frame of the thermodynamical models this result indicates that the temperature of the hadronic matter in soft photoproduction and hadron hadron collisions at comparable energies is very similar. This behaviour is fully consistent with the VDM.

10.2 Hard photoproduction

The non diffractive spectrum in Fig. 10.1 clearly departs from the exponential shape at high p_T values. Such a behaviour is expected from the contribution of the hard scattering

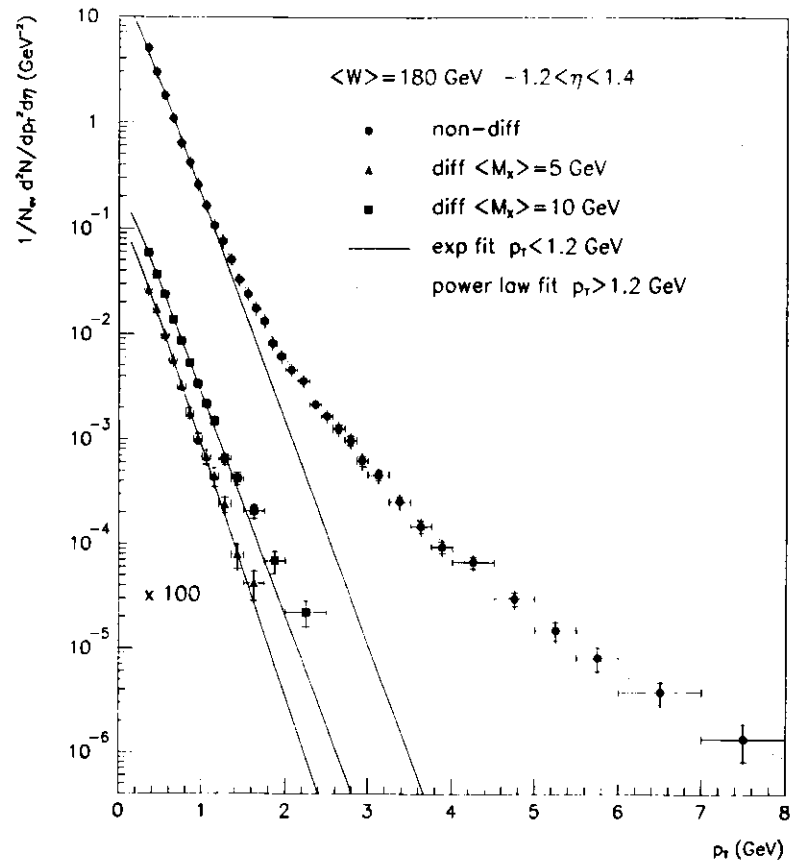

Figure 10.1: *Inclusive transverse momentum distributions of charged particles in photoproduction events at $\langle W \rangle = 180$ GeV averaged over the pseudorapidity interval of $-1.2 < \eta < 1.1$. The inner error bars indicate the statistical errors and the outer ones represent the quadratic sum of the statistical and systematic errors. Solid lines indicate fits of Eq. 10.1 to the data in the region of $p_T < 1.2$ GeV. The dotted line shows a power law formulae (Eq. 10.2) fitted to the non diffractive data for $p_T > 1.2$ GeV. For the sake of clarity the diffractive points are shifted down by two orders of magnitude.*

of partonic constituents of the colliding particles, a process that can be described in the framework of perturbative QCD. It results in a high p_T behaviour of the inclusive spectrum that can be approximated by a power law formula:

$$\frac{1}{N_{ev}} \cdot \frac{d^2N}{dp_T^2 d\eta} = A \cdot (1 + \frac{p_T}{p_{T0}})^{-n} \qquad (10.2)$$

	$p_{T\,0}$	n	A
$p_{T\,0}$	$0.32 \cdot 10^{-3}$	$0.18 \cdot 10^{-3}$	$-0.10 \cdot 10^{1}$
n		$0.12 \cdot 10^{-2}$	$-0.12 \cdot 10^{1}$
A			$0.32 \cdot 10^{1}$

Table 10.1: *The covariance matrix corresponding to the fit of equation (10.2) to the non diffractive data for $p_T > 1.2$ GeV.*

where A, $p_{T\,0}$ and n are the parameters determined from the data. The fit to the data points in the region of $1.2 < p_T < 8$ GeV gives a good description of the data and results in the parameter values $p_{T\,0} = 0.51$ GeV, $n = 7.25$ and $A = 391$ GeV^{-2}. The statistical precision of these numbers is described by the covariance matrix given in Table 10.1. The fitted function is shown in Fig. 10.1 as a dotted line.

In Fig. 10.2 the photoproduction p_T spectrum is presented together with the results of a similar measurement from the H1 collaboration at $\langle W \rangle = 200$ GeV [76] and the data from the WA69 photoproduction experiment at a c.m. energy of $\langle W \rangle = 18$ GeV [5]. For the purpose of this comparison, the inclusive cross sections published by those experiments were divided by the corresponding total photoproduction cross sections [29, 31]. The results of this analysis are in agreement with the H1 data. The comparison with the WA69 data shows that the transverse momentum spectrum becomes harder as the energy of the γp collision increases. Figure 10.2 also shows the functional fits of the Eq. 10.2 to $p\bar{p}$ data from UA1 and CDF at various c.m. energies [75, 77]. These fits correspond to the inclusive cross sections divided by the cross section values used by these experiments for the absolute normalization of their data. The inclusive p_T distribution in photoproduction at $\langle W \rangle = 180$ GeV is clearly harder than the distribution for $p\bar{p}$ interactions at a similar c.m. energy and in fact is similar to $p\bar{p}$ at $\sqrt{s} = 900$ GeV.

This comparison indicates that in spite of apparent similarity in the low p_T region between photoproduction and proton antiproton collisions at a similar c.m. energy, the two reactions are different in the hard regime. There are many possible reasons for this behaviour. Firstly, both of the $p\bar{p}$ experiments used for the comparison measured the central rapidity region ($|\eta_{c.m.}| < 2.5$ for UA1 and $|\eta_{c.m.}| < 1$ for CDF), while this data correspond to $-3.3 < \eta_{c.m.} < -0.7$. Secondly, according to VDM, the bulk of the γp collisions can be approximated as an interaction of a vector meson V with the proton. The p_T spectrum of Vp collisions may be harder than $p\bar{p}$ at a similar c.m. energy, since the parton momenta of quarks in mesons are on average larger than in baryons. Thirdly, in the picture where the photon consists of a resolved part and a direct part, both the anomalous component of the resolved photon and the direct photon become significant at high p_T and make the observed spectrum harder compared to that of Vp reactions.

Figure 10.3 shows the comparison of the results of this measurement with the theoretical prediction obtained recently from NLO QCD calculations [78]. The charged particle production rates in a non diffractive event were converted to inclusive non-diffractive cross sections by multiplying by the non diffractive photoproduction cross section of $\sigma_{nd}^{\gamma p} = 91 \pm 11$ μb [28]. The theoretical calculations use the GRV parametrization of the parton densities in the photon and the CTEQ2M parametrization for partons in the proton [79]. The NLO fragmentation functions describing the relation between the hadronic final state and the

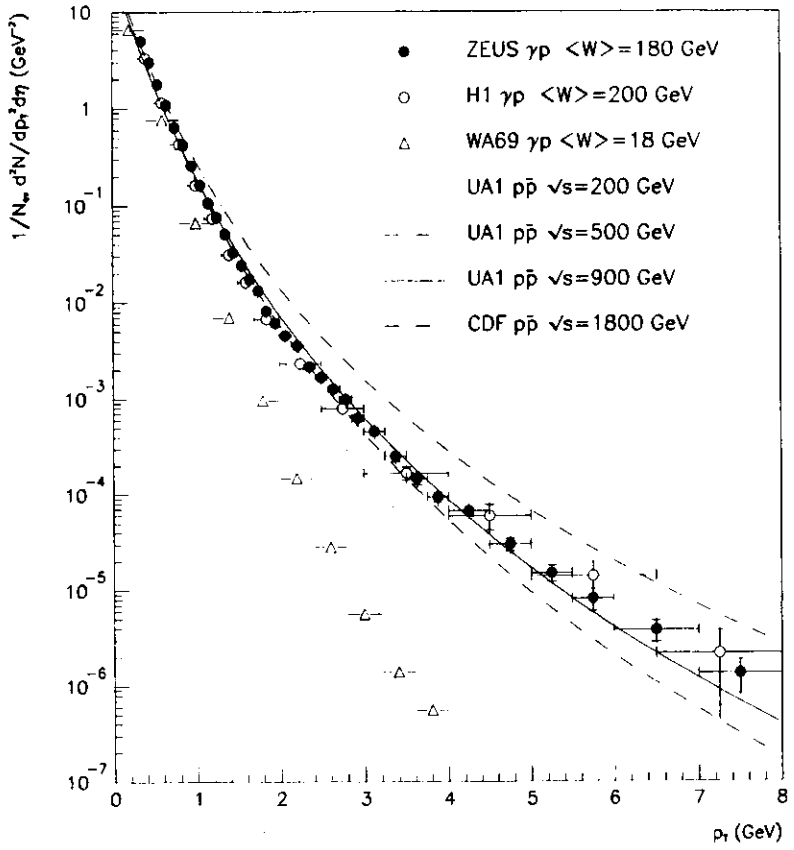

Figure 10.2: *Comparison of non diffractive transverse momentum spectrum with the data from H1 [76], OMEGA [5], UA1 [75] and CDF [77]. The inner error bars indicate the statistical errors and the outer ones represent the quadratic sum of the statistical and systematic errors.*

partonic level were derived [80] from the e^+e^- data. The calculation depends strongly on the parton densities in the proton and in the photon, yielding a spread in the predictions of up to 30% due to the former and 20% due to the latter. The factorization scales of the incoming and outgoing parton lines, as well as the renormalization scale, were all set to p_T. The uncertainty due to the ambiguity of this choice was estimated by changing all three scales up and down by a factor of 2. The estimates of the theoretical errors were added in quadrature and indicated in Fig. 10.3 as a shaded band. The theoretical calculation is in good agreement with the experimental results.

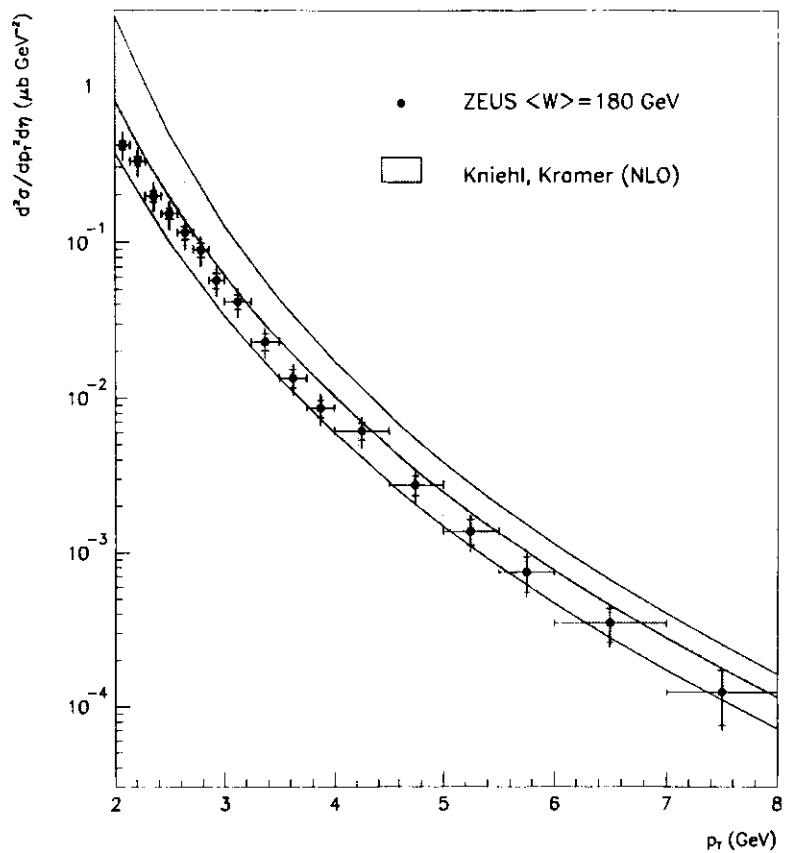

Figure 10.3: *Comparison of the inclusive cross sections for non diffractive photoproduction at $\langle W_{\gamma p} \rangle = 180$ GeV with the NLO QCD calculation results from [78]. The inner error bars on the data points indicate the statistical errors and the outer ones represent the quadratic sum of the statistical and systematic errors. The shaded band corresponds to the uncertainty of the theoretical calculation.*

10.3 Diffractive photoproduction

In chapter 9 a measurement of the invariant mass distribution of the diffractively dissociated photon was presented. It was performed for the reactions $\gamma p \to Xp, XN$, were N is the nucleonic system with $M_N < 2$ GeV, at an average c.m. energy $\langle W \rangle = 200$ GeV. The obtained spectrum of diffractive masses in the range $8 < M_X < 24$ GeV can be described by the triple pomeron Regge formula (Eq. 2.15) with the pomeron intercept of $\alpha_P(0) = 1.14 \pm 0.01(stat) \pm 0.08(syst)$. The single diffractive dissociation was recently studied in $p\bar{p}$ collisions at c.m. energies of $\sqrt{s} = 546$ GeV and 1.8 TeV [33]. The results fitted

sample	b[GeV^{-1}]	$\sigma_{stat}(b)$	$\sigma_{syst}(b)$	a	$\sigma_{stat}(a)$	$cov(a,b)$
non-diffractive	4.91	0.09	0.19	3.39	0.09	-0.011
diff $\langle M_X \rangle$ 5 GeV	5.91	0.17	0.19	2.78	0.10	-0.016
diff $\langle M_X \rangle$ 10 GeV	5.28	0.10	0.17	3.31	0.06	-0.006

Table 10.2: *The values of the parameters resulting from the fits of Eq. 10.1 to ZEUS data in the interval $0.3 < p_t < 1.2$ GeV. The σ_{stat} and σ_{syst} indicate the statistical and systematic errors (in GeV^{-1} for b).*

with similar triple pomeron relation indicate $\alpha_P(0) = 1.121 \pm 0.011(stat) \pm 0.011(syst)$ for the lower c.m. energy and $\alpha_P(0) = 1.103 \pm 0.017(stat) \pm 0.011(syst)$ for the higher one. The $\alpha_P(0)$ value obtained in this analysis is consistent with both measurements, indicating that the diffractive dissociation of photons is very similar to that of a hadron, which is in full accord with the VDM. The Regge theory allows to relate the M_X behaviour in diffractive processes to the W dependence of the total and the elastic cross sections. The pomeron intercept of $\alpha_P(0) = 1.08$ [23] used in the parametrization successfully describing all the total and elastic photoproduction cross sections (see section 2.2.3) is also consistent with the result of this measurement. Therefore, within the achieved experimental precision this result confirms the applicability of the Regge phenomenology for the description of the diffractive photoproduction.

However, the presented measurement leaves one question open. The comparisons of the reconstructed M_X spectrum in the data and in the MC simulation indicate a significant excess of diffractive events with $1.1 < M_X < 1$ GeV over the level expected from the triple pomeron relation. The poor resolution of this measurement in the low M_X region does not allow to determine whether the effect is due to a single resonance, unexpectedly high non resonant cross section or a very different behaviour of the ρ^0, ω and ϕ production with respect to what was simulated in the MC. Only a part of the effect may be ascribed to the resonant J/Ψ production since the excess of events in the data over the model expectations corresponds to the γp cross section of the order of 1 μb, while the elastic J/Ψ photoproduction cross section is of the order of 0.1 μb [81]. It is also not clear if one should expect the triple pomeron relation derived in the asymptotic limit $M_X^2 \to \infty$ to work for such low masses.

Chapter 8 presented a measurement of the inclusive p_t spectra of charged particles emitted in the photon fragmentation region in the diffractive reactions $\gamma p \to Xp, XN$ were N denotes a nucleonic system with $M_N < 1$ GeV. The measurement was performed at $\langle W \rangle = 180$ GeV in two intervals of the dissociated photon mass with mean values $\langle M_X \rangle = 5$ GeV and 10 GeV. In the interval of $0.3 < p_t < 1.2$ GeV the two obtained diffractive spectra can be described with the exponential form (Eq. 10.1). The result of the fit is shown in Fig. 10.1. The obtained values of the exponential slope b and the parameter a are listed together with the non diffractive result in table 10.2. The systematic errors were calculated like in case of the non diffractive data (see section 10.1). In Fig. 10.1 the values of the b parameter resulting from the fits of Eq. 10.1 to pp and $p\bar{p}$ data are presented as a function of the c.m. energy. The slope measured in non-diffractive photoproduction is also included. The diffractive slopes agree better with the hadronic data corresponding to lower c.m. energy. In Fig. 10.1 the ZEUS diffractive points are plotted at 5 GeV and 10 GeV, the values of the invariant mass of the dissociated photon. A similar behaviour has been observed for the diffractive dissociation of hadrons, i.e. the scale of the fragmentation of the dissociated system is related to the value of its mass rather than to the total c.m. en-

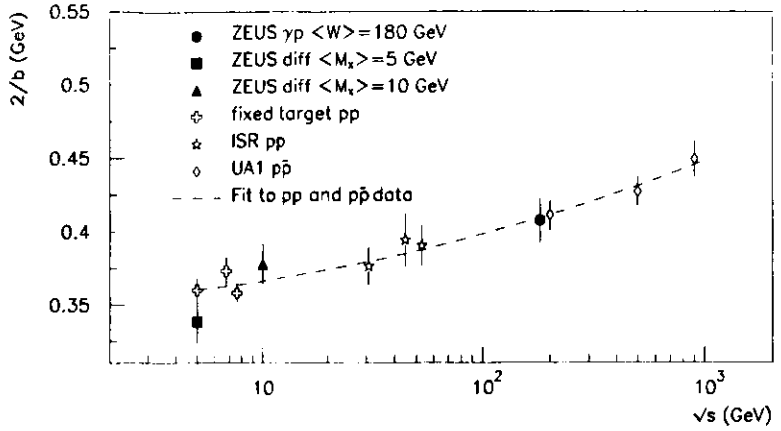

Figure 10.4: *Inverse slope of the p_t spectrum from the fit of Eq. 10.1 vs. the c.m. energy for different experiments. The fixed target data were taken from [82, 83, 84]. ISR [85], UA1 [75]. The ZEUS non diffractive point is placed at the photon proton c.m. energy. The diffractive points are plotted at the energies corresponding to the mean value of the invariant mass (M_X). The error bars indicate the quadratic sum of the statistical and systematic errors. The dashed line is a parabola in log(s) and was fitted to all the hadron hadron points to indicate the trend of the data.*

ergy [18, 19, 7] (see section 2.2.2). This measurement is another example of close similarities between the diffractive dissociation of photons and that of hadrons, as expected from the VDM.

10.4 EPSOFT

One of the important outcomes of this study is the MC program EPSOFT. It simulates soft diffractive and non diffractive collisions of hadronic photons with protons. It has been tuned to the ZEUS photoproduction data. The EPSOFT generator turned out to be very useful also in other analyses of photoproduction at ZEUS since it correctly describes the hadronic final states observed in soft γp interactions at HERA. The program was written in such a way that it can be also used to simulate the interactions of photons of higher virtualities. The dynamics of the simulated process is assumed not to depend on the photon virtuality in any way. The only dependence on Q^2 enters through the kinematical constraints. Surprisingly the EPSOFT turned out to be very useful also in some analysis of the Deep Inelastic Scattering ($Q^2 >> 1$ GeV^2). In particular the studies of diffraction in DIS have profited from EPSOFT since it works in the kinematical regions where the simulation programs based on QCD models usually fail, e.g. region of very low values of M_X where the full simulation of QCD radiation and the subsequent hadronization can not be performed due to lack of the phase space. Even more surprising is the fact that EPSOFT correctly simulates many of the features of the hadronic final states in non diffractive DIS. To illustrate this observation a comparison of one of the measurements of charged particle production in DIS with the

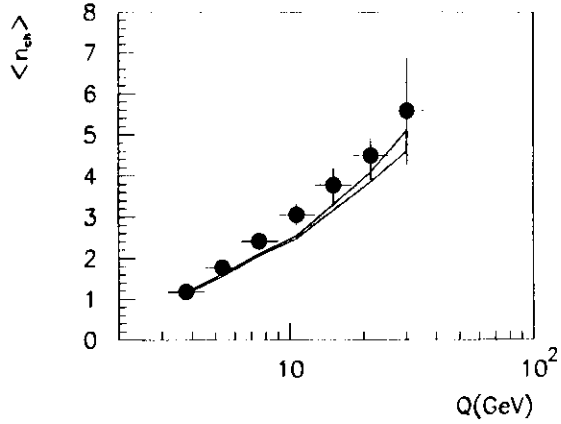

Figure 10.5: *Mean multiplicity of charged particles in the current region of the Breit frame in DIS as a function of Q. The ZEUS data [87] (points) is compared to the results of the EPSOFT simulation (shaded band).*

prediction from EPSOFT is presented below.

The charged particle production in DIS at HERA was studied in the Breit frame [86] defined such that the virtual photon exchanged between the electron and the proton is completely space-like - it has no energy but only a momentum along the Z direction. Within the quark parton model (QPM), viewing the DIS as the process where the virtual photon couples directly to a charged parton inside the proton, the Breit frame is the most natural reference system to study the particle production. In this frame the Z-component of the momentum of the incoming quark is $Q/2$ before the interaction and changes to $-Q/2$ by the absorption of the virtual photon. The particles produced in DIS can be assigned to one of two regions depending on the Z component of the momentum. The current region corresponds to the direction of the outgoing struck quark.

The multiplicity and the momentum spectra of charged particles produced in the current region of the Breit frame in DIS were measured with the ZEUS detector. The obtained dependence of the mean multiplicity on Q is compared to the results of the simulation with EPSOFT in Fig. 10.5. The MC simulation correctly reproduces the observed relation. Figure 10.6 shows the peak position of the $ln(1/x_p)$ distribution vs. Q, where the scaled momentum is defined as $x_p = 2p/W$. Also in this case EPSOFT correctly describes the measured dependence. This agreement is somewhat surprising since the studied quantities clearly depend on Q and there is no explicit dependence of the particle production on the photon virtuality in the EPSOFT generator. This suggest strong phase space effects in the measurements of particle production in the current region of the Breit frame vs. Q. A closer examination confirms this, as the size of the kinematically available phase space attributed to the current region of the Breit frame increases with growing Q which determines the gross features of the observed dependencies. This example shows that the simulation of particle production according to longitudinal phase space, as it is done in EPSOFT, is sufficient to reproduce many properties of hadronic final states in DIS. It is therefore often easier and

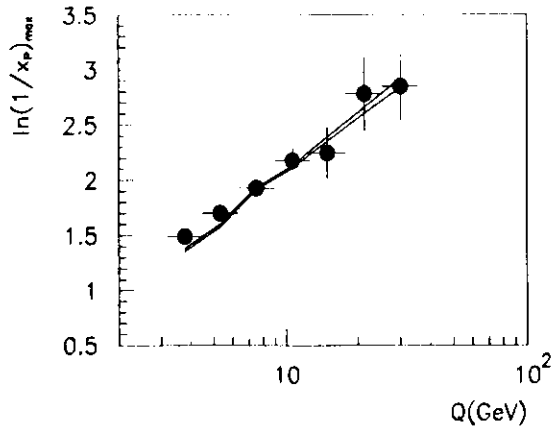

Figure 10.6: *Peak position of the $\ln(1/x_p)$ distribution in the current region of the Breit frame in DIS as a function of Q. The ZEUS data [87] (points) is compared to the results of the EPSOFT simulation (shaded band).*

more educative to use a simple MC simulation program like EPSOFT than to work with a complicated MC simulation of QCD processes.

Chapter 11

Conclusions

The properties of photoproduction reactions at c.m. energies $W \approx 200$ GeV were studied using the ZEUS detector at the HERA collider.

The inclusive transverse momentum spectrum of charged particles measured in non diffractive reactions falls exponentially in the low p_t region in accord with thermodynamical models of soft interactions. The exponential slope is consistent with that measured in hadron hadron reactions at similar c.m. energies. This behaviour of soft non diffractive photoproduction is consistent with the VMD. In the region of high p_t the non diffractive spectrum clearly departs from the exponential shape. Compared to photoproduction data at a lower c.m. energy, a hardening of the transverse momentum spectrum is observed as the collision energy increases. The shape of the p_t spectrum is comparable to that of $p\bar{p}$ interactions at $\sqrt{s} = 900$ GeV. The results from a NLO QCD calculation including the direct and the resolved photon interactions agree with the measured cross sections for inclusive charged particle production.

An extensive study of the diffractive dissociation of photons was presented. The distribution of the dissociated photon mass in the region $8 < M_X < 21$ GeV can be described with the triple pomeron Regge formula with the pomeron intercept of $\alpha_{I\!P}(0) = 1.11 \pm 0.01(stat) \pm 0.08(syst)$. This is consistent with the value obtained in the measurement of single diffraction in pp collisions and with the pomeron intercept that correctly describes the total and elastic photoproduction cross sections. Within the available experimental precision this results confirms the applicability of VMD and the Regge phenomenology for the description of diffractive photoproduction. A significant excess of diffractive events with $1.1 < M_X < 1$ GeV over the level expected from the triple pomeron relation was observed in the data. However, due to poor experimental resolution at low M_X it was not possible to identify the nature of the effect in this analysis. The p_t spectra of charged particles produced in the diffractive dissociation of photons were measured in two intervals of the dissociated photon mass with mean values $\langle M_X \rangle = 5$ GeV and 10 GeV. The p_t spectra fall exponentially in the low p_t region, with slopes consistent with hadronic data at a c.m. energy equal to the invariant mass of the diffractive system. A similar behaviour has been observed in the diffractions of hadrons. This analogy between dissociation of photons and hadrons is another confirmation of VMD for diffractive photoproduction reactions.

The results presented in this thesis allow to draw the following three general conclusions:
- the VMD correctly models the soft photoproduction reactions also at HERA energies,
- the diffractive dissociation of photons is correctly described by the Regge phenomenology,
- the properties of photon proton collisions in the hard regime are consistent with QCD.

An important result of this study is the EPSOFT MC program simulating soft diffractive and non diffractive collisions of the photon with the proton. The program was tuned to correctly describe the hadronic final states observed in photoproduction at HERA. The EPSOFT generator can also be used to simulate the interaction of virtual photons and it successfully reproduces many features of multiparticle final states in DIS.

Bibliography

[1] T.H.Bauer et al., Rev. Mod. Phys. 50 (1978) 261.

[2] J.J.Sakurai, Ann. Phys. 11 (1960) 1.

[3] R.P.Feynman, Phys. Rev. Lett. 23 (1969) 1415.

[4] NA11 Collab., E.Auge et al., Phys. Lett. 169B (1986) 163;
NA11 Collab., R.Barate et al., Phys. Lett. 174B (1986) 158.

[5] OMEGA Photon Collab., R.J.Apsimon et al., Z. Phys. C43 (1989) 63.

[6] C.Geich-Gimbel, Int. Journal of Mod. Phys. A1, 7 (1989) 1527.

[7] K.Goulianos, Phys.Rep. 101 (1983) 169;
K.Goulianos, Nucl. Phys. B (Proc. Suppl.) 12 (1990) 110.

[8] T.J.Chapin et al., Phys. Rev. D31 (1985) 17.

[9] J.J.Sakurai and D.Schildknecht, Phys. Lett. B40 (1972) 121.

[10] E.M.Levin, L.L.Frankfurt, A.F.Ioffe, JETP Lett. 2 (1965) 65; H.J.Lipkin, F.Scheck, Phys. Rev. Lett. 16 (1966) 71.

[11] P.D.B.Collins, A.D.Martin, "Hadron Interactions", A.Hilger Ltd, Bristol (1984);

[12] Z.Koba, H.B.Nielsen and P.Olesen, Nucl. Phys. B40 (1972) 317.

[13] R.Szwed, G.Wrochna and A.K.Wróblewski, Mod. Phys. Lett. A5 (1990) 1851.

[14] R.Hagedorn, Riv. Nouvo Cim. 6 (1983) 1.

[15] ZEUS Collab., M.Derrick et al., Z. Phys. C69 (1995) 39.

[16] H1 Collab., S.Aid et al., DESY 95-251 (1995).

[17] UA5 Collab., R.E.Ansorge et al., Z. Phys. C33 (1986) 175.

[18] UA1 Collab., D.Bernard et al., Phys. Lett. B166 (1986) 459.

[19] EHS/NA22 Collab., M.Begalli et al., Z. Phys. C55 (1992) 531.

[20] A.Breakstone et al., Phys. Rev. D30 (1984) 528.

[21] T.Regge, Nouvo Cim. 14 (1959) 951.

[22] D.H.Perkins, "Introduction to High Energy Physics", Addison Wesley (1982).

[23] A.Donnachie, P.V.Landshoff, Nucl. Phys. B244 (1984) 322;
P.V.Landshoff, Nucl. Phys. B (proc.Suppl) 18C (1990) 211;
A.Donnachie and P.V.Landshoff Phys. Lett. B296 (1992) 227.

[24] I.Y.Pomeranchuk, Sov. Phys. JEPT 7 (1958) 499.

[25] E710 Collab., N.A.Amos et al., Phys Lett. B243 (1990) 158.

[26] CDF Collab., F.Abe et al., Phys. Rev. D, 50, 9 (1994) 5550.

[27] T.Armstrong et al., Phys. Lett. B228 (1989) 536.

[28] ZEUS Collab., M.Derrick et al., Z. Phys. C63(1994)391.

[29] H1 Collab., T.Ahmed et al., Int. Europhys. Conf. on HEP, Brussels (1995), EPS 474.

[30] Landolt-Börnstein, "Total Cross-Sections for Reactions of High Energy Particles", New Series, Vol. 12b, H.Schopper, Ed.(1987).

[31] H.Abramowicz, E.M.Levin, A.Levy and U.Maor, Phys. Lett. B269 (1991) 465.

[32] G.A.Schuler and T.Sjöstrand, Phys. Lett. B300 (1993) 169;
G.A.Schuler and T.Sjöstrand, Nucl. Phys. B407 (1993) 539.

[33] CDF Collab., F.Abe et al., Phys. Rev. D50 (1994) 5535.

[34] SWT Collab., Y. Eisenberg et al., Phys. Rev. D5 (1972) 15;
J. Park et al., Nucl. Phys. B 36 (1972) 401;
SBT Collab., J. Ballam et al., Phys. Rev. D5 (1972) 545;
SBT Collab, J. Ballam et al., Phys. Rev. D7 (1973) 3150;
W. Struczinski et al., Nucl. Phys. B108 (1976) 45;
OMEGA Collab., D. Aston et al., Nucl. Phys. B209 (1982) 56.

[35] J.K.Storrow, J. Phys. G: Nucl. Part. Phys. 19 (1993) 1641.

[36] H.Abramowicz et al., Int. Journal of Mod. Phys. A8 (1993) 1005.

[37] Yu.L.Dokshitzer, V.A.Khoze, A.H.Mueller, S.I.Troyan, "Basics of perturbative QCD", Frontieres (1991).

[38] ZEUS Collab., M.Derrick et al., Phys. Lett. B322 (1994) 287.

[39] G.Wolf, DESY 94-022 (1994).

[40] B.D.Burow, PhD Thesis, University of Toronto, DESY F35D-94-01 (1993).

[41] K.F.Weizsäcker, Z. Phys. 88 (1934) 612;
E.J.Williams, Phys. Rev. 45 (1934) 729.

[42] K.Charchula, J.Gajewski, Int. Journal of Mod. Phys. A9 (1994) 3229.

[43] G.Wolf, DESY 86-089 (1986).

[44] K.Piotrzkowski, M.Zachara, ZEUS 94-167.

[45] K.Piotrzkowski, M.Zachara, ZEUS 95-138.

[46] The ZEUS Detector, Status Report, DESY(1993).

[47] ZEUS Collab., M.Derrick et al., Phys. Lett. B293 (1992) 465.

[48] C.Alvisi et al., Nucl. Instr. Meth. A305 (1991) 30.

[49] N.Harnew et al., Nucl. Instr. Meth. A279 (1989) 290;
C.B.Brooks et al., Nucl. Instr. Meth. A283 (1989) 477;
B.Foster et al., Nucl. Phys. B, Proc. Suppl. B32 (1993) 181.

[50] M.Derrick et al., Nucl. Instr. Meth. A309 (1991) 77;
A.Andresen et al., Nucl. Instr. Meth. A309 (1991) 101;
A.Bernstein et al., Nucl. Instr. Meth. A336 (1993) 23.

[51] D.Kisielewska et al., DESY-HERA report 85-25 (1985);
J.Andruszkow et al., DESY 92-066 (1992).

[52] K.Piotrzkowski, PhD Thesis, Cracow, INP-Exp, DESY-F35D-93-06 (1993).

[53] K.Desler, U.Schneekoth, ZEUS Note 95-061 (1995).

[54] M.Kasprzak et al., ZEUS Note 92-072 (1992).

[55] U.Behrens et al., Nucl. Instr. Meth. A332 (1993) 253.

[56] L.A.T.Bauerdick et al., DESY 95-236 (1995).

[57] R.Brun et al., CERN DD/EE/84-1 (1987).

[58] J.Mainusch, PhD Thesis (Hamburg University), 1995, DESY F35D-95-11

[59] N.N.Nikolaev and B.G.Zakharov, Z. Phys. C53 (1992) 331;
P.Bruni et al., Proc. Workshop on Physics at HERA, DESY (1991) 363;
A.Solano, PhD Thesis (University of Torino), 1993.

[60] B.Andersson, G.Gustafson, G.Ingelman and T.Sjöstrand, Phys. Rep 97 (1983) 31.

[61] T.Sjöstrand, Z. Phys. C42 (1989) 301;
H-U.Bengtsson and T.Sjöstrand, Comput. Phys. Commun. 46 (1987) 43;
T.Sjöstrand, CERN-TH. 6488/92 (1992).

[62] P.Bruni and G.Ingelman, DESY 93-187, proceedings of the Europhysics Conf. on HEP, Marseille 1993.

[63] B.R.Webber, Ann. Rev. Nucl. Part. Sci. 36 (1986) 253;
G.Marchesini et al., Comput. Phys. Comm. 67 (1992) 465.

[64] T.Sjöstrand, M. van Zijl, Phys. Rev. D36 (1987) 2019.

[65] M.Glück, E.Reya and A.Vogt, Phys. Rev. D45 (1992) 3986.

[66] A.D.Martin, W.J.Stirling and R.G.Roberts, Phys. Lett. B306 (1993) 145.

[67] G.Marchesini, B.R.Webber, Nucl. Phys. B310 (1988) 527.

[68] A.M.Rossi, Nucl. Phys. B84 (1975) 269.

[69] UA1 Collab., C.Albajar et al., Nucl. Phys. B335 (1990) 261.

[70] S.Jadach, Comp.Phys.Comm. 9 (1975) 297.

[71] G.Levman, private communications.

[72] G.Wolf, private communications.

[73] Y.Iga, DESY 95-005 (1995).

[74] P.Billoir and S.Qian, Nucl. Instr. Meth. A311 (1992) 139.

[75] UA1 Collab., C.Albajar et al., Nucl. Phys. B335 (1990) 261.

[76] H1 Collab., I.Abt et al., Phys. Lett. B328 (1994) 176.

[77] CDF Collab., F.Abe et al., Phys. Rev. Lett. 61 (1988) 1819.

[78] F.M.Borzumati, B.A.Kniehl and G.Kramer, Z. Phys. C59 (1993) 311;
B.A.Kniehl and G.Kramer, Z. Phys. C62 (1994) 53.

[79] J.F.Botts et al., Michigan State University Report, MSUHEP-93/28 (1993).

[80] J.Binnewies, B.A.Kniehl and G.Kramer, DESY 94-121 (1994).

[81] ZEUS Collab., M.Derrick et al., DESY 95-052 (1995).

[82] J.V.Allaby et al., Fourth International Conference on High Energy Collisions, Oxford (April 1972).

[83] E.W.Anderson et al., Phys. Rev. Lett. 19 (1967) 198.

[84] C.W.Akerlof et al., Phys. Rev. D3 (1971) 645.

[85] P.Capiluppi et al., Nucl. Phys. B70 (1974) 1.

[86] R.P.Feynman, "Photon Hadron Interactions", Benjamin, N.Y. (1972).

[87] ZEUS Collab., M.Derrick et al., Z. Phys. C67 (1995) 93.

Acknowledgements

I would like to thank A.Levy for introducing me to the physics of photoproduction. Without his contagious enthusiasm, encouragement and support this thesis would never be written. I am also grateful for all the help in correcting the manuscript.

I thank B.Löhr, R.Klanner and J.Whitmore for support, stimulating discussions and critical remarks on numerous details of the analysis. I would like to thank all the members of the ZEUS collaboration, in particular the participants of the photoproduction group who were more or less directly involved in this analysis.

I am grateful to H.Abramowicz, G.Levman and G.Wolf for the discussions that turned out to be very helpful in the course of developing the EPSOFT. They also provided me with the code that was directly used in the program. I am grateful to A.K.Wróblewski for the discussions on various aspects of soft processes.

I would like to thank DESY Directorate for the financial support during my stay at DESY.

I am grateful to J.Zakrzewski who, as the boss of the ZEUS group at the Warsaw University, always supported me, making this thesis possible. I would like to thank all the members of the ZEUS Warsaw group for being my home at DESY and at the University. I also acknowledge the help of J.Ciborowski in correcting parts of this manuscript.

I would like to thank my wife Małgosia for her patience.